T2R2 東京工業大学リサーチリポジトリ
Tokyo Tech Research Repository

論文 / 著書情報
Article / Book Information

題目(和文)	BiFeO3ベース積層構造の界面解析および磁気特性
Title(English)	Interface Structure and Magnetic Properties of BiFeO3-based Layered Films
著者(和文)	WangYue
Author(English)	Yue Wang
出典(和文)	学位:博士(工学), 学位授与機関:東京工業大学, 報告番号:甲第10698号, 授与年月日:2017年12月31日, 学位の種別:課程博士, 審査員:史 蹟,細野 秀雄,中村 吉男,中川 茂樹,平松 秀典,木村 好里
Citation(English)	Degree:Doctor (Engineering), Conferring organization: Tokyo Institute of Technology, Report number:甲第10698号, Conferred date:2017/12/31, Degree Type:Course doctor, Examiner:,,,,,
学位種別(和文)	博士論文
Type(English)	Doctoral Thesis

Powered by T2R2 (Tokyo Institute Research Repository)

Doctor Thesis

Interface Structure and Magnetic Properties of $BiFeO_3$-based Layered Films

Yue Wang

Supervisor: Prof. Ji Shi

Prof. Hideo Hosono

Department of Materials Science and Engineering

Interdisciplinary Graduate School of Science and Engineering

Tokyo Institute of Technology

Oct. 2017

Contents

Chapter 1 Introduction

1.1 A brief overview of magnetic storage development

In the past century, our life has experienced world-shaking improvements due to development of semiconductor industry. One of the core parts of semiconductor industry is complementary metal-oxide-semiconductor (CMOS) technology. Today's CMOS technology is mainly electron charge-based device, and has encountered two main challenges as dimensional and functional scaling: power consumption and variability.[1,2] A potential alternative solution under development is spintronic, which utilize another fundamental quantum property of electrons: spin. Magnetic random-access memory (MRAM) is one of the promising storage technology due to its non-volatility, infinite endurance and fast data access.[3,4] Besides, the state-of-art spin-torque-transfer MRAM (STT-MRAM) also attracts great attention as it enables higher density at a low cost.[5]

The first commercial MRAM chips started to launch on market in 2006 by Freescale.[6] Those chips just had 4Mbit storage with 35ns read/write speed. This first generation MRAM devices are designed on toggle-mode, where a magnetic field (induced by current) is used to change the spin. In recent years, MRAM technology has blossomed into second generation, the so-called STT-MRAM. This mode uses spin-polarized current to achieve switching. Many companies, such as Everspin (derived from Freescale MRAM division), IBM, Avalenche Technologies and Crocus, have devoted intense efforts to develop this new technology. Figure 1-1 shows the roadmap on the memory technology updated in 2017. In 2016 Everspin first announced STT-MRAM prototype with perpendicular magnetic tunnel junction (pMTJ).[7] This new design offers lower power and better scalability compared to previous MRAM products. Afterwards, they also demonstrates the world's fastest solid-

state drive based on its pMTJ STT-MRAM technology.[8] If progress smooth, STT-MRAM technology will be commercialized in mass production around 2019.[9] In all, this spintronic memory will stir up a wave of revolution in modern semiconductor field once widely put into use.

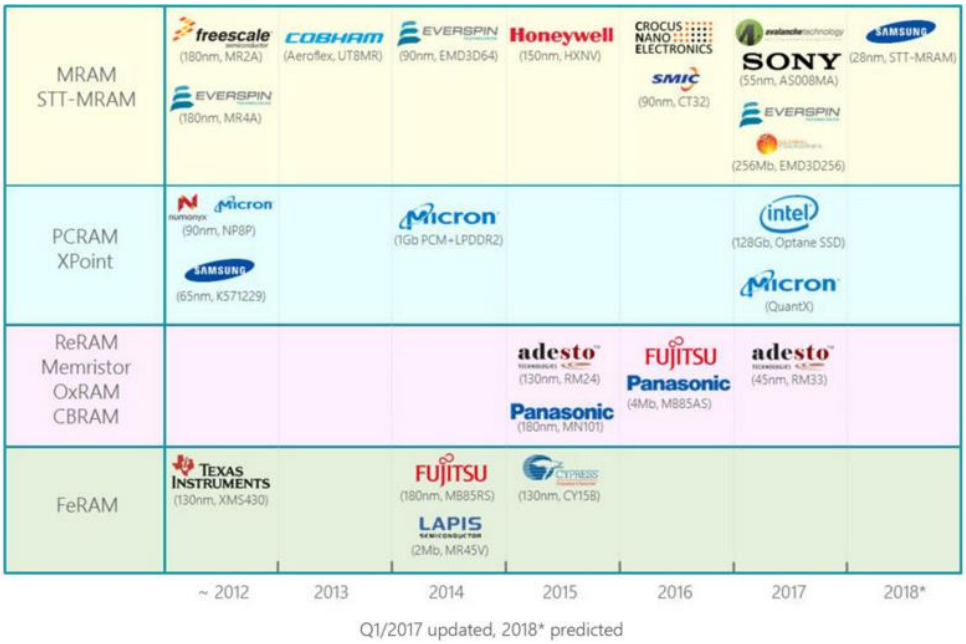

Figure 1-1 Memory technology/produces roadmap.[10]

1.2 Major break-throughs in MRAM

Magnetoresistance effect describes the resistance as a function of the magnetic field due to Lorentz force. The magnitude of magnetoresistance in a normal metal is too small for real application. In 1856, anisotropic magnetoresistance (AMR) was discovered. It emphasizes the resistance depends on the direction of applied magnetic field. Although AMR sensors have successfully replaced inductive sensors in hard-disk industry, its resistance ratio is no more than 10 %. (Now the AMR sensors are mainly used in aerospace field such as A380, due to its robust resistance to cosmic radiation at high altitude). Thus, the most impressive results are giant magnetoresistance (GMR) and tunnel magnetoresistance (TMR).

1.2.1 Giant Magnetoresistance

In 1988, two groups independently discovered GRM effect in Fe/Cr superlattice[11,12], which were awarded the Nobel Prize of physics in 2007. GMR is observed in a multilayer consisting of at least two ferromagnetic layers separated by a non-magnetic spacing layer. The resistance is lower if the magnetizations of two ferromagnetic films are parallel. Otherwise, the resistance becomes larger. GMR effect can be interpreted by two conductive channel: spin-up and spin-down channel.[13] When the spin of electrons is parallel to the magnetization direction of ferromagnetic film, electrons have weak scattering ($R_{\uparrow\uparrow}$). Otherwise, electrons experience strong scattering ($R_{\uparrow\downarrow}$). Thus in parallel magnetization case, two $R_{\uparrow\uparrow}$ and two $R_{\uparrow\downarrow}$ are connected in parallel, the total resistance R_P for this case can be expressed as $\frac{2R_{\uparrow\uparrow}R_{\uparrow\downarrow}}{R_{\uparrow\uparrow}+R_{\uparrow\downarrow}}$. While in antiparallel state, the resistance R_{AP} is $2(R_{\uparrow\uparrow}+R_{\uparrow\downarrow})$. The resistance difference between states is given as $\Delta R = R_P - R_{AP} = -\frac{(R_{\uparrow\uparrow}-R_{\uparrow\downarrow})^2}{2(R_{\uparrow\uparrow}+R_{\uparrow\downarrow})}$. By this result, we know that the larger difference between $R_{\uparrow\uparrow}$ and $R_{\uparrow\downarrow}$, the larger magnetoresistance is.

1.2.2 Tunnel Magnetoresistance

Tunnel magnetoresistance (TMR) originates from spin-polarized tunneling in multilayers (consisting of two ferromagnetic layers separated by an insulating layer), which was discovered in 1970.[14,15] This ferromagnet/insulator/ferromagnet structure is called magnetic tunnel junction (MTJ) cell. Similar to GMR, the resistance of this cell depends on the magnetization direction with respect to each other. At that time, TMR effect did not make an impact to magnetic head industry since the TMR ratio is only a few percent. The first observation of large TMR ratio (~ 10 %) was realized in 1995 with amorphous Al_2O_3 tunnel barriers.[16] In 2004 TMR ratio was further increased to 70.4 % at room temperature using amorphous Al_2O_3.[17] Moreover, a MTJ cell with MgO tunnel barriers was expected to present at least 1000 % by first-principles calculations.[18,19] In 2004,

Fe(001)/MgO(001)/Fe(001) MTJ cell was prepared by molecular beam epitaxy, but the observed TMR ratio was only 180 % at 293 K (247 % at 20 K).[20] TMR ratio was further increased to 604 % at room temperature in Ta/CoFeB/MgO/CoFeB/Ta junctions in 2008, and its TMR ratio measured at 4.2 K was up to 1144 %.[21] All of the TMR effect mentioned above is in longitudinal direction. However perpendicular TMR effect attracts more interests recently. In perpendicular design, two ferromagnetic layers should show large perpendicular anisotropy, so that they can coupled in perpendicular direction. A perpendicular MTJ of GdFeCo/Fe/MgO/Fe/TbFeCo layers was fabricated and TMR ratio was measured at 64 % at room temperature.[22]

1.2.3 Spin transfer effect

In field-mode MRAM, the magnetization direction of one of the two ferromagnetic layers (free layer) is switched by magnetic field induced from current. Arrays of wires (bit lines and word lines) are orthogonal designed and their cross-point are connect by one MTJ cell. When current flow through two wires (bit line and word line), generating magnetic field, switching occurs in this cell (following asteroid curve principle). The required current increases with the reduction of wire size. Therefore, this field-based writing and reading MRAM encountered a scalability limit around 90 nm.[23]

The observation of spin-torque transfer (STT) opens a new way for switching via spin-polarized current rather than magnetic field from adjacent wires. When electrons pass across a metal layer, as we all know they experience scattering, which is independent of original spin polarization. However, when electrons pass across a ferromagnetic layer, spin-dependent scattering takes place. That is after leaving, a high portal of electrons are polarized with the same direction as the ferromagnetic layer (called as spin-polarized current). STT effect says if a spin-polarized electrons flow through ferromagnetic layer, the

magnetization of the ferromagnetic layer becomes aligned to the polarization of the current. Namely there is a spin moment transfer. This magnetization switching takes place if the polarized current density is larger than a threshold value, which is around in the order of 10^6 – 10^7 A/cm^2.[24] First MgO-based STT-MRAM design were published in 2005. [25]

1.2 Introduction of $BiFeO_3$

1.2.1 Multiferroic material $BiFeO_3$

Multiferroic, as explains itself, adopts at least two ferroic orders (e.g. ferroelectric, (anti-)ferromagnetic and ferroelastic) within one material simultaneously.[26,27] Its potential application lies in the coupling interaction between the different orders, such as magnetoelectric (ME) effect. The magnetoelectric effect describes polarization modification upon a magnetic field (the so-called direct ME effect) and vice versa magnetic response to an electric field.[28] Bismuth ferrite ($BiFeO_3$; BFO) is currently the only single phase multiferroic material at room temperature. It was first synthesized in late 1950s, but its detail information such as structure and properties was in vague at that time.[29] In 1970, the first polarization hysteresis loop of BFO was reported in liquid nitrogen, confirming ferroelectric nature of BFO.[30] The observed polarization value was only 6.1 μC/cm^2 along <111> direction due to sample leakage. The ferroelectric Curie temperature (T_c) is around 1100 K.[31] Meanwhile structure of BFO was determined as *R*3c space group via single crystal X-ray diffractions (XRD) and neutron diffraction methods.[32,33] It can be characterized by two distorted perovskite units connected along pseudocubic <111> directions. In this structure FeO_6 octahedral tilt from <111> by ~ 13.8 ° and Fe ions shift from centrosymmetric positions by 0.135 Å, leading to intrinsic ferroelectric state.[34] Structure detail, especially variety in thin film forms, will be discussed in section 1.2.2. In 1980s BFO magnetic nature was reported as G-type antiferromagnet (AFM) up to Néel

temperature (T_N) ~ 658 K and was found BFO endowed a magnetic cycloidal spiral with a long period of 620 Å.[35,36] In particular, the cycloidal spin is incommensurate with the crystal lattice. Thus, it permits a moment canting and results in a weak ferromagnetic moment, which is the so-called Dzyaloshinskii-Moriya (DM) interaction.[37,38] The DM equation can be rewritten into specific form in BFO due to rhombohedral symmetry as $E = -D \cdot (L \times M)$, where D is DM coupling vector (Heisenberg exchange constant J in exchange interaction by analogy), L is antiferromagnetic vector defined as the magnetization differences between two FeO_6 octahedral along <111> directions and M is magnetization addition of the above two FeO_6 octahedral. Thus D, L, and M set up a right-handed system.[39] It is clear that DM interaction (weak ferromagnetism) is determined by the rotations of FeO_6 octahedral and it is the key to magnetoelectric switching scenarios in $BiFeO_3$.[40,41] Research about BFO did not catch too much attention since there exist magnitude disparity between experiment observation and theoretical expectation due to poor sample quality. A revival of BFO starts from 2003, where pure epitaxial thin film was stabilized.[42]

1.2.2 Structure deviation in film form

As we mentioned in last section, bulk BFO presents rhombohedral structure in *R*3c group (a_r = 5.634 Å, α_r = 59.35°)[43]. This is often treated as two distorted pseudo-cubic units (a_{pc} = 3.96 Å, α_{pc} = 89.35 °) connected along body diagonal. For simplicity and conciseness, people often use pseudo-cubic Miller index to label crystallographic structure and so is in this thesis unless indicated. Derived from this pseudo-cubic unit, BFO can take on diverse structures in thin film forms because of the so-called strain engineering,[44] as summarized in Figure 1-2. In all there are 6 different structures: tetragonal, three types of monoclinic M_C M_A and M_B, (these monoclinic can also be treated as M deviations from T or R phases)

rhombohedral and orthorhombic. Here we will describe each structures in detail in the following text.

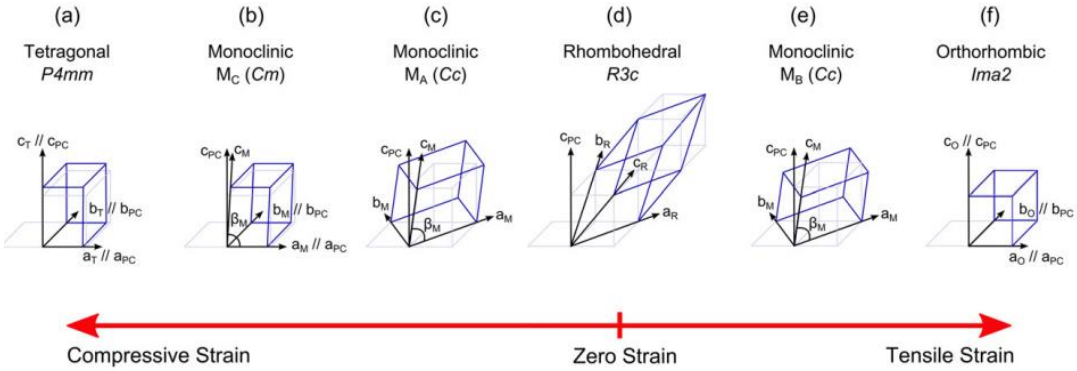

Figure 1-2 Summary of various structures of BFO in thin film form due to strain.[44]

1.2.2.1 Bulk-like rhombohedral (R)

Bulk-like rhombohedral BFO is usually obtained on $SrTiO_3$ substrates (a = 3.94 Å).[45,46] STO substrates can provide the smallest misfit ($\varepsilon = (a_{substrate} - a_{BFO})/a_{substrate} \sim 0.6$ %) among all the commercially available substrates. Evidences show what this structure starts to relax at 30 nm thickness.[47]

1.2.2.2 Tetragonal (T)

Induced by compressive strain, BFO can display a tetragonal phase of P4mm space group.[48,49] The reported c-axis constant was ~ 4.062 Å with tetragonality (c/a) ~ 1.014 – 1.032. This T-phase was stabilized on $Pt/TiO_2/SiO_2/Si$ substrates. In 2009, T-phase was also successfully obtained on (001)-oriented $LaAlO_3$ (rhombohedral phase with pseudo-cubic lattice parameter a = 3.79 Å) substrates, yielding c-axis constant ~ 4.67 Å with tetragonality value ~ 1.23.[50] Furthermore, the rather large tetragonality can remain even if the thickness is increased to 100 nm.

What is more, there exist mixed T and R phase in BFO thin films, forming morphotropic phase boundary. Such mixed phases can be stabilize on (001) LAO substrates, (110) $YAlO_3$ substrates (orthorhombic with pseudo-cubic lattice parameter a =

3.69 Å),[51] (001) $LaSrAlO_4$ substrates (tetragonal with lattice parameter a = b = 3.76 Å).[52] Details about the substrates are summarized in Section 3.1.2.

It should be noted that structure of BFO can be tailored not only by the strain imposed via single crystal substrates, but also by the growth conditions. For example, varying growth rate or substrate temperature can induce T-phase on STO substrates.[53,54,55] Besides, pure R-phase and T-phase BFO can be grown separately on LAO substrates by a careful growth refinement.[56]

1.2.2.3 Monoclinic

Low symmetry monoclinic acts as structural bridge between R and T phases and is often found around the above-mentioned morphotropic phase boundaries.[57] There are three reported monoclinic phases: M_A, M_B, M_C, according to the notation by Vanderbilt and Cohen.[58] The units of M_A and M_B two phases are rotated by 45 ° around c-axis of pseudo-cubic cell and thus volume is doubled compared to pseudo-cubic. The monoclinic distortion originates from c-axis tilting with respect to that of pseudo-cubic cell, resulting in $\beta < 90$ °. The magnitudes of polarization components of M_A and M_B phases are different: for M_A, $P_X = P_Y < P_Z$, whereas $P_X = P_Y > P_Z$ for M_B.[59] For M_C phase, its unit cell almost overlap with that of pseudo-cubic cell but c-axis is tilted from the normal of (110) plane.

Existence of monoclinic distortion cannot be determined merely by out-of-plane XRD. Peak splitting information of (103), (013) or (113) in reciprocal space mapping are usually carried out to obtain the monoclinic angle and lattice parameters.[60,61]

BFO phase transition from T to R is not isosymmetric, but evolves from pure tetragonal phase → monoclinic M_A → monoclinic M_B → pure rhombohedral phase.[57] Therefore monoclinic phase can be obtained on almost all the above-mentioned substrates.[58,59]

1.2.2.4 Orthorhombic (O)

First-principle calculations predicted that an orthorhombic BFO phase may be stabilized in 2 % tensile strain or beyond.[47,62] This phase was first realized on (110)-oriented $NdScO_3$ substrates.[63] Rare-earth scandate substrates, such as $GdFeO_3$, $NdGaO_3$, $SrRuO_3$, etc, are orthorhombic and belongs to *Pbnm* space group. Their (110) plane provides a nearly square units with c/2 = 4.000 Å and $\sqrt[2]{a^2 + b^2}/2$ = 4.013 Å (in $NdScO_3$ case) along [001] and [110] direction, respectively.[64] The lattice parameter of this orthorhombic BFO were measured as: a ~ 3.99 Å, b ~ 4.00 Å and c ~ 3.89 Å.

For systematic explanation of various BFO structures, published review papers can be referenced.[65]

1.2.3 Ferroelectricity

Ferroelectric nature of BFO is no doubt the most investigated scope since its thin film stabilization in 2003. The ferroelectric state is induced by a large displacement of Bi ions relative to FeO_6 octahedral. The measured spontaneous polarization of BFO epitaxial films can reach to 90 – 120 μC/cm^2 along <111> directions.[42,45,46,66] Besides T-phase exhibits a super large polarization ~ 150 μC/cm^2, which comes from an even larger relative ion shift.[48,49,67,68,69]

As BFO exhibits rhombohedral phase, the polarization can point to either <111> directions, generating eight possible domain variants.[70,71] This corresponds to three possible domain boundaries: 71 °, 109 ° and 180 ° domain walls. These values are actually rotational angle between two separating domain states. The 180 ° domain walls are merely ferroelectric type, while the other two are also ferroelastic domain walls.[72] Generally, the different domain types can be characterized by a scanning technique called piezoresponse force microscopy (PFM). Its basic mechanism is to map the polarization directions in each

domains by applying localized electric field. By comparing in-plane and out-of-plane PFM images, a comprehensive domain structure can be obtained.[73]

1.2.4 Antiferromagnetism

Magnetic characterization of BFO did not receive that much attention compared to ferroelectric property mainly due to its small magnitude value. As we discussed previous, BFO is a G-type antiferromagnetic with a cycloidal order imposed on (111) planes. At first, many reports focused on canting or destruction of the cycloidal spin structure, which result in a weak ferromagnetism ~ 0.05 μ_B per unit cell.[39,74] Until 2013, Santo *et al* depicted a magnetic phase diagram of strained BFO films via Mössbauer spectroscopy in 100 % ^{57}Fe films, revealing the structure dependent on spin structures.[75] At low compressive strain range (< 1.6 %) and low tensile strain range (< 0.5 %), BFO films present bulk-like cycloidal spin structures, with <1-10> and <110> propagation directions, respectively. Meanwhile, large strain will induce collinear antiferromagnetic order suppressing cycloidal structures.[76]

Since the coupling between ferroelectric and antiferromagnetic order in BFO films are realized by FeO_6 octahedral rotatio[39], 71 ° and 109 ° polarization switch can lead to magnetic configuration change (magnetoelectric scenario) instead of 180 ° switching.[77]

1.2.5 Devices

Multiferroic nature of BFO enables coupling between electric and magnetic orders, which is quite attractive for device application, especially MRAM.[78] For example, quaternary (four logical states) information system can be realized utilizing co-existence of polarization and magnetization.[79] Furthermore a theoretical model consisting of multiferroic tunnel junction has been put forward to realize octal (eight logical states) data storage.[80]

Apart from logical encoding, electric field control of magnetization is the most investigated topic in BFO-based heterostructures.[81,82] The first observation of electrical control of antiferromagnetic domain structure manipulation was reported in 2006.[83] A domain correlation between ferroelectricy and antiferromagnetism in terms of both domain size and shape were found in (001)-oriented BFO films by PFM imaging and X-ray photoemission electron microscopy. Such coupling demonstration paves the way for electric control of magnetization. Since the magnetic magnitude value of BFO is relatively small, people often use its ordered spin structures. Generally, exotic interface effect will occur between two layers exhibiting different spin structures (such as (anti-)ferromanget, paramagnet, diluted magnetic semiconductor and so on).[84] Thus BFO/ferromagnet heterstructures are often prepared in the attempt to realize E-control of magnetization with the vision that electric signal will pass to ferromagnet through BFO layers.

In 2010, the first reversible electric control of two distinct exchange bias was realized in $La_{0.7}Sr_{0.3}MnO_3$/BFO heterostructures.[85] Applying voltage pulse can reversible modulate the magnitude of exchange bias shift. However, this measurements were conducted at 5.5 K instead of room temperature because of the low blocking temperature (~ 100 - 120K). Other types of electrical control of magnetic properties were also observed. Magnetic anisotropy direction take 90 ° rotation after electric field application in Py/BFO bilayers.[86] Ferromagnetic domain wall rotation upon electric poling switching in $Co_{0.9}Fe_{0.1}$/BFO heterstructures.[87,88] The latter two effects were observed at room temperature. These BFO-based devices with exotic functionality provide perspectives for further information technology. Despite of this promising application, BFO-based devices does not receive the same attention as BFO other characterization. Since intensive experiments have been concentrated on structures (phase transition) and ferroelectric properties, this part remains yet virgin. I think this will be a hot topic in the following years.

1.3 Magnetic interface effect

Magnetic interface effect builds up the mainstay in MRAM technology. There are many kinds of magnetic features induced by interface effect, such as exchange bias, exchange spring coupling and magnetic proximity.[84] In this thesis, we will merely focus on the following two interface effect: exchange bias and exchange-spring coupling.

1.3.1 Exchange bias effect in ferromagnetic/antiferromagnetic bilayers

Exchange bias probably is the mostly explored magnetic interface effect due to its practical application in both experimental and theoretical. As we have discussed previously, there needs two ferromagnetic layers in GMR/TMR cells. One is free layer, the other is pinned layer. As their name can self-explain, magnetization is switched in free layer and stay unmoved in pinned layer. Usually this pinned layer is realized by exchange bias phenomenon. Exchange bias phenomenon is an uni-directional anisotropy and has two main characters: 1) a shift of the hysteresis loop after field cooling, 2) an enhancement of the coercivity compared to single ferromagnetic layers. Unfortunately a clear understanding of exchange bias mechanism is still lacking. Here we just discuss some prevalent models.

1.3.1.1 Stoner-Wohlfarth model

The Stoner-Wohlfarth model names after the two scientists who developed it.[89] This model describes the magnetization behaviors from analytical equations instead of microscale simulations.[90] Although this model cannot clarify the exchange bias effect, it can explain the basic magnetization loop behavior dependence of azimuth angle and deduce the asteroid curve. In other words, this model is the starting point to understand the following expressions. Thus we will start from this model.

For a single ferromagnetic thin, the total energy per unit volume is expressed as following equation:

$$E_v(\beta) = -\mu_0 H M_F \cos(\theta - \beta) + K_F sin^2(\beta) \quad (1)$$

where the first term and second term is Zeeman energy and magnetic crystalline anisotropy, respectively. H is the applied magnetic field; M_F and K_F is the saturation moment and the volume anisotropy constant of ferromagnetic material, respectively; angle θ and β is shown in Figure 1-3.

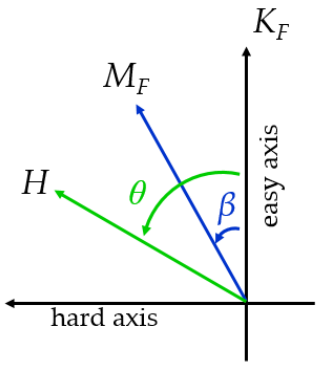

Figure 1-3 Schematic illustration of angles and vectors in Stoner-Wohlfarth mode.

To satisfy energy stable conditions, there are:

$$\frac{\partial E_V(\beta)}{\partial} = 0 \quad (2)$$

$$\frac{\partial^2 E_V(\beta)}{\partial \beta^2} > 0 \quad (3)$$

And we obtain the following equations:

$$-\mu_0 H M_F \sin(\theta - \beta) + K_F \sin(2\beta) = 0 \quad (4)$$

$$\mu_0 \mathrm{H} M_F \cos(\theta - \beta) + 2K_F \cos(2\beta) > 0 \quad (5)$$

Hysteresis loops can be deduced by solving equation 4 with constraint imposed by equation 5. Here people usually define two terms: longitudinal magnetization (projection of M along H) $m_{\parallel} = \cos(\beta - \theta)$, and transverse magnetization (projection of M perpendicular to H) $m_{\perp} = \sin(\beta - \theta)$. Past literature has depicted the numerical-obtained loops at various angle difference,[91] and this goes well with experiment results. Specifically,

hysteresis is squared loop and transverse component is 0 along easy axis. If field is applied long hard axis, longitudinal is a linear line and transverse is an oval shape loop.

Besides, from equation (4) we have:

$$H_c(\theta) = \frac{2K_F}{\mu_0 M_F}|cos\theta| \qquad (6)$$

This is accordance with our common sense as well. Upon easy axis direction (θ = 0), hysteresis gets the broadest and H_c value reach to the largest. While the coercivity field decreases to zero if θ = 2/π (hard axis). Based on this model, the coercivity field dependence of azimuthal angle can also be deduced. This is the famous asteroid equation, which is the basis for writing process in first generation MRAM devices. In this thesis, we will not cover this part in detail.

1.3.1.2 Meiklejohn and Bean model

The exchange bias effect was first discovered in 1956 by Meiklejogh and Bean when studying Co particles embedded in CoO.[92] They have an acuminous understand of this phenomenon and attribute this as unidirectional anisotropy.[93] Soon after a model was proposed to illustrate such anisotropy phenomenon.[94] There are two types of M&B model: ideal case and realistic case. The main difference between the two cases is the assumption of magnetic rigidness in antiferromagnetic layer. In ideal case, AF is rigid and remain unchanged during ferromagnetic rotation. On the contrary, in realistic case AF is allowed to rotate as a whole, leading to addition of antiferromagnetic anisotropy term in total energy. Since the basic idea for the two cases are the same, we will focus on ideal M&B model.

Similar to S&W model, the total energy per unit area is expressed as:

$$\mathrm{E} = -\mu_0 H M_F t_F \cos(\theta - \beta) + K_F t_F sin^2(\beta) - J_{eb}\cos(\beta) \quad (7)$$

Where J_{eb} is the interfacial exchange energy per unit area (J/m^2).

From physical understanding, the anisotropy directions of F and AF, that is K_F and K_{AF}, are assumed to be oriented parallel to the field cooling direction, that is H. This means $\theta = 0$. As AF is rigid and thus AF spin direction remains the same the whole magnetization reversal process. Thus the new schematic view of angles and vectors in ideal M&B model is shown in Figure 1-4.

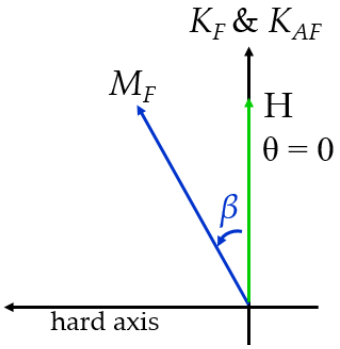

Figure 1-4 Schematic illustration of angles and vectors in ideal Meiklejohn & Bean mode.

Then equation 7 is simplified as following:

$$E_A = -\mu_0 H M_F t_F \cos(-\beta) + K_F t_F sin^2(\beta) - J_{eb}\cos(\beta) \quad (8)$$

$$\frac{\partial E_A}{\partial \beta} = -\mu_0 H M_F t_F \sin(\beta) + 2K_F t_F \cos(\beta) + J_{eb}\sin(\beta) = 0 \quad (9)$$

There are solutions for equation (9),

$$\beta = cos^{-1}\left(\frac{\mu_0 H M_F t_F - J_{eb}}{2K_F}\right) \qquad \text{for } \mu_0 H M_F t_F - J_{eb} \leq 2K_F \quad (10)$$

$$\beta = 0, \pi \qquad \text{for } \mu_0 H M_F t_F - J_{eb} \geq 2K_F \quad (11)$$

solution (11) corresponds to positive and negative saturation, respectively. Thus we can deduce coercivity fields Hc1 and Hc2 from this solution.

$$H_{c1} = -\frac{2K_F t_F + J_{eb}}{\mu_0 M_F t_F} \quad (12)$$

$$H_{c2} = \frac{2K_F t_F - J_{eb}}{\mu_0 M_F t_F} \quad (13)$$

Based on equation (12) and (13), coercivity field and exchange bias field are given as:

$$H_c = \frac{|H_{c1}|+|H_{c2}|}{2} = \frac{2K_F}{\mu_0 M_F} \qquad (14)$$

$$H_{eb} = \frac{H_{c1}+H_{c2}}{2} = -\frac{J_{eb}}{\mu_0 M_F t_F} \qquad (15)$$

Now we have finished the basic derivation process of ideal M&B model. Although the experiment values are usually several orders of magnitude smaller than this theoretical results, this model can still provide us a glimpse of this bias phenomenon. First, it indicates the exchange bias field is always in negative direction. Then it points out exchange bias field value is proportional to the inverse of F thickness. This is easy to understand, since exchange bias is an interface effect. The thinner the F is, the larger the effect is.

1.3.1.3 Malozemoff random field model

In 1987 Malozemoff proposed a new model, the so-called random field model.[95] Enlightened by Neel's AF domain wall concept[96], Malozemoff assumed that in realistic bilayers interface roughness will exert lateral variation effect on F and AF layers. Such random field causes AF to break into several magnetic domains to minimize the total energy. Different from contemporary models, this model focus on the interface mesoscopic scale instead of microscopical and macroscopic scale. By taking interface roughness into consideration, this model successfully deal with the large discrepancy between theory and experiment results.

Malozemoff starts from the exchange field imposed on AF by two F domains. In the final equilibrium condition, we have

$$H_{eb} = \frac{\Delta\sigma}{2M_F t_F} \qquad (16)$$

Where Δσ is interfacial energy. If the interface is ideally compensated, then the exchange bias field will be zero. In other words, "uncompensated" spin configuration across the interface is the prerequisite of existence of hysteresis loop shift. Further interface

energy can be expressed as $\Delta\sigma = {}^{2J_i}/_{a}$. J_i is exchange coupling constant across the interface and a is lattice parameter of AF layer. Thus we have

$$H_{eb} = \frac{J_i}{aM_F t_F} \qquad (17)$$

Now the prediction of H_{eb} are still two order of magnitude larger than experiment results.[97,98] Now Malozemoff introduced a parameter z called number of order unity from physical understanding. This implies atomic roughness can frustrate AF spin pairs and increase energy difference by $2J_A$, where J_A is AF exchange constant. Thus the total energy difference at the interface will be $2J_i + 2J_A$ or $4J$ assuming exchange constants are similar at the both interface sides ($J_A \approx J_i \approx J$). Then AF domain energy is taken into consideration. AD domain wall energy has the value ~$4\sqrt{A_{AF}K_{AF}}$, where A_{AF} and K_{AF} are exchange stiffness and uniaxial anisotropy of AF layer, respectively. Then the exchange bias field can be extracted as following:

$$H_{eb} = \frac{2z\sqrt{A_{AF}K_{AF}}}{\pi^2 M_F t_F} \qquad (18)$$

Till now, the theory and experiment agreement is excellent.

1.3.1.4 Phenomenological explanation of exchange bias effect

Although the mechanism of exchange bias effect is unsolved, we can understand this effect from phenomenological aspect. We first assume both FM and AFM are in a single domain state. Demonstrated in Figure 1-5 (assuming in-plane exchange bias), the whole process start from field cooling treatment.

That is first raise the temperature to T, where $T_{\text{Néel}} < T < T_{\text{Curie}}$. (Here there is a prerequisite of the two layers: $T_{\text{Néel}} < T_{\text{Curie}}$) At this temperature, spin direction of FM aligns along one direction, while spin direction of AFM is random (shown in Figure 1-4-1 state). Then add external magnetic field and cool down. This is the so-called field cooling treatment. Afterwards, the first monolayer spin is fixed by the FM layer (Figure 1-4-2). As

external field is reversed (from positive to negative), FM spin will try to re-orient themselves. Because of the interface coupled exerted by AFM to FM, more energy (magnetic field) is needed to total flip the FM spins compared to single FM layer. In the ascending branch (negative to positive), similarly the FM spins require smaller energy (field) to rotate back to its original states. In all, the magnetization hysteresis loop is shifted along negative field. The larger interface coupling effect/exchange bias effect, the more shift (H_{EB}) is. In this assumption, AFM spin state is simplified to be rigid.

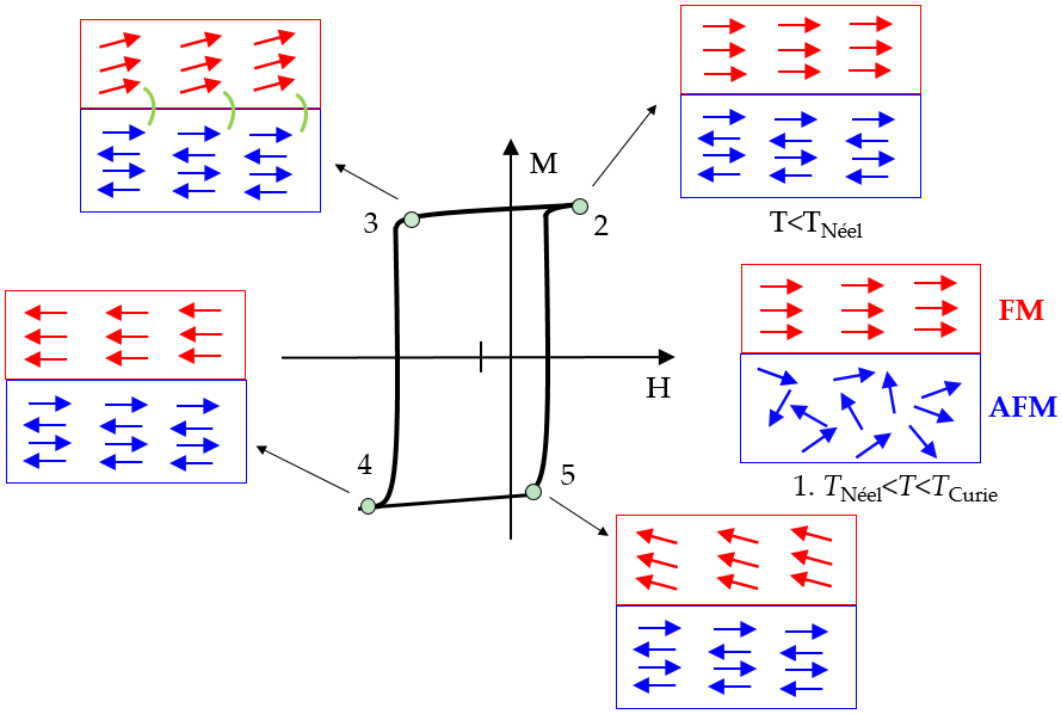

Figure 1-5 Phenomenological model of exchange bias effect in FM/AFM bilayers.

1.3.2 Exchange coupling effect

In the hard disk magnetic recording technology, information is stored in "bit". Each bit consists of tens of grains. To ensure a relative large signal-to-noise ratio (SNR), a number of grains are needed. On the contrary, grain size is reduced (as well as perpendicular recording) for higher areal density. According to $K_1V > k_bT$ thermal stability requirement, materials such as $L1_0$ CoPt with large K_1 value are great candidate as

perpendicular magnetic recording media. However, there is a main issue concerning the high writing field, as it is proportional to K_1/M_s. This is a well know magnetic recording trilemma. One possible solution is through exchange coupling effect.[99] This is usually achieved by depositing another soft magnetic layer on the hard magnetic material ($L1_0$ ordered FePt or CoPt). Thus the soft region responds to magnetic field first and then it will apply a magnetic torque to help the hard region switch. With proper coupling, the coercivity can be reduced to half of that original value. This method is also called as dynamic tilted media.[100]

1.4 Outlines of this thesis

The related background knowledge of this thesis study is briefly introduced in this Chapter, including MRAM development, multiferroic $BiFeO_3$ material and magnetic interface effect.

Chapter 2 explains experimental details including film preparation, microstructure and magnetic characterization and other conducted measurements in this study. Besides, the results of systematic $BiFeO_3$ film growth exploration is also presented. This can give us a brief image of how sensitive $BiFeO_3$ is to the growth conditions, especially to substrate mismatch.

Chapter 3 presents $BiFeO_3$ growth results on TiN conductive under layers. After carefully revising growth conditions, $BiFeO_3$ epitaxial growth can be obtained on TiN layers using MgO (001) substrates.

Followed by film preparation, **chapter 4** mainly focuses on macroscopic magnetic properties of $BiFeO_3/L1_0$ ordered CoPt layered structures. A magnetic field-mediated exchange coupling effect is observed in this films. That is two magnetic states (two-step switching and one-step switching shape in hysteresis loops) can be repeatedly switched

by orthogonal external magnetic field. Both XRD and TEM results indicate epitaxial growth. Element mapping suggests there exist two additional layers across the interface: Co-deficient CoPt layers (~ 1.5 nm) and Co-doped $BiFeO_3$ layer (2 nm). This exact discrepant Co-distribution leads to exchange coupled and decoupled states.

Chapter 5 demonstrates magnetic properties of $Co_2FeSi/BiFeO_3$ layered structures. Co_2FeSi is a half-metallic ferromagnet with high Curie temperature and large saturation moment. Exchange bias effect is observed in this layered films. The antiferromagnetism of $BiFeO_3$ has a pinning effect to the ferromagnetism of Co_2FeSi layers, leading to a coercivity enlargement (from ~ 20 Oe to 80 Oe) after field-cooling treatment.

Conclusions from each chapters are summarized in **chapter 6**.

Reference

[1] Y. Kim, C. Pham and J. P. Chang, *J. Phys. D: Appl. Phys.* **48** 063001 (2015)

[2] A. Makarov, T. Windbacher, V. Sverdlov and S. Selberherr, *Semicond. Sci. Technol*. **31** 113006 (2016)

[3] *What is MRAM* Retrieved from http://www.mram-info.com/introduction

[4] J. Das, S. M. Alam, S. Bhanja, *SPIN* **04** 1450004 (2014)

[5] K. L. Wang, P. K. Amiri, *SPIN* **02** 2 (2012)

[6] *Freescale first to market with MRAM memory chips* Retrieved from http://www.macworld.com/ article/1051739/mram.html

[7] *Evernspin 256Mb ST-MRAM with Perpendicular MTJ Sampling* Retrieved from https://www. everspin.com/news/everspin-256mb-st-mram-perpendicular-mtj-sampling

[8] *Everspin releases fastest and most reliable non-volatile storage class memory* Retrieved from https:// www.everspin.com/news/everspin-releases-fastest-and-most-reliable-non-volatile-storage-class-memory

[9] *SK Hynix, Toshiba Announce 4Gb STT-MRAM* Retrieved from http://techon.nikkeibp.co.jp/ atclen/news_en/15mk/121901031/?n_cid=nbptec_tecrs

[10] *Emerging Memory Technology/Products Roadmap* Retrieved from http://www.techinsights.com/technology-intelligence/overview/technology-roadmaps/#EmergingMemory

[11] M. N. Baibich, J. M. Broto, A. Fert, *et al*. *Phys. Rev. Lett.* **61** 2472 (1988)

[12] G. Binasch, P. Grunberg, F. Saurenbach and W. Zinn, *Phys. Rev. B* **39** 4828 (1989)

[13] C. Chappert, A Fert and F. N. Van Dau, *Nat. Mater.* **6** 813 (2007)

[14] R. Meservey, P. M. Tedrow and P. Fulde, *Phys. Rev. Lett.* **25** 1270 (1970)

[15] P. M. and R. Meservey, *Phys. Rev. Lett.* **26** 192 (1971)

[16] J. S. Moodera, L. R. Kinder, T. M. Wong and R. Meservey, *Phys. Rev. Lett.* **74** 3273 (1995)

[17] D. Wang, C. Nordman, J. Daughton, Z. Qian and J Fink, *IEEE Trans. Magn.* **40** 2269 (2004)

[18] W. H. Butler, X. G. Zhang, T. C. Schulthess and J. M. MacLaren, *Phys. Rev. B* **63** 054416 (2001)

[19] J. Mathon and A. Umerski, *Phys. Rev. B* **63** 220403 (2001)

[20] S. Yuasa, T. Nagahama, A. Fukushima, Y. Suzuki and K. Ando, *Nat. Mater.* **3** 868 (2004)

[21] S. Ikeda, J. Hayakawa, Y. Ashizawa, Y. M. Lee, K. Miura, H. Hasegawa, M. Tsunoda, F. Matsukura and H. Ohno, *Appl. Phys. Lett.* **93** 082508 (2008)

[22] H. Homori, T. Hatori and S. Nakagawa, *J. Appl. Phys*. **103**, 07A911 (2008)

[23] R. Sbiaa, H. Meng and S. N. Piramanayagam, *Phys. Status Solidi-Rapid Res. Lett.* **5** 413 (2011)

[24] L. Berger, *Phys. Rev. B* **54** 9353 (1996)

[25] Z. Diao, D. Apalkov, M. Pakala, Y. Ding, A. Panchula and Y. Huai, *Appl. Phys. Lett.* **87** 232502 (2005)

[26] R. Ramesh and N. A. Spaldin, *Nature* **6** 21 (2007)

[27] N. A. Spaldin, S. W. Cheong and R. Ramesh, *Phys. Today* **63** 38 (2010)

[28] J. Ma, J. Hu, Z. Li and C. W. Nan, *Adv. Mater.* **23** 1062 (2011)

[29] P. Royen and K. Swars, *Angew. Chem*. **24** 779 (1957)

[30] J. R. Teague, R. Gerson and W. J. James, *Solid State Commun.* **8** 1073 (1970)

[31] N. N. Krianik, N. P. Khuchua, V. V. Zhdanova and V. A. Evseev, *Sov. Phys. Solid State* **8** 654 (1966)

[32] C. Michel, J. M. Moreau, G. D. Achenbach, R. Gerson and W. J. James, *Solid Sate Commun.* **7** 791 (1969)

[33] J. M. Moreau, C. Michel. R. Gerson and W. J. James, *J. Phys. Chem. Solids* **32** 1315 (1971)

[34] H. Megaw and C. Darlington, *Acta Crystallogr. Sect. A* **31** 161 (1975)

[35] P. Fischer, M. Polomska, I. Sosnowska and M. Szymanski, *J. Phys. C: Solid State Phys.* **13** 1931 (1980)

[36] I. Sosnowska, N. T. Peterlin and E. Steichele, *J. Phys. C: Solid State Phys.* **15** 4835 (1982)

[37] I. E. Dzyaloshinskii, *J. Phys. Chem. Solids* **4** 241 (1958)

[38] T. Moriya, *Phys. Rev.* **120** 91 (1960)

[39] C. Ederer and N. A. Spaldin, *Phys. Rev. B* **71** 060401-R (2005)

[40] C. Ederer and C. J. Fennie, *J. Phys.: Condens. Matter.* **20** 434219 (2008)

[41] C. J. Fennie, *Phys. Rev. Lett.* **100** 167203 (2008)

[42] J. Wang, J. B. Neaton, H. Zheng, V. Nagarajan, S. B. Ogale, B. Liu, D. Viehland, V. Vaithyanathan, D. G. Schlom, U. V. Waghmare, N. A. Spaldin, K. M. Rabe, M. Wutting and R. Ramesh, *Science* **299** 1719 (2003)

[43] F. Kubel and H. Schmid, *Acta Crystallogr., Sect. B: Struc. Sci.* **46** 698 (1990)

[44] D. Sando, A. Barthélémy and M. Bibes, *J. Phys.: Condens. Matter.* **26** 473201 (2014)

[45] H. Béa, M. Bibes, X. H. Zhu, S. Fusil, K. Bouzehouane, S. Petit, J. Kreisel and A. Barthélémy, *Appl. Phys. Lett.* **86** 071913 (2008)

[46] J. Li, J. Wang, M. Wuttig, R. Ramesh, N. Wang, B. Ruette, A. P. Pyatakov, A. K. Zvezdin and D. Viehland, *Appl. Phys. Lett.* **84** 5261 (2004)

[47] H. Ma, L. Chen, J. Wang, J. Ma and F. Boey, *Appl. Phys. Lett.* **92** 182902 (2008)

[48] K. Y. Yun, D. M. Noda, M. Okuyama, H. Saeki, H. Tabata and K. Saito *J. Appl. Phys.* **96** 3399 (2004)

[49] K. Y. Yun, D. Richinschi, T. Kanashima, M. Noda and M. Okuyama, *Jpn. J. Appl. Phys.* **43** L647 (2004)

[50] H. Béa, B. Dupé, S. Fusil, R. Mattana, E. Jacquet, B. Warot-Fonrose, F. Wilhelm, A. Rogalev, S. Petit, V. Cros, A. Anane, F. Petroff, K. Bouzehouane, G. Geneste, B. Dkhil, S. Lisenkov, I. Ponomareva, L. Bellaiche, M. Bibes and A. Barthélémy, *Phys. Rev. Lett.* **102** 217603 (2009)

[51] R. J. Zeches, M. D. Rossell, J. X. Zhang, A. J. Hatt, Q. He, C. H. Yang, A. Kumar, C. H. Wang, A. Melville, C. Adamo, G. Sheng, Y. H. Chu, J. F. Ihlefeld, R. Erni, C. Ederer, V. Gopalan, L. Q. Chen, D. G. Schlom, V. A. Spaldin, L. W. Martin, R. Ramesh, *Science* **326** 977 (2009)

[52] Z. Chen, L. You, C. Huang, Y. Qi, J. Wang, T. Sritharan and L .Chen, *Appl. Phys. Lett.* **96** 252903 (2010)

[53] H. Liu, P. Yang, K. Yao, and J. Wang, *Appl. Phys. Lett.* **98** 102902 (2011)

[54] H. Liu, P. Yang, K. Yao, K. P. Ong, P. Wu and J. Wang, *Adv. Funct. Mater.* **22** 937 (2012)

[55] P. Ren, S. K. Cho, P. Liu, L. You, X. Zou, B. Wang, J. Wang and L. Wang, *AIP adv.* **3** 012110 (2013)

[56] K. I. Doig, F. Aguesse, A. K. Axelsson, N. M. Alford, S. Nawaz, V. R. Palkar, S. P. P. Jones, R. D. Johnson, R. A. Synowicki and J. Lloyd-Hughes, *Phys. Rev. B* **88** 094425 (2013)

[57] H. M. Christen, J. H. Nam, H. S. Kim, A. J. Hatt and N. A. Spaldin, *Phys. Rev. B* **83** 144107 (2011)

[58] D. Vanderbilt and M. H. Coehn, *Phys. Rev. B* **63**, 094108 (2001)

[59] Z. Chen, Z. Lou, Y. Qi, P. Yang, S. Wu, C. Huang, T. Wu, J. Wang, C. Gao, T. Sritharan and L. Cheng, *Appl. Phys. Lett.* **97** 242903 (2010)

[60] G. Xu, H. Hiraka, G. Shirane, J. Li, J. Wang and D. Viehland, *Appl. Phys. Lett*. **86** 182905 (2005)

[61] H. Toupet, F. Le Marrec, C. Lichtensteiger, B. Dkhil, and M. G. Karkut, *Phys. Rev. B* **81** 140101(R) (2010)

[62] B. Dupé, S. Prosandeev, G. Geneste, B. Dkhil and L. Bellaiche, *Phys. Rev. Lett.* **106** 237601 (2011)

[63] J. C. Yang, Q. He, S. J. Suresha, C. Y. Kuo, C. Y. Peng, R. C. Haislmaier, M. A. Motyka, G. Sheng, C. Adamo, H. J. Lin, Z. Hu, L. Chang, L. H. Tjeng, E. Arenholz, N. J. Podraza, M. Bernhagen, R. Uecker, D. G. Schlom, V. Gopalan, L. Q. Chen, C. T. Chen, R. Ramesh and Y. H. Chu, *Phys. Rev. Lett.* **109** 247606 (2012)

[64] J. Schubert, O. Trithaveesak, A. Petraru, C. L. Jia, R. Uecker, P. Reiche and D. G. Schlom, *Appl. Phys. Lett.* **82** 3460 (2003)

[65] D. Sando, B. Xu, L. Bellaiche and V. Nagarajan, *Appl. Phys. Rev.* **3** 011106 (2016)

[66] R. R. Das, D. M. Kim, S. H. Beak, C. B. Eom, F. Zavaliche, S. Y. Yang, R. Ramesh, Y. B. Chen, X. Q. Pan, X. Ke, M. S. Rzchowski and S. K. Streiffer, *Appl. Phys. Lett*. **88** 242904 (2006)

[67] K. Y. Yun, D. Ricinschi, T. Kanashima and M. Okuyama, *Appl. Phys. Lett.* **89** 192902 (2006)

[68] J. X. Zhang, *et al Phys. Rev. Lett.* **107** 147602 (2011)

[69] M. D. Rossell, R. Erni, M. P. Prange, J. C. Idorobo, W. Luo, R. J. Zeches, S. T. Pantelides and R. Ramesh, *Phys. Rev. Lett.* **108** 047601 (2012)

[70] S. K. Streiffer, C. B. Parker, A. E. Romanov, M. J. Lefevre, L. Zhao, J. S. Speck, W. Pompe, C. M. Foster and G. R. Bai, *J. Appl. Phys.* **83** 2742 (1998)

[71] F. Zavaliche, S. Y. Yang, T. Zhao, Y. H. Chu, M. P. Cruz, C. B. Eom and R. Ramesh, *Phase Trans.* **79** 991 (2006)

[72] J. Sapriel, *Phys. Rev. B* **12** 5128 (1975)

[73] C. S. Ganpule, V. Nagarajan, B. K. Hill, A. L. Roytburd, E. D. Williams, R. Ramesh, S. P. Aplay, A. Roelofs, R. Waser and L. M. Eng, J. Appl. Phys. 91 1477 (2002)

[74] F. Bai, J. Wang, M. Wutting, J. Li, N. Wang, A. P. Pyatakov, A. K. Zvezdin, L. E. Cross, D. Viehland, *Appl. Phys. Lett.* **86** 032511 (2005)

[75] D. Sando, A. Agbelele, D. Rahmedov, J. Liu, P. Rovillain, C. Toulouse, I. C. Infante, A. P. Pyatakov, S. Fusil, E. Jacquet, C. Carrétéro, C. Deranlot, S. Lisenkov, D. Wang, J. M. Le Breton, M. Cazayous, A. Sacuto, J. Juraszek, A. K. Zvezdin, L. Bellaiche, B. Dkhil, A. Barthélémy and M. Bibes, *Nature Mater.* **12** 641 (2013)

[76] J. Juraszek, O. Zivotsky, H. Chiron, C. Vaudolon and J. Teillet, *Rev. Sci. Instrum.* **80** 043905 (2009)

[77] C. Ederer and N. A. Spaldin, *Phys. Rev. B* **71** 224103 (2005)

[78] M. Bibes and A. Barthélémy, *Nature Mater.* **7** 425 (2008)

[79] M. Gajek, M. Bibes, S. Fusil, K. Bouzehouane, J. Fontcuberta, A. Barthélémy and A. Fert, *Nature Mater.* **6** 296 (2007)

[80] F. Yang, M. H. Tang, Z. Ye, Y. C. Zhou, X. J. Zheng, J. X. Tang and J. J. Zhang, *J. Appl. Phys.* **102** 044504 (2007)

[81] J. T. Heron, D. G. Schlom and R. Ramesh, *Appl. Phys. Rev.* **1** 021303 (2014)

[82] L. W. Martin, S. P. Crane, Y. H. Chu, M. B. Holcomb, M. Gajek, M. Huijben, C. H. Yang, N. Balke and R. Ramesh, *J. Phys.: Condens. Matter.* **20** 434220 (2008)

[83] T. Zhao, A. Scholl, F. Zavaliche, K. Lee, M. Barry, A. Doran, M. P. Cruz, Y. H. Chu, C. Ederer, N. A. Spaldin, R. R. Das, D. M. Kim, S. H. Baek, C. B. Eom and R. Ramesh, *Nature Mater*. **5** 823 (2006)

[84] P. K. Manna and S. M. Yusuf, *Phys. Rep.* **535** 61 (2014)

[85] S. M. Wu, S. A. Cybart, P. Yu, M. D. Rossell, J. X. Zhang, R. Ramehs and R. C. Dynes, *Nature Mater.* **9** 756 (2010)

[86] D. Lebeugle, A. Mougin, M. Viret, D. Colson, and L. Ranno, Phys. Rev. Lett. 103, 257601 (2009)

[87] Y. H. Chu, L. W. Martin, M. B. Holcomb, M. Gajek, S. J. Han, Q. He, N. Balke, C. H. Yang, D. Lee, W. Hu, Q. Zhan, P. L. Yang, A. Fraile-Rodriguez, A. Scholl, S. X. Wang and R. Ramesh, *Nature Mater.* **7** 478 (2008)

[88] P. Shafer, F. Zavaliche, Y. H. Chu, P. L. Yang, M. P. Cruz and R. Ramesh, *Appl. Phys. Lett*. **90** 202909 (2007)

[89] E. C. Stoner and E. P. Wohlfarth, *Nature* **160**, 650 (1947)

[90] E. C. Stoner and E. P. Wohlfarth, *Phil. Trans. Royal Soc. London. Series A, Mat. Phys. Sci.* **240**, 826 (1948)

[91] C. Tannous and J. Gieraltowski, *Eur. J. Phys.* **29**, 475 (2008)

[92] W. H. Meiklejonh and C. P. Bean, *Phys. Rev.* **102**, 1413 (1956)

[93] W. H. Meiklejohn and C. P. Bean, *Phys. Rev.* **105**, 904 (1957)

[94] W. H. Meiklejohn, *J. Appl. Phys.* **33**, 1328 (1962)

[95] A. P. Malozemoff, *Phys. Rev. B* **35**, 3679 (1987)

[96] L. Néel, *Ann. Phys. (Paris)* **2**, 61 (1962)

[97] J. S. Kouvel, *J. Phys. Chem. Solids* **21**, 57 (1961)

[98] C. Tsang, N. Heiman and K. Lee, *J. Appl. Phys.* **52**, 2471 (1981)

[99] J. P. Wang, W. Shen and J. Bai, *IEEE Trans. Magn*. **41**, 10 (2005)

[100] J. P. Wang, W. K. Shen, J. M. Bai, R. H. Victora, J. H. Judy and W. L. Song, *Appl. Phys. Lett.* **86**, 142504 (2005)

Chapter 2 Preparation and Characterization of $BiFeO_3$ films

In this chapter, thin film preparation and characterization are explained. This thesis involves several materials, such as $BiFeO_3$, TiN, CoPt alloy, Pt, Co_2FeSi. All of these films were fabricated by magnetron sputtering method. Out-of-plane and in-plane X-ray diffraction were conducted to reveal film structure information and relative orientation relationship. Cross-section transmission electron microscopy were also used to determine interface structures. Magnetic properties were measured by vibrating sample magnetometer. Detail experiment set up will be introduced in this chapter.

2.1 Thin film preparation

Sputtering is a widely-used method to prepare films. Atoms or clusters are ejected from solid targets to substrates by bombarding their surfaces with energetic ions.[1] Besides, vacuum condition is also a prerequisite. Rotary pump and turbo-molecular pump work together to guarantee our base pressure is always lower than $5*10^{-5}$ Pa. Since this method is a world-wide popular technique, no more information about sputtering working mechanism is introduced here.

Our sputtering machine has a max target capacity of six (Figure 2-1), which means six kinds of layers can be deposited in one experiment without breaking the vacuum state. This can greatly reserve the interface state, benefiting the magnetic interface characterization. In the following experiment, we will my experiment benefit a lot from this unique adventage. There are several major categories: direct current (DC), radio-frequency (RF) alternative current (AC) and reactive magnetron. All of the mentioned

categories were used in this thesis, which will be introduced in each material cases following.

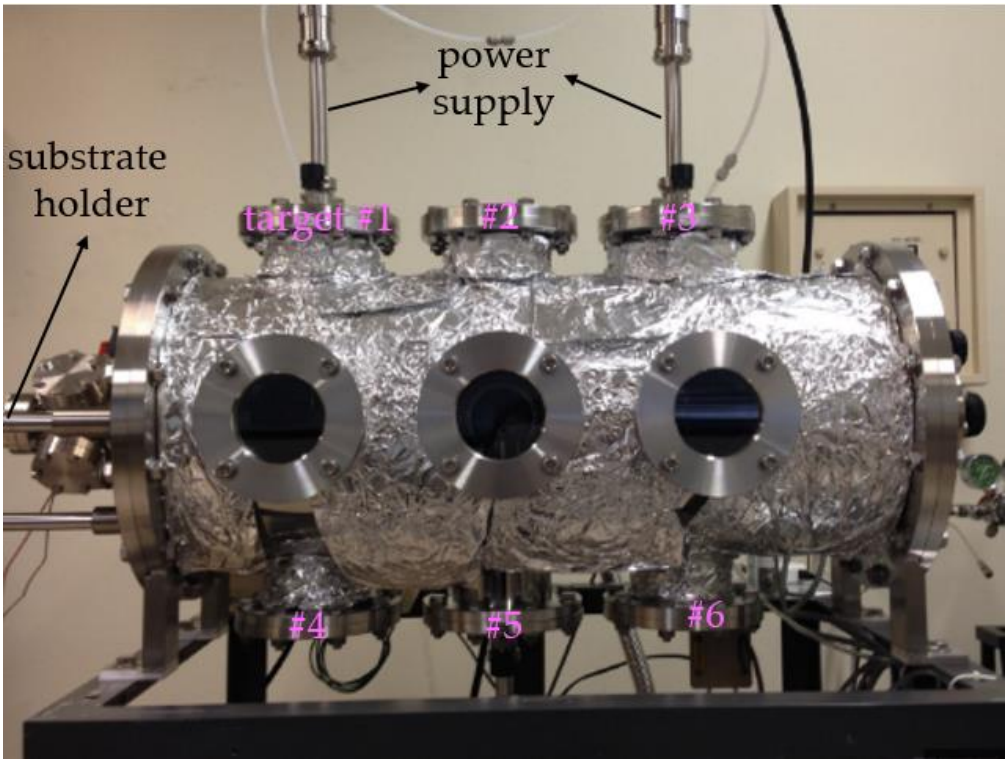

Figure 2-1 Sputtering chamber picture

For $BiFeO_3$ film growth, we use Bi-rich target to compensate the Bi loss during deposition, due to the low vapor pressure of Bi metal. Typical a nominal composition of $Bi_{1.1}FeO_3$ target is used in literature,[2,3] and so is in our experiment. Different from BFO, Bi-rich target presents a bright red color, as shown in Figure 2-2 (a). According to our experience, this Bi-rich target deteriorates with deposition and a new target will expire after around 10 hour-deposition. Our target size is 2 inch in diameter and RF power is fixed at 100 W with growth rate ~ 4 nm/min. Substrate temperature varies from 400 to 700 °C as needed. O_2/Ar gas ratio (volume) is varied from 1:4, 1:7 to 1:10 as needed. The deposition pressure is kept 0.1 or 0.2 Pa. Figure 2-2 (b) is a photo, which is taken at BFO deposition. The plume color shows a bit purple compared to others, probably due to oxygen existence in working gas.

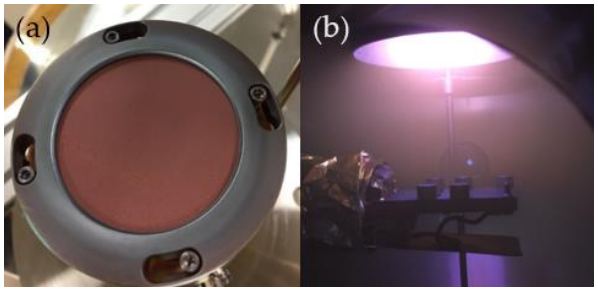

Figure 2-2 (a) Photo of a new $Bi_{1.1}FeO_3$ target (b) BFO deposition plume

2.2 Structure characterization

X-ray diffraction (XRD) measurement is the most common method to detect material structures due to its non-destructive property. For each sample in this thesis, out-of-plane θ-2θ XRD scan is conducted to first confirm the existence of expected phase. If needed, further in-plane scan, pole figure profile and transmission electron microscopy (TEM) are also recorded.

2.2.1 X-ray diffraction (XRD)

X-ray diffraction is a well-known nondestructive structure characterization method, and we will briefly introduce it in this section. Constructive interference occurs as long as Bragg's law is satisfied. The Bragg equation is expressed as $2d\sin\theta = \lambda$, where d is some index inter-planar distance, 2θ is diffraction angle (angle between incident beam and detector) and λ is incident wavelength (~ 1.541 Å for Cu Kα1).

For every sample, we first conduct θ-2θ scan in Bragg-Brentano geometry, where the diffraction vector is always normal to the surface of films. In θ-2θ mode, incident beam is fixed and sample rotates at θ degree/min while detector rotates at 2θ degree/min. For epitaxy sample, only [00L] peak can be detected in this scan.

If needed, further in-plane scan or φ-scan are recorded. 90 °C in-plane scan is the same to out-of-plane scan expect that sample rotates 90 ° in chi (χ) axis. Besides, pole figure

measurement is an indispensable method to find orientation relationship between films and substrate. The sample is first adjusting 2θ and χ angles while keeping θ -2θ configuration. Then diffraction intensity is collected with ϕ rotation.

We use Bruker D8 Discovery μHR machine to conduct in-plane or pole figure with area (2D) diffraction. In in-plane scan, this can distinguish texture sample or epitaxy, since area diffraction also include chi (χ) information. In pole figure, this method can also collect reciprocal space mapping information due to a wide angular range. A schematic illustration of typical XRD geometry set up is depicted in Figure 2-7.

2.2.2 Transmission electron microscopy (TEM)

Transmission electron microscopy (TEM) is a powerful tool for atomic structure observation. A high energy beam penetrate through a thin sample and information coming from interaction between atoms and electrons is collected.

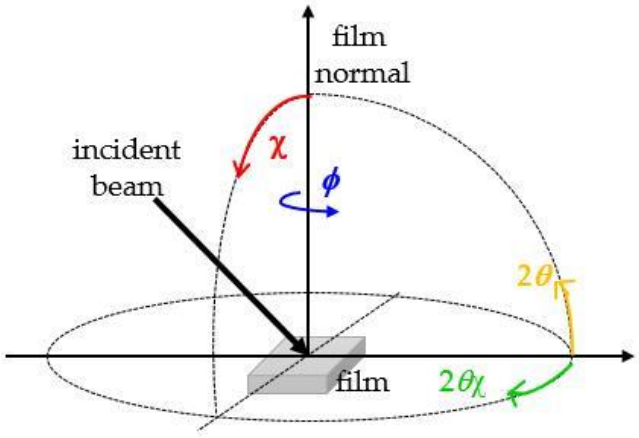

Figure 2-7 A schematic illustration of typical X-ray diffraction geometry set up.

There are mainly two categories of TEM operation: imaging mode and diffraction mode. Imaging is further divided into dark-field and bright-field depending on which beam (direct beam or diffracted beam) passes through aperture. Different from traditional dark field image, high-angle annular dark-field imaging (HAADF) captures electrons

scattered at high angles in scanning TEM (STEM). STEM uses a convergent electron beam to scan the sample. When electrons imping on the sample, it will emit X-ray which can be used to do chemical analysis (element mapping in certain interested area). HAADF method collects information via incoherently scattered electrons, and thus is sensitive to atomic number of atoms. As for the diffracted mode, diffraction pattern containing structure information can be obtained.

To observe TEM, a thinning process is needed. Here I just briefly introduce two kinds of thinning method we use in this thesis: ion milling and focused ion beam (FIB). For ion milling technique, prerequisite steps such as grinding, polishing and dimple are needed to reduce sample thickness. Then high energy ions (usually Ar gas) is used to bomb the sample surface. In FIB a focused Gallium ions probe is operated and small probe current is used to remove atoms from specimen surface.

In this thesis, two types of TEM machines are applied: one is conventional TEM (JEM-3010; JEOL); the other is Cs-corrected scanning TEM (FEI Titan G2 80-200) equipped with energy dispersive X-ray spectroscopy (EDS) and electron energy-loss spectroscopy (EELS).

2.3 Thickness determination

In this thesis, we conduct two methods to measure sample thickness for mutual confirmation.

2.3.1 Step profiler

As the name can self-explain, this method operates a probe to scan the profile of the samples. The height difference between the whole sample and substrate is the film thickness we want. Step profiler is an effective method and easy to get thickness. However, this method can only corresponds to whole films and cannot distinguish each layers in

heterostructure systems. Thus X-ray reflection is a suitable way to measure thickness of each layers.

2.3.2 X-ray reflection (XRR)

X-ray reflection is a useful technique to characterize film thickness and interface roughness. Similar to XRD, information is obtained via interaction between X-ray and atomic planes. Figure 2-8 shows a typical XRR profile and how does useful information is extracted. This figure explain every detail information we can obtain from XRR profile. In brief, oscillation period width is related to film thickness, and oscillation decay rate at higher angles corresponds to interface roughness. Actually, information mentioned in the Figure 2-8 is collected by simulation and thus initial parameters are needed to perform simulation. This means we should have a rough impression (thickness, roughness or density) about the sample in advance in order to get a more precise information. This is why two techniques are used together.

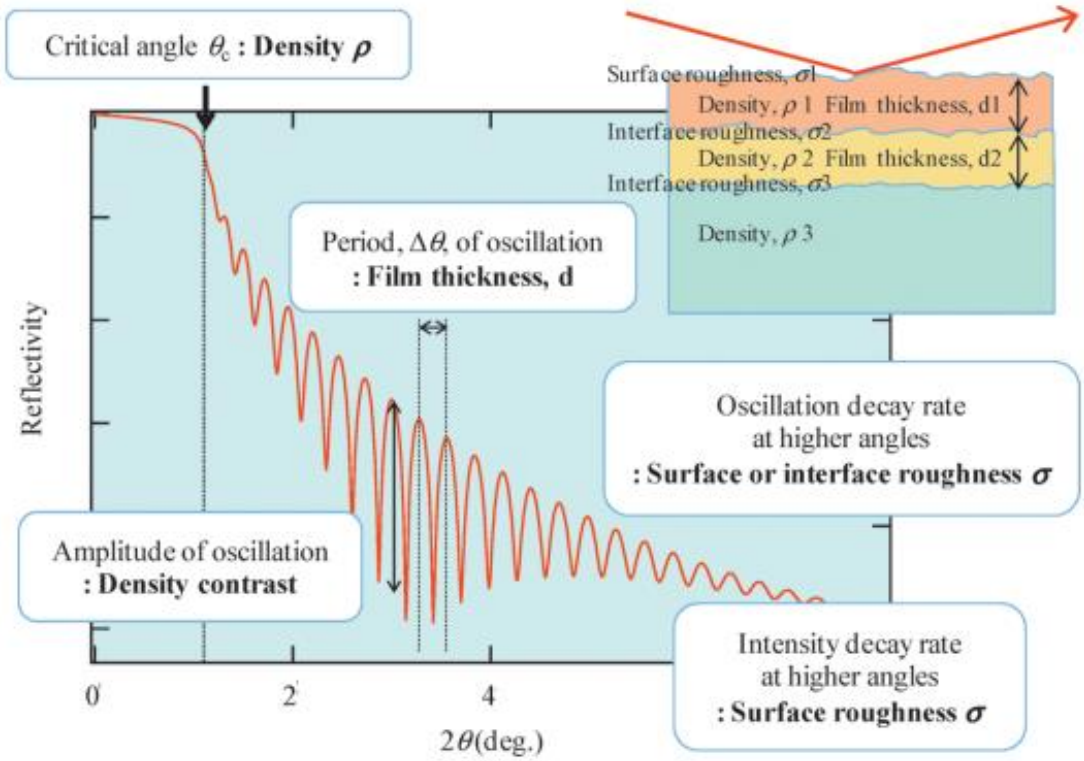

Figure 2-8 Information provided by X-ray reflectivity profile. Retrieved from Ref. [4]

2.4 Magnetic characterization

The magnetic hysteresis loops are first measured by vibrating sample magnetometer (VSM). Some samples are further cut into small pieces and measured by higher accuracy VSM machine, such as physical property measurement system (PPMS)-VSM or superconducting quantum interference device (SQUID). The fundamental mechanism of VSM are given in following section.

2.4.1 Vibrating sample magnetometer (VSM)

The fundamental mechanism of VSM is Faraday induction deprived from Maxwell equation. According to $U = \iint \frac{\partial}{\partial t} \vec{B}\, dS$, induced voltage depends on the change rate of induction B. And thus the electromotive force generated in the pick-up coils is proportional to the magnitude of magnetic moment of the sample. Figure 2-9 briefly draws a VSM schematic diagram.

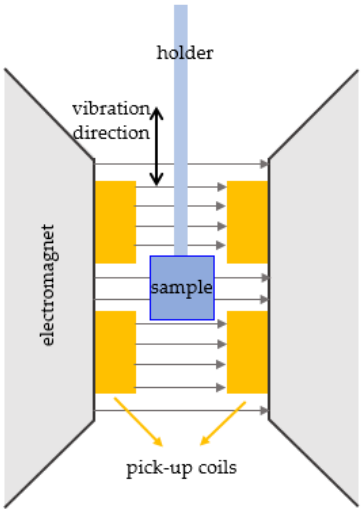

Figure 2-9 A sketch of VSM operation

As indicated in the sketch, the relative movement is realized by sinusoidally vibrating sample in transverse configuration (vibration perpendicular to the field).[5] This induce voltage in the pick-up coils, which is measured by a lock-in amplifier.

VSM machine used in this work is VSM Model BHV-50HTI by Riken Denshi Co., Ltd. The max magnetic field available in this apparatus is 15000 Oe. The magnetic moment measuring range is 0.005 ~ 250 emu and sensitivity is $\pm 2*10^{-6}$ emu. Even the sample size is 10*10mm, no cutting is needed for VSM measurement.

2.4.2 VSM with SQUID

The superconducting quantum interference device (SQUID) can be used in VSM. Different from conventional VSM, samples vibrate inside pick-up coils. The pick-up coils are connected to another input coil, which coupled to a SQUID. Because of flux quantization in superconducting rings, flux change in pick-up coils leads to voltage response in SQUID. And this voltage is measured by lock-in amplifier. Although the SQUID VSM has a high sensitivity (> 10^{-11} Am^2 for MPMS SQUID VSM by Quantum Design), the narrow space inside pick-up coils limit the measurement size of specimen, which means 10 * 10 mm size sample needs to be cut into small pieces.

2.4.3 Field cooling process

Field cooling process is done in VSM high/low temperature mode by Riken Denshi Co., Ltd. The same was VSM measurement, no sample cutting is needed. The temperature range in this apparatus is -196 °C – 700 °C. The high temperature range is realized by heating while the low temperature by liquid nitrogen. The static magnetic field applied in field cooling is 5000 Oe.

2.5 Other measurements

2.5.1 Ferroelectric measurement

For BFO ferroelectric measurement, top electrode and bottom electrode are both required. The buffer layer TiN owns a resistivity ~ 10^{-6} Ωm and can be used as bottom

electrode. After film preparation, BFO is corroded by acid to reveal TiN as bottom electrode. 10 % mass concentration hydrochloric acid is first prepared in fume hood. Then one part of BFO/TiN sample is dipped in acid for corrosion for 2 minutes. Afterwards, ultrasonic cleaning is followed, first in ethanol liquid for 5 minutes then another 5 minutes for distilled water. Finally, sample is baked on hot plate at 70 °C until complete dry. After wet corrosion, 10nm CoPt is sputtered by mask at the top. Before sputtering, sample temperature is raised to 300 °C in vacuum chamber to remove surface contamination. There are three kinds of size in the mask pattern, as shown in the Figure 2-10 (a). The circular size parameter r_1, r_2, r_3 is 0.2 mm, 0.1 mm and 0.05 mm, respectively. Figure 2-10 (b) and (c) show sample before and after CoPt deposition, respectively. As indicated in Figure 2-10 (b), a corner of the BFO sample has been corroded in acid revealing TiN bottom layer, that presents TiN characteristic goldish color. Clearly CoPt pattern can be seen in Figure 2-10 (c).

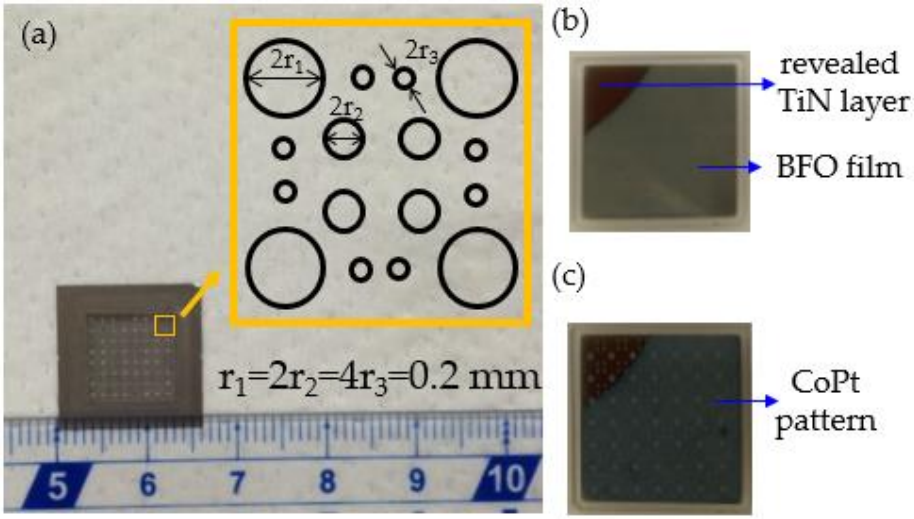

Figure 2-10 (a) A photo of shadow mask with dimension labeled by ruler. Inset is the pattern arrange, where three kinds of size exist. (b) A photo of sample after acid corrosion revealing TiN bottom layer at one corner. (c) A photo of sample after CoPt deposition on the top via shadow mask.

The ferroelectic loops in this thesis are measured by TF 1000 Analyzer FE-Module (aix ACCT Co.) ferroelectric test system. The voltage range is ± 15 V and maximum hysteresis excitation frequency is 1000 Hz.

2.5.2 Atomic force microscopy (AFM)

Atomic force microscopy (AFM) is a non-destructive technique for studying sample surface at nanoscale. AFM uses a cantilever with an atomic size tip to scan over sample surface. A laser beam is used to detect cantilever deflection and profile the film surface. There are several conventional working modes: image mode, contact mode (also called static mode) and tapping mode (also called dynamic mode). We use Microscope Probe Unit (AFM51100N mode) manufactured by HITACHI company. From this measurement, both surface morphology and surface roughness can be obtained.

2.5.3 Auger electron spectroscopy (AES) depth profile

Auger electron spectroscopy (AES) is a surface analysis method. Emitted auger electrons from sample surface (~ 1nm) after electron beam irradiated can be detected. From the kinetic energy and intensity of Auger peak, the elemental identity and quantity of a detected element can be determined. AES depth profile is a chemical content analysis as a function of depth. Each AES measurements are obtained by a sequence of Ar ion etch, as shown in Figure 2-11.

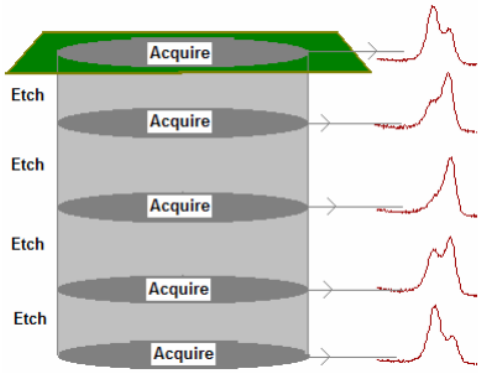

Figure 2-11 Schematic illustration of AES depth profile.[6]

In this work, AES depth profile is measured by JEOL JAMP-9500F. Analysis energy range is 0~ 2500 eV and energy resolution is ΔE/E is 0.05 ~ 0.6 %.

2.6 $BiFeO_3$ film growth exploration

According to previous reported literature, growth window of BFO films is quite narrow and sensitive to environment. Since this is our first time to examine BFO films, plenty of preliminary work has been done on various substrates. This section work aims only to get familiar with BFO growth condition in our sputtering machine, so we have paid all the attention to phase information by XRD method (sometimes followed by surface roughness by AFM).

2.6.1 Experimental details

Basic information, such as $BiFeO_3$ chamber and target, are described in section 2.1. Here we only list the growth conditions used in this chapter.

Determination of initial sputtering parameter comes from reported papers. At first stage, we compensate Bi loss using Bi metal in BFO target. Although this method seems success, it cannot last long due to the difficulty to remain Bi-rich situation for too long. Thus this part experiment is not mentioned in this thesis. Here we only listed repeatable experiment results. Three kinds of substrates has been tried in this chapter. That is amorphous-SiO_2 substrates (a-SiO_2), MgO (001) substrates (mismatch ε ~ -6.6 %) and STO (111) substrates (ε ~ 1.4 %). Table 3-1, table 3-2, table 3-3 list the sputtering parameters of BFO growth on a-SiO_2 (including post annealing process), MgO (001) and STO (111), respectively. Parameter variates are indicated in purple color in the below tables. Substrate bias (-50, -100, -150 V) is applied using a-SiO_2 substrates in the attempt to increase film

crystallinity.[7] Experiments have proved that applying substrate bias (usually at the range of -50 ~ -300 V) can improve film adhesion, increase film density (e.g. Cr), significantly reduce resistivity of metal films (e.g. Ta, W, Ni) and change the film properties as well. Pictures of bias power supply panel are shown to indicate that bias is indeed applied successfully to the substrates, as shown in Figure 2-12.

Figure 2-12 Substrate bias power supply panel of 50, 100, 150 V.

Table 2-1 BFO growth parameters on a-SiO_2 substrates.

substrate	amorphous-SiO_2
base pressure	< 5.0 ×10^{-5} Pa
inlet sputtering gas	5 ccm
gas ratio (O_2 : Ar)	1:4
sputtering power	50 W
sputtering rate	1.67 nm/min
substrate temperature	500 550 600 650 °C
post annealed	700 °C for 2 h at ambient
substrate bias	-50 -100 -150 V

Table 2-2 BFO growth parameters on MgO (001) substrates.

substrate	MgO (001)
base pressure	< 5.0×10^{-5} Pa
inlet sputtering gas	5 ccm
gas ratio (O_2 : Ar)	1:4 1:7 1:10
sputtering power	50 W
sputtering rate	1.67 nm/min
substrate temperature	550 600 650 °C

Table 2-3 BFO growth parameters on STO (111) substrates.

substrate	STO (111)
base pressure	< 5.0×10^{-5} Pa
inlet sputtering gas	5 ccm
gas ratio (O_2 : Ar)	1:4
sputtering power	50 W
sputtering rate	1.67 nm/min
substrate temperature	600 °C

2.6.2 Phase analysis

BFO phase existence is checked mainly by XRD measurements. Figure 2-13 demonstrates phase information of as-deposited sample prepared at 500, 550, 600 and 650 °C, respectively. And Figure 2-14 shows their post annealed results. Grey background indicates Fe_2O_3 peak position and blue corresponds to BFO peak. As we be seen, film is amorphous at low T_s ($T_s \leq 550$ °C) while Fe_2O_3 phase emerge at high T_s ($T_s \geq 600$ °C) for as-deposited samples. And there is no sign of crystal BFO phase existence. This is probably due to formation of amorphous phase. After post-annealing, Bi-deficient phase $Bi_2Fe_4O_9$

and Fe_2O_3 phase crystalize at low T_s. One excited thing is a BFO (001) peak emerges at 650 °C deposition with 700 °C post annealing. Despite of existence of BFO, Fe_2O_3 phase cannot be eliminated, indicating easy formation of amorphous Bi oxide and/or Bi loss on a-SiO_2 substrates.

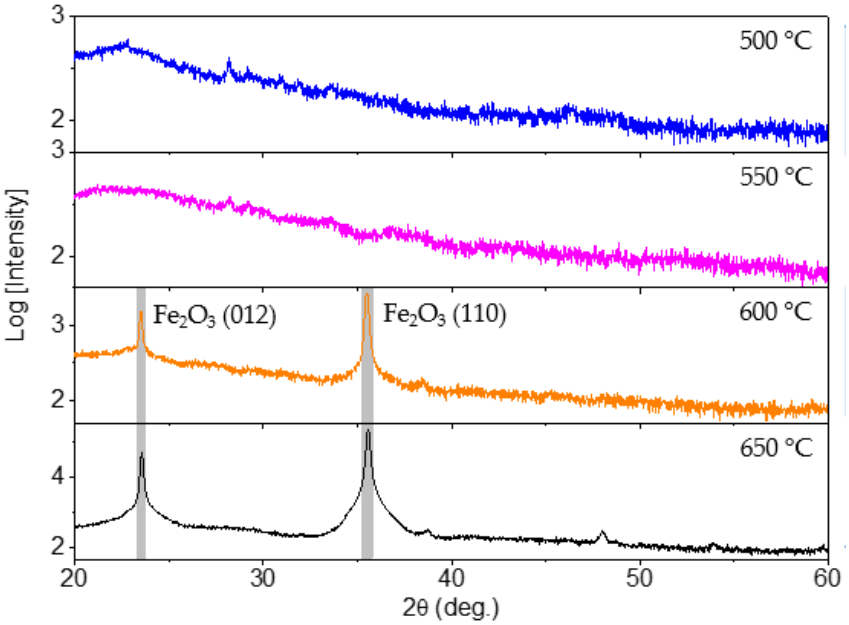

Figure 2-13 XRD profiles of BFO/a-SiO_2 substrates at T_s = 500, 550, 600 and 650 °C, respectively.

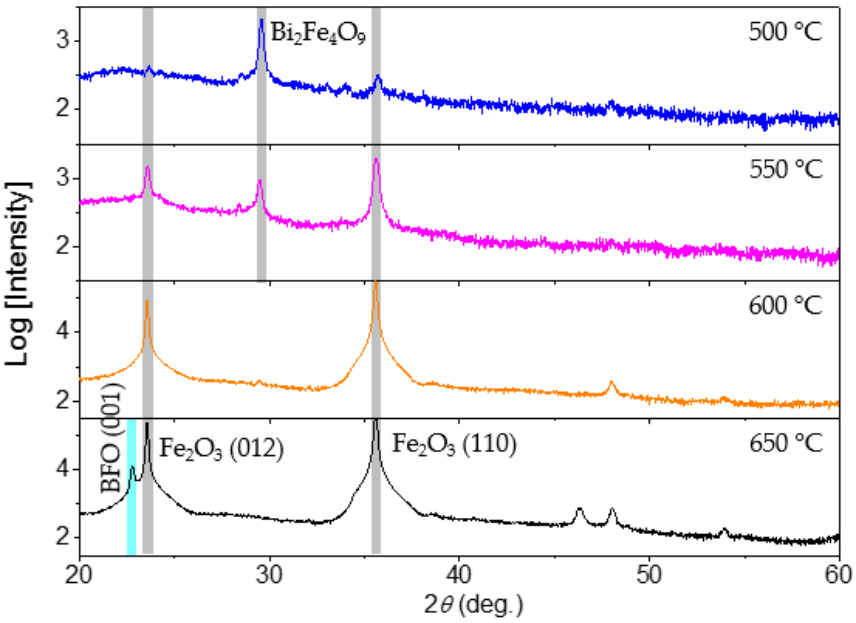

Figure 2-14 XRD profiles of previous sample (deposited on a-SiO_2 substrates at various T_s as shown in Figure 2-13) post-annealed at 700 °C respectively.

The Bi-deficiency problem is further confirmed by Auger electron spectrum, a semi-quantitative method. At 500 ° C as-deposited sample, Bi/Fe atom ratio is 16/19 ~ 0.84, while 600 ° as-deposited sample, the ratio is further decreased to 3/22 ~ 0.27.

Based on this results, we fix the substrate temperature to 500 °C and apply substrate bias in the attempt to increase film crystallinity. Figure 2-15 demonstrates the XRD profiles. One can see from the results from even with -150 V substrate bias, no crystal BFO phase can be detected. Instead, peaks attributed to $Bi_2Fe_4O_9$ seems to emerge.

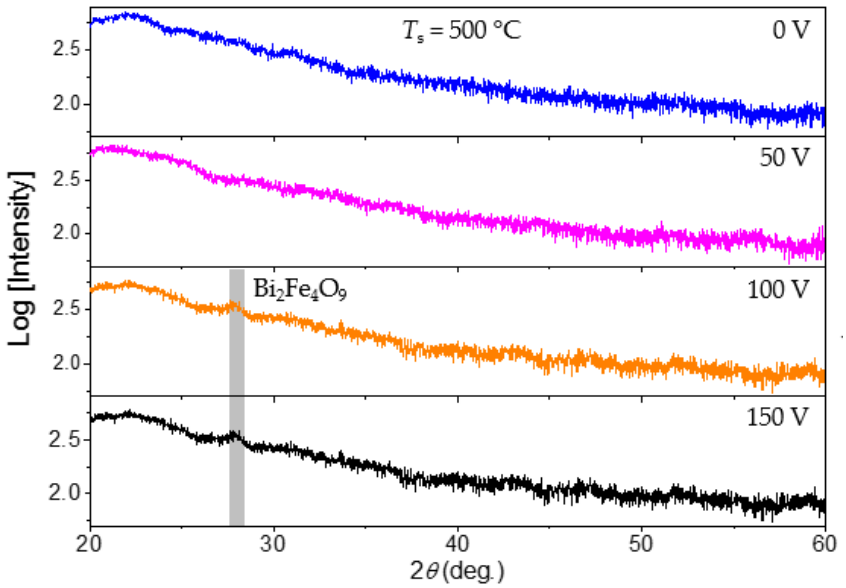

Figure 2-15 XRD profiles of BFO grown at 500 °C on a-SiO_2 substrates with various substrate bias (-50, -100, -150 V).

Due to missing of crystallized BFO phase on a-SiO_2 substrates, we decide to give up a-SiO_2 substrates and select MgO (001) substrates instead. Despite of this failure, we get the impression that BFO phase tends to grow under high temperature, which helps a lot for MgO substrate growth.

Figure 2-16 illustrates XRD profiles of samples deposited at various gas ratio O_2 : Ar ~ 1:10, 1:7 and 1:4, respectively. Under low oxygen partial pressure (O_2 : Ar ~ 1:10 and 1:7), secondary phase $Bi_2Fe_4O_9$ comes into being. $Bi_2Fe_4O_9$ is a common secondary phase when

fabricating BFO in both film and bulk form. From its element stoichiometry, we can expect the existence of $Bi_2Fe_4O_9$ mainly results from Bi deficiency while keep the same oxygen concentration with that of BFO phase. There is another secondary phase, which we will encounter later, and that is $Bi_{24}Fe_2O_{39}$. This phase usually forms when people deliberately increase Bi concentration in the source too much. As a result, precisely control Bi ratio (neither too little nor too huge) is pre-requirement for BFO film growth. Back to this experiment results, further increase gas ratio to 1:4, $Bi_2Fe_4O_9$ phase disappear and BFO phase appears. Besides, BFO phase shows (001) (110) and (111) three growth orientations, forming polycrystalline-like growth.

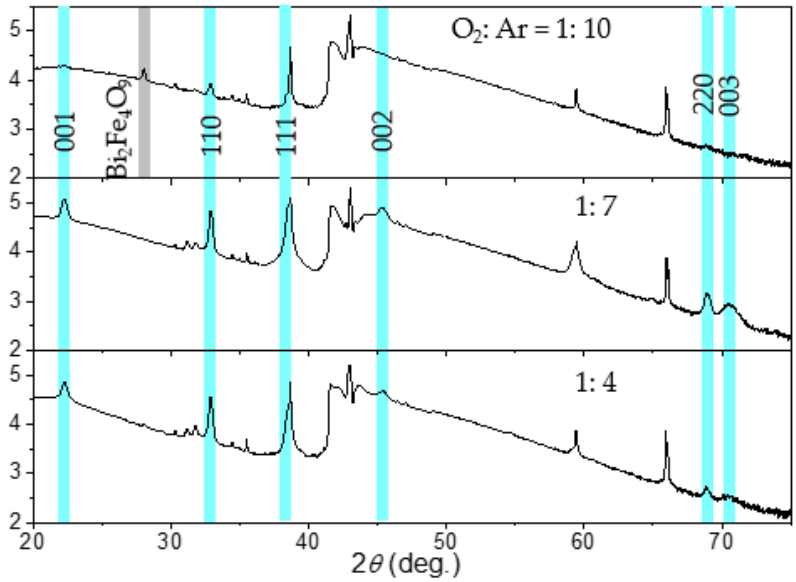

Figure 2-16 XRD profiles of BFO/MgO (001) at various gas ratio O_2 : Ar ~ 1:10, 1:7 and 1:4, respectively. The T_s is fixed at 600 °C.

Figure 2-17 shows XRD profiles of samples deposited at different T_s = 550, 600 and 650 °C, respectively. As one can see clear, T_s = 600 °C is a critical point, whereas both poor crystalized $Bi_2Fe_4O_9$ and BFO phases exist when T_s < 600 °C. Increasing T_s above 600 °C, only textured-BFO phase exists. Thus the optimal growth condition for BFO films on MgO substrate is at T_s = 600 °C and gas ratio ~ 1:4.

Now we can get the conclusion that pure BFO phase can be obtained on MgO (001) substrates. Early than this, no paper about BFO directly grow on MgO has been reported. People usually inset a buffer layer, such Pt[8,9] or SRO[10] to cushion the large lattice mismatch (~ -6.6 %) between MgO and BFO. Besides, Nd-doped BFO is reported to be directly grown on MgO.[11] Different from our results, the doped BFO adopts 45 ° in-plane rotation with respect to MgO substrates. Clearly none of the reported results are the same as the results we got in this work.

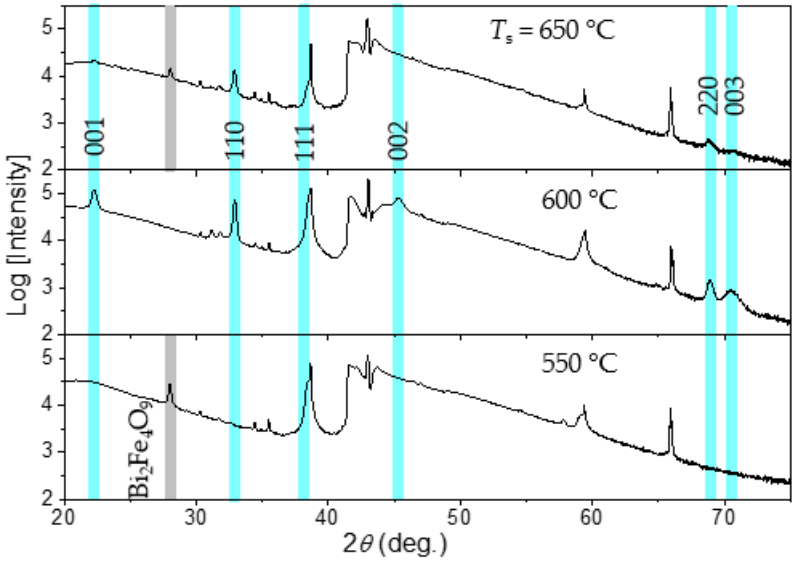

Figure 2-17 XRD profiles of BFO/MgO (001) at T_s = 550, 600 and 650 °C, respectively. Gas ratio is fixed at O_2: Ar ~ 1:4.

The optimal growth conditions on MgO is 600 °C substrate temperature with O_2: Ar ratio ~ 1:4. Furthermore we tried STO (111) substrates, which is a popular substrates for epitaxial BFO growth as we mentioned. Figure 2-18 demonstrates XRD profiles of BFO/STO (111) with χ = 0 and 54.7 °, respectively. Epitaxial growth of BFO, which is cube-on-cube structure, is indicated from XRD pattern and pole figures (shown in Figure 2-19).

In summary, BFO growth is quite sensitive to substrates, especially the lattice mismatch. No pure BFO phase can be grown on a-SiO_2, while BFO present texture crystalline structure on MgO (001) substrates. And epitaxial BFO is easily obtained on STO

(111) substrates. Besides, $Bi_2Fe_4O_9$ secondary phase is the most prone to appear because of the high vapor pressure of Bi element and it is characterized by 28 ° peak position in XRD profiles.

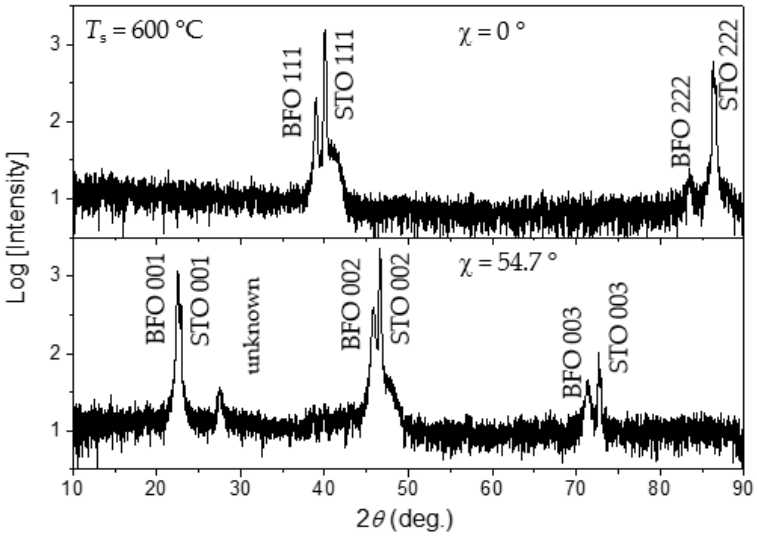

Figure 2-18 XRD profiles of BFO/STO (111) with χ = 0 and 54.7 °, respectively. The growth condition is 600 °C with O_2: Ar ratio ~ 1:4.

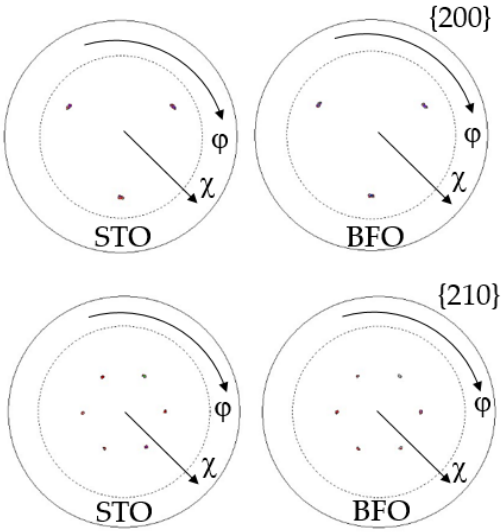

Figure 2-19 Pole figure maps of {200} and {201} reflections of STO substrates and BFO films.

2.7 Summary

Experiment details are explained and summarized in this chapter. Besides, preliminary works about BFO film preparation are also prepared on three kinds of

substrates: a-SiO_2, MgO (001) and STO (111). I need to specify that we use magnetron sputtering to prepare BFO films, which is different from popular method pulsed laser deposition. Sputtering allows us to grow complex heterostructures with smooth interfaces. From our results, no crystal BFO films can be obtained on a-SiO_2 even after high temperature annealing treatment or applying substrate bias, as the same with reported literatures. Poly-crystal like BFO films is grown on MgO substrate (exerting ~ 6.6 % tensile strain), while epitaxial BFO on STO substrates (~ 1.4 % compressive strain). The difference may suggest that the first atomic layer of BFO film is quite critical for film growth. Amorphous substrates can only induce amorphous films, while single crystal substrates can lead to crystalline growth of BFO films. Besides, it also indicates BFO growth is quite sensitive to the mismatch provide by substrates.

Our work may be the first report about successful preparation of BFO films directly grown on MgO substrates.

Reference

[1] Milton Ohring. *Materials Science of Thin Films: Deposition and Structure.* New Jersey: Academic Press, 2002. Print.

[2] Y. H. Lee, C. S. Liang and J. M. Wu, *Electro. Solid State Lett.* **8**, F55 (2005)

[3] R. Y. Zheng, X. S. Gao, Z. H. Zhou and J. Wang, *J. Appl. Phys.* **101**, 054104 (2007)

[4] M. Yasaka, Rigaku J. **26**, 1 (2010)

[5] A. Zieba and S. Foner, *Rev. Sci. Instrum.* **53**, 1344 (2982)

[6] Picture retrieved from http://www.nanolabtechnologies.com/xps-esca

[7] J. L. Vossen and W. Kern, eds. Thin Film Processes. Academic Press, New York, 1978

[8] F. Tyholdt, H. Fjellvåg, A. E. Gunnæs and A. Olsen, *J. Appl. Phys.* **102**, 074108 (2007)

[9] S. Ryu, J. Y. Son, Y. H. Shin, H. M. Jang and J. F. Scott, *Appl. Phys. Lett.* **95**, 242902 (2009)

[10] V. Shelke, D. Mazumdar, G. Srinivasan and A. Gupta, *J. Appl. Phys.* **109**, 07D914 (2011)

[11] I. N. Leontyez, Y. I. Yuzyuk, P. E. Janolin, M. E. Marssi, D. Chernyshov, V. Dmitriev, Y. I. Golovko, V. M. Mukhortov and B. Dkhil, *J. Phys.: Condens. Matter.* **23**, 332201 (2011)

Chapter 3 Epitaxial $BiFeO_3$ growth on TiN conductive under layers

3.1 Introduction

$BiFeO_3$ (BFO) is the only single-phase multiferroic at ambient conditions and has the potential to exert marvelous properties, as we introduced in chapter 1.2. In this chapter, we report epitaxial BFO growth on TiN conductive under layers.

3.1.1 $BiFeO_3$ structure details

We know that BFO can take on various structures deprived from *R*3c under strain. However, there are no standard structure information. First we list calculated structure information, which can be used as a reference in the following experiments. In this section, we present detail structure information calculated by *Diamond – Crystal and Molecular Structure Visualization* (Demo 4.3.2 Version).

3.1.1.1 Rhombohedral

Rhombohedral (R3c) is BFO bulk structure. The detail structure information has been revealed in late 19s,[1] and is listed in Figure 3-1 (a). Figure 3-1 (b) depicts the corresponding atomic structure with two Fe atoms coordinated by distorted octahedral oxygen cages. Figure 3-1 (c) and (d) present diffraction peak details and diffraction pattern, respectively. One thing to be noticed is that diffraction index uses hexagonal unit.

3.1.1.2 Pseudo-cubic

As we discussed in section 1.2.2, pseudo-cubic and rhombohedral is actually two aspects of the same structure. Rhombohedral is BFO original structure, however, for conciseness and simplicity, rhombohedral is split into two distorted perovskite units

(a)

phase data					
space group	*R*3c (No. 161)				
cell	a = 5.63 Å α = 59.35 °				
atomic parameters					
atom	wyck.	site	x/a	y/b	z/c
Bi	2a	3	0.000	0.000	0.000
Fe	2a	1	0.221	0.221	0.221
O	6b	1	0.395	0.528	0.933

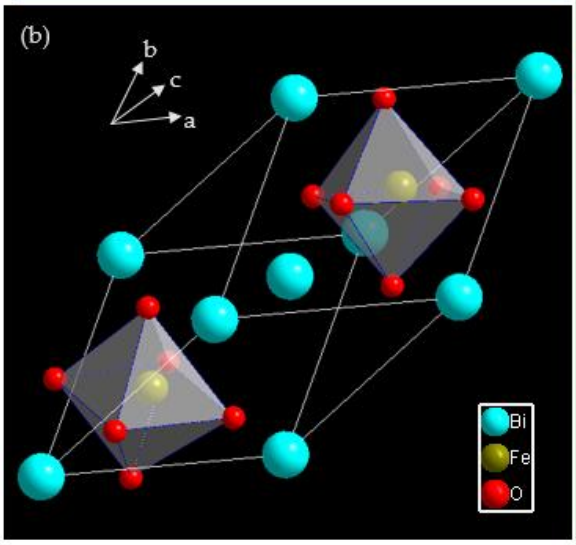

(c)

No.	2Theta ...	d-spacing...	Int.	F	h	k	l	Mult.
1	22.412	3.9637	15115651.00	317.25	0	1	2	6
2	31.742	2.8168	18716648.00	510.33	-1	1	4	6
3	32.066	2.7890	18676768.00	515.41	-1	2	0	6
4	37.636	2.3881	252844.94	50.50	-1	2	3	12
5	38.933	2.3115	1737553.63	336.67	0	0	-6	2
6	39.475	2.2809	5840663.50	361.89	-2	2	2	6
7	45.744	1.9819	8700654.00	521.03	0	2	4	6
8	50.369	1.8102	63862.91	35.21	-2	3	1	12
9	51.294	1.7797	6513542.00	363.04	-1	2	6	12
10	51.732	1.7657	3541376.00	270.30	-1	3	2	12
11	56.339	1.6317	3380714.75	411.54	0	1	8	6
12	56.955	1.6155	7944648.50	451.62	-2	3	4	12
13	57.159	1.6102	4385558.50	476.46	0	3	0	6
14	60.674	1.5251	30032.64	29.81	-1	3	5	12
15	66.315	1.4084	1672140.88	346.69	-2	2	8	6
16	67.061	1.3945	2917323.75	463.38	-2	4	0	6
17	69.654	1.3488	23019.30	30.27	-1	2	9	12
18	70.020	1.3426	16773.58	25.98	-2	3	7	12
19	70.475	1.3351	1440.74	7.66	-2	4	3	12
20	70.566	1.3336	47852.84	44.22	-1	4	1	12
21	70.600	1.3330	1868793.00	391.02	-1	1	10	6
22	71.325	1.3212	1202227.13	316.82	0	3	6	6
23	71.325	1.3212	1085247.25	301.02	-3	3	6	6
24	71.687	1.3155	1468965.50	248.87	-3	4	2	12
25	75.573	1.2572	2679026.50	353.18	-1	3	8	12
26	76.103	1.2497	3137530.00	384.59	-1	4	4	12
27	79.360	1.2064	30811.86	39.47	-3	4	5	12
28	79.654	1.2027	984161.75	316.41	0	2	10	6

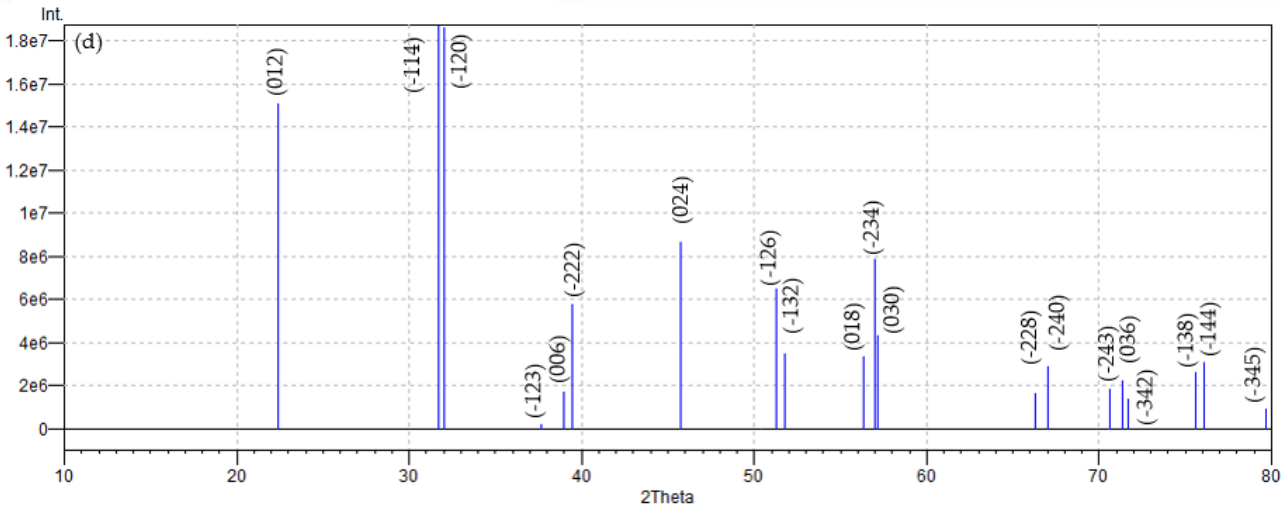

Figure 3-1 Rhombohedral phase of BFO. (a) Detail structure information; (b) Rhombohedral unit cell schematic structure; (c) Calculated diffraction peak information; (d) Calculated diffraction pattern.

(a)

phase data					
space group	Pm-3m (No. 221)				
cell	a = 3.96 Å				
atomic parameters					
atom	wyck.	site	x/a	y/b	z/c
Bi	1a	m-3m	0	0	0
Fe	1b	m-3m	0.5	0.5	0.5
O	3c	4/mm	1	0.5	0.5

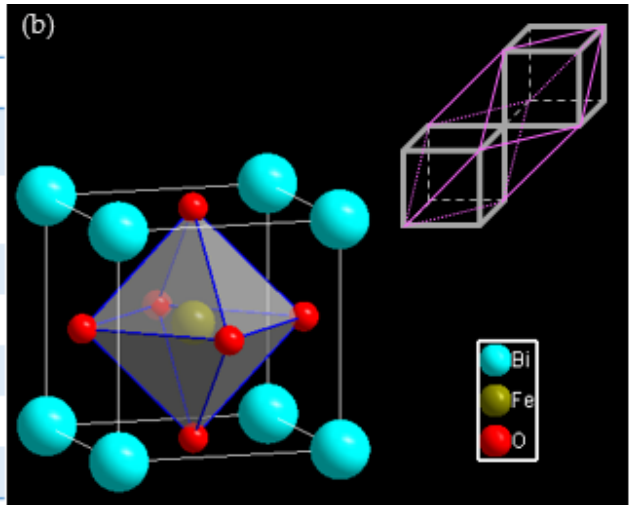

(c)

No.	2Theta ...	d-spacing...	Int.	F	h	k	l	Mult.
1	22.433	3.9600	328348.53	46.80	0	0	1	6
2	31.935	2.8001	1067333.00	86.74	0	1	1	12
3	39.379	2.2863	253906.41	65.17	1	1	1	8
4	45.790	1.9800	310807.28	98.59	0	0	2	6
5	51.566	1.7710	173215.52	42.11	0	1	2	24
6	56.911	1.6167	430495.66	74.27	1	1	2	24
7	66.760	1.4001	192099.28	83.68	0	2	2	12
8	71.403	1.3200	18506.68	39.35	0	0	3	6
9	71.403	1.3200	74026.73	39.35	1	2	2	24
10	75.922	1.2523	188182.38	66.46	0	1	3	24

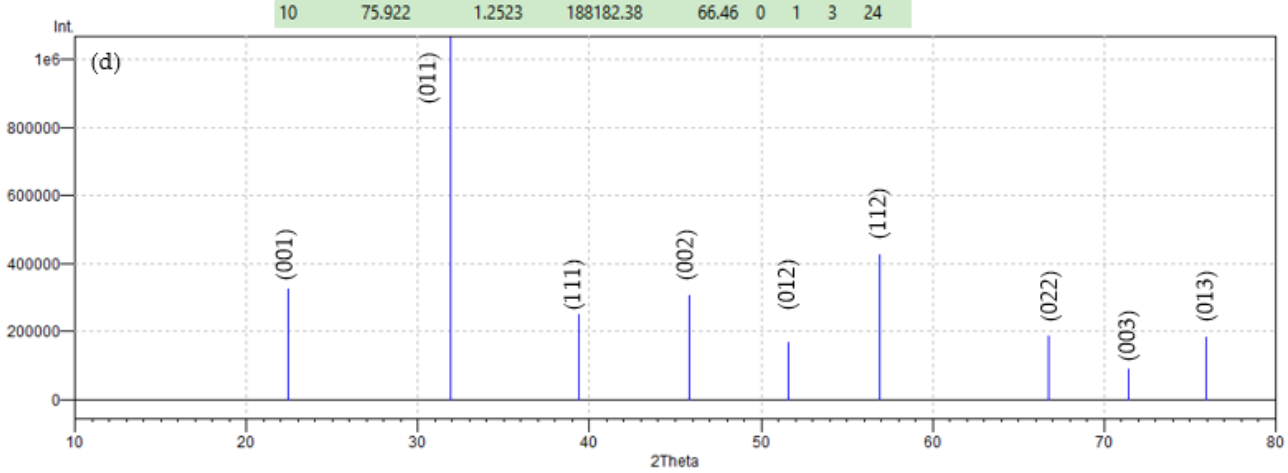

Figure 3-2 Pseudo-cubic phase of BFO. (a) Detail structure information; (b) Pseudo-cubic unit cell schematic structure with inset depicting derivation from rhombohedral unit to pseudo-cubic unit; (c) Calculated diffraction peak information; (d) Calculated diffraction pattern.

(a)

phase data					
space group	P4mm (No. 99)				
cell	a = 3.67 Å c = 4.66 Å				
atomic parameters					
atom	wyck.	site	x/a	y/b	z/c
Bi	1a	4mm	0.000	0.000	0.000
Fe	1b	4mm	0.5	0.5	0.439
O	1b	4mm	0.5	0.5	-0.164
O	2c	2mm	0.5	0	0.308

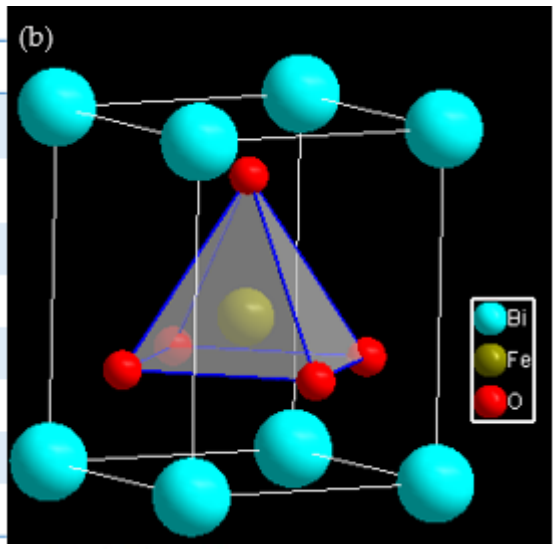

(c)

No.	2Theta ...	d-spacing...	Int.	F	h	k	l	Mult.
1	19.112	4.6400	226611.25	57.04	0	0	1	2
2	24.232	3.6700	183865.72	46.50	0	1	0	4
3	31.044	2.8785	790930.25	88.70	0	1	1	8
4	34.535	2.5951	290416.66	85.31	1	1	0	4
5	38.784	2.3200	91098.08	76.76	0	0	2	2
6	39.766	2.2649	193203.19	57.47	1	1	1	8
7	46.258	1.9610	137488.11	57.44	0	1	2	8
8	49.642	1.8350	161970.67	95.53	0	2	0	4
9	52.893	1.7296	199142.66	80.51	1	1	2	8
10	53.669	1.7064	67307.10	47.59	0	2	1	8
11	55.982	1.6413	46477.67	41.49	1	2	0	8
12	59.713	1.5473	253977.06	73.76	1	2	1	16
13	59.741	1.5467	19761.35	58.22	0	0	3	2
14	64.717	1.4392	84712.16	65.83	0	2	2	8
15	65.430	1.4253	93269.82	69.90	0	1	3	8
16	70.186	1.3399	82721.11	50.08	1	2	2	16
17	70.871	1.3286	33040.21	45.20	1	1	3	8
18	72.835	1.2975	49265.01	80.16	2	2	0	4
19	76.113	1.2496	26054.13	42.93	2	2	1	8
20	78.052	1.2233	10020.22	38.47	0	3	0	4

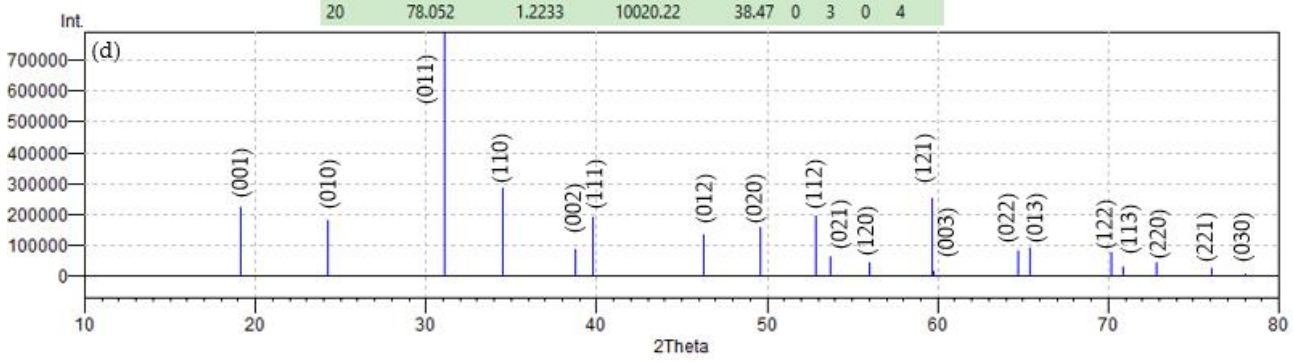

Figure 3-3 Tetragonal phase of BFO. (a) Detail structure information; (b) Tegregonal unit cell schematic structure; (c) Calculated diffraction peak information; (d) Calculated diffraction pattern.

connected along body diagonal direction, as shown in Figure 3-2 (b). If we compare diffraction pattern of rhombohedral and pseudo-cubic phase, their small index peaks match with each other, such as (012) set of rhombohedral and (001) set of pseudo-cubic, (-120) set of rhombohedral and (011) set of pseudo-cubic. In most cases, pseudo-cubic Miller index are used although rhombohedral phase is labeled, especially in single crystal growth and epitaxial films. And so is in this thesis.

3.1.1.3 Tetragonal

Tetragonal phase evolves from pseudo-cubic phase under tensile strain. Figure 3-3 lists tetragonal information containing parameter details (Figure 3-3 (a)), schematic structure (Figure 3-3 (b)), diffraction information (Figure 3-3 (c)) and diffraction pattern (Figure 3-4 (d)).

3.1.2 $BiFeO_3$ film growth

3.1.2.1 $BiFeO_3$ preparation method

Almost all kinds of thin film preparation methods have been used to grow BFO. The most popular method is no doubt pulsed laser deposition (PLD), by which the first BFO film was realized.[2] PLD method can prepare epitaxial BFO films on various substrates regardless of structures[3,4,5,6] and many BFO-based heterostructures are also prepared by PLD due to the high quality of BFO[7,8,9]. Besides, many BFO films are also reported by sputtering method, which is believed to grow complex oxide films with extremely smooth surfaces[10] and compatible with the semiconductor technology. Under optimal conditions, epitaxial BFO can be obtained on single crystal substrates by sputtering.[11,12,13,14] Other method such as chemical solution deposition (CSD)[15,16], metalorganic chemical vapor deposition (MOCVD)[17,18] can also prepare BFO films without secondary phases.

As far as we know, all of the BFO-based heterostructure or devices use PLD method to prepare BFO layer and no other methods have been reported. This indicates that high quality BFO films growth is quite sensitive growth method. However, considering BFO practical application, sputtering is the best growth choice without question.

3.1.2.2 Substrate selection

Single crystal substrates or at least crystalized buffer layer is needed to growth BFO films no matter which growth method is used. Thus, mismatch strain between substrates and BFO films is inevitable. The magnitude of mismatch is defined as $\varepsilon = (a_s - a_{BFO})/a_s$, where a_s is the lattice parameter of the substrate and a_{BFO} is the lattice parameter (~ 3.96 Å) of pseudo-cubic phase. Generally, by choosing an appropriate substrate, fully coherent, epitaxial films with little defects can be obtained. Figure 3-4 shows lattice constants of some commercial single crystal substrates. In section 1.2.2, we have briefly summarized the substrate selection for different BFO phases.

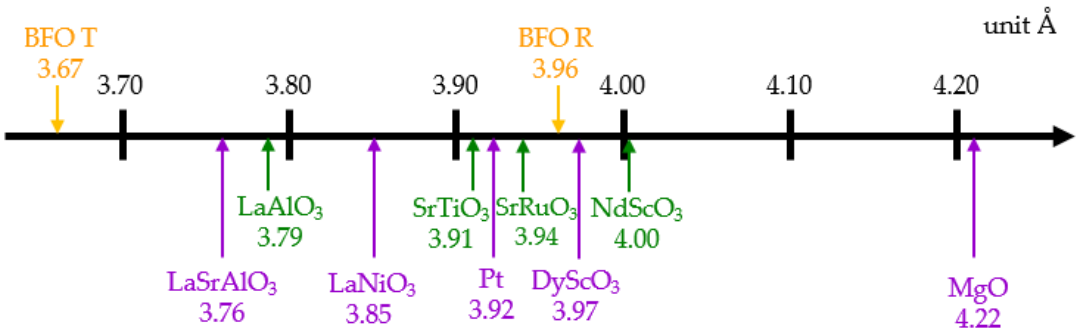

Figure 3-4 A number line showing (pseudo-)cubic or (pseudo-) tetragonal in-plane lattice constants of BFO films (above line) and of substrates or common buffer layers.

Although epitaxial BFO films can be realized on various substrate, theses listed substrates is of high cost and quite a few is compatible with Si-based technology. The cheapest substrate above is MgO (001)-orientation with at least 3000 JPY. Only $LaNiO_3$ layer is reported to be buffered on Si wafer.[19] Besides, conductive property of substrate or

buffer layer is needed in order to input electric signal to BFO films, from practical point of view. Currently Nd-doped STO substrates[20] and SRO[21,22,23] or Pt layers[23,24] are placed to solve this problem. Therefore an alternative buffer layer is needed to satisfy both Si-compatible and conductive for epitaxial BFO film growth.

3.1.3 Objectives in this chapter

For application aspect, BFO needs to be grown with efficient cost (especially the single crystal substrate cost) and reduced deposition temperature. Thus we aim to achieve well crystallized BFO film with no secondary phase. To achieve this target, we propose to use conductive TiN as under layers to prepare BFO films. As has been proved that TiN is conductive[25] and can epitaxially grow on Si (001) wafer[26]. Besides, TiN has high thermal stability and low cost advantages.

Structure of TiN is NaCl-type, which is the same with MgO substrates. Besides, the lattice parameter of TiN (a_{TiN} ~ 4.24 Å) is also quite near to that of MgO (a_{MgO} ~ 4.22 Å). Based on the results obtained in Chapter 2, such large mismatch (~ 6.6 %) between BFO and TiN under layers may not be a problem to prepare pure BFO phase. Besides, it has been reported that at the surface of TiN layers various atom bonding conditions between Ti and O easily occurs as long as oxygen exists.[27] We hope such bonding may promote crystal BFO growth.Based on such proposal, we systemically investigated BFO growth on TiN under layers.

3.2 Experimental details

BFO film preparation is detailed explained in chapter 2. As for the growth conditions, all the investigated parameters in this chapter are listed in Table 3-1.

Table 3-1 Sputtering parameters of BFO layers

bottom layer	TiN layer
inlet sputtering gas	5 ccm
gas ratio (O_2 : Ar)	1:4
substrate temperature	600 °C
sputtering power	50 W
sputtering rate	1.33 nm/min
thickness	100 nm

As for TiN, this under layer is prepared by reactive sputtering method. Ti metal target (2 inch diameter) is used and N_2 gas is also supplied apart from Ar gas. The gas ratio (N_2 : Ar) varies from 1:3 to 1:21. Substrate temperature is fixed at 500 °C. DC power supply is used by fixing current at 200 mA with its corresponding voltage ~ 260 – 270 V. Figure 3-5 shows Ti target (2 inch in diameter) and TiN deposition plume (N_2:Ar ratio ~ 1:15), respectively. The working pressure is 0.5 Pa. Table 3-2 lists all the sputtering parameters of TiN layers.

Figure 3-5 (a) Ti metal target (b) TiN deposition plume (N_2 : Ar ratio ~ 1:15)

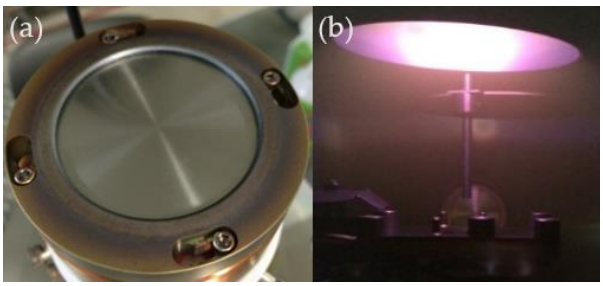

Table 3-2 Sputtering parameters of TiN layers in this section work (a-SiO_2 substrates)

substrate	amorphous-SiO_2
base pressure	< 5.0 ×10^{-5} Pa
inlet sputtering gas	5 ccm
gas ratio (N_2 : Ar)	1:9 1:12 1:15 1:18 1:21
substrate temperature	500 °C
sputtering power	200 mA ~ 280- 290 V
sputtering rate	1.33 nm/min
thickness	80 nm

3.3 BFO/TiN/amorphous-SiO_2 films

Amorphous-SiO_2 substrates instead of single crystal substrates are firstly used. And TiN film growth details are systematically explored.

Figure 3-6 clearly lists the XRD profiles (left-hand side) and AFM images (right-hand side) of 80 nm TiN films deposited on a-SiO_2 substrates under different N_2 : Ar gas ratio ~ 1: 9, 1:12, 1:15, 1:18 and 1:21, respectively. Roughness values are also indicated at each conditions. Peak orientation is labeled by yellow shadow background. Under high N_2 partial pressure (N_2: Ar > 1: 12), film crystallinity is poor (suggested by the low peak intensity) with low roughness. When N_2: Ar ratio ~ 1: 15, TiN crystallinity is the best as the sacrifice of high surface roughness (32 nm with in-total 80 nm thickness). And only (111)-oriented peaks exists under this condition. This means (111) orientation is easily grow for TiN layers. Further lowing N_2 concentration, TiN tends to be polycrystalline (other orientation such as (222) and (200) appear) and roughness decreases. In all, (111)-textured TiN films are easily obtained on a-SiO_2 substrates.

Gas ratio dependence of film resistivity is draw in Figure 3-7. The resistivity magnitude decreases from 10^{-4} to 10^{-6} with reducing N_2 partial pressure. This range can be defined as nearly conductive material in common sense (< 10^{-8} Ω m). In common, people define that 10^{-6} magnitude order resistivity is within conductive range, which accomplishes conducting function. Clearly TiN deposited at small N_2 concentration (< ~ 1: 15 ratio) is conductive. This conductivity property of TiN qualifies itself as bottom electrode for BFO films.

Balancing TiN film crystallinity (surface roughness) and resistivity magnitude order, we choose 1:12 and 1:15 gas ratio conditions for further preparing BFO films on top of TiN. Unfortunately, no crystalized BFO phase is detected under these two conditions, as shown in Figure 3-8. TiN (111) peak is labeled by yellow background while possible BFO peak

positions are indicated by blue lines in Figure 3-8. The vanish of BFO phase on TiN (111) films indicates two possible reasons: BFO growth is sensitive to roughness or (111)-orientation under layer is difficult to induce crystal BFO formation than that of (001)-orientation. We expect the second reason may be the main reason. This may come from the stability difference between (001) and (111) surfaces, as suggested by first-principle calculations.[28] Compared to (001), (111) surfaces are energetically unfavourable, and thus (111) TiN need more energy to trigger the nucleation of BFO phase, which cannot be provided in sputtering preparation.

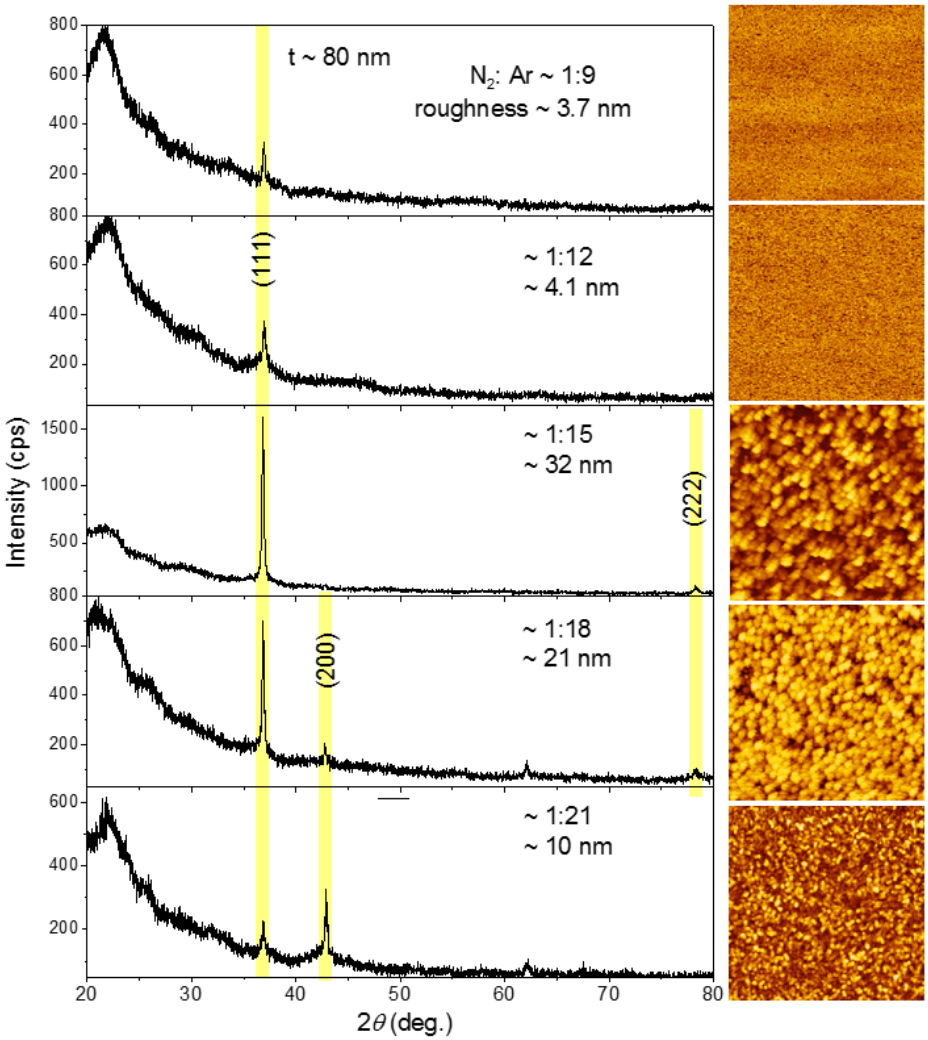

Figure 3-6 XRD profiles (left-hand side) and AFM images (right-hand side) of 80 nm TiN films deposited on a-SiO_2 substrates under various N_2: Ar gas ratios.

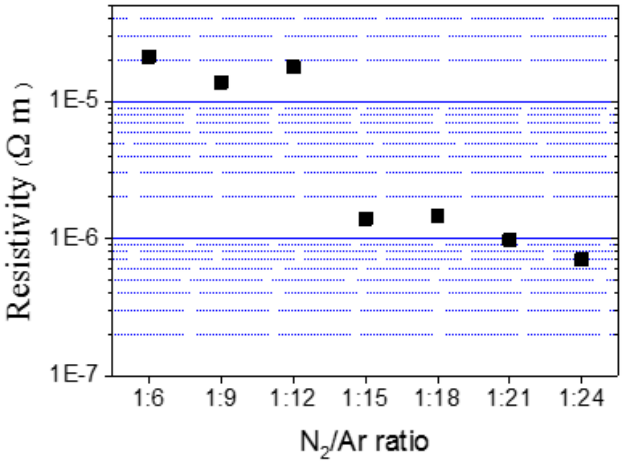

Figure 3-7 Gas ratio N_2: Ar dependence of film resistivity tendency.

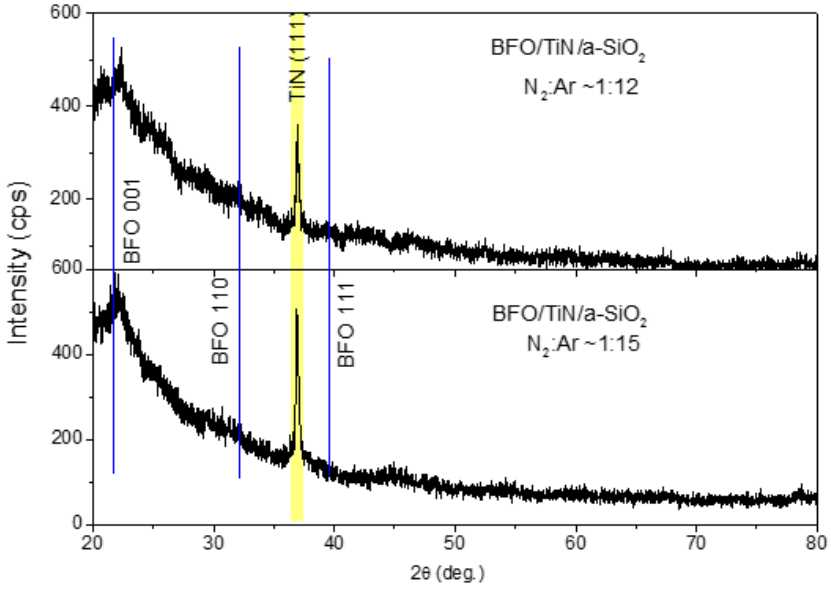

Figure 3-8 XRD profiles of BFO/TiN/a-SiO_2 bilayers. TiN layers are prepared under different gas ratio N_2:Ar ~ 1:12 and 1:15, respectively. TiN (111) peak is labeled by yellow background, while blue lines indicate possible BFO peak position.

3.4 $BiFeO_3$/TiN/MgO (001) films

After the failure of BFO/TiN on a-SiO_2 substrates, MgO (001) substrates are chosen to induce (001)-orientation of TiN layers. Since the lattice parameter of TiN (a ~ 4.241 Å) is almost the same with that of MgO (a ~ 4.219 Å), the roughness of TiN can also be reduced meanwhile. This method is expected to facilitate BFO epitaxial growth.

3.4.1 Experimental details

This section mainly focuses on BFO/TiN bilayers preparation on MgO substrates. Detail experiment deposition parameters are listed in Table 3-3 for TiN and BFO each films. The growth condition is decided based on results obtained from films grown on a-SiO_2 substrates. The same with previous, purple color indicates parameter variates, which is the substrate temperature for BFO films. Besides, the RF power supply of BFO is increased from previous 50 W to current 100 W in the attempt to promote film crystallinity and speed up growth rate as well.

Table 3-3 Sputtering parameters of BFO/TiN/MgO (001) substrates

	TiN	$BiFeO_3$
substrate	MgO (001)	
deposition pressure	0.6 Pa	0.2 Pa
inlet sputtering gas	5 ccm	5 ccm
gas ratio	N_2 : Ar ~ 1 15	O_2 : Ar ~ 1 : 4
substrate temperature	500 °C	450, 500, 550, 600, 650, 700 °C
sputtering power	200 mA ~ 280- 290 V	100 W
sputtering rate	2.67 nm/min	4 nm/min
thickness	80 nm	30 nm

3.4.2 Microstructure analysis of TiN/MgO (001) films

XRD profile and AFM image of 80nm TiN film on MgO (001) substrate are depicted in Figure 3-9. As expected, (001)-oriented TiN is induced with a roughness value S_q/RMS ~ 0.4 nm. And the measured resistivity is at the order of 10^{-6} Ωm, which is capable to serve as conductive bottom layer. Both phase detection and surface roughness can satisfy under layer requirements.

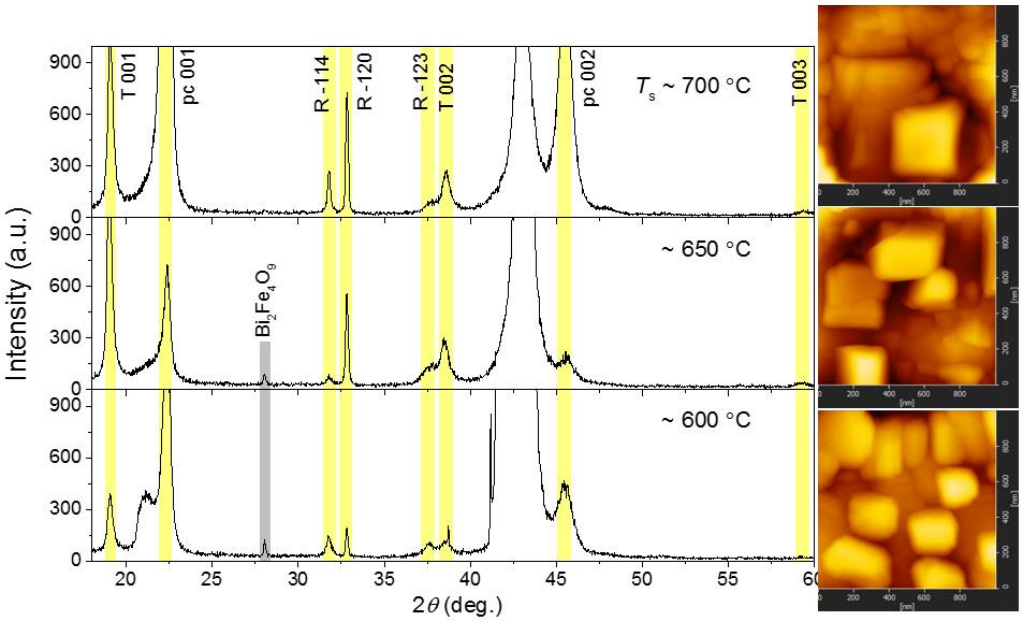

Figure 3-9 XRD profile and AFM image of 80 nm TiN grown on MgO (001).

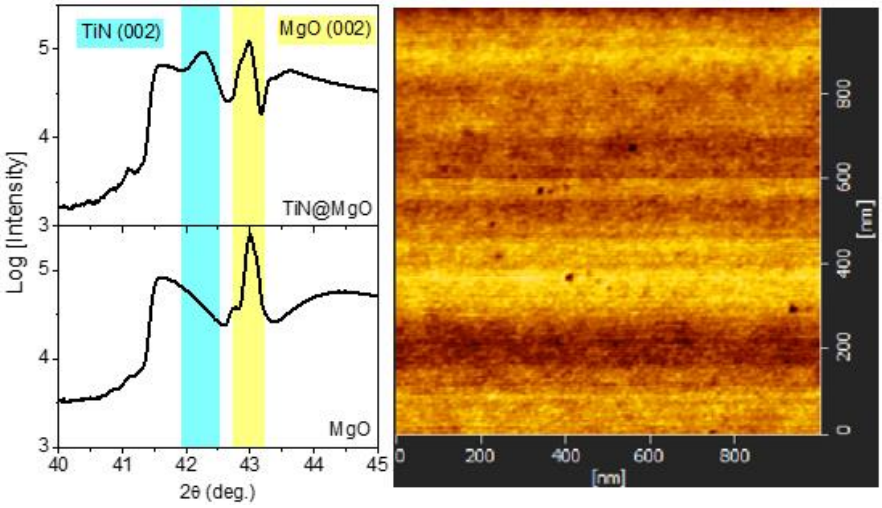

Figure 3-10 XRD profiles of BFO/TiN/MgO (001) grown at T_s = 700, 650, 600 °C. Right-hand row is corresponding AFM image.

3.4.3 Microstructure analysis of BFO/TiN/MgO (001) films

According to reported papers, the growth window of BFO is around 600 – 700 °C. Thus we perform a systematic substrate temperature dependence of BFO structure, as shown in Figure 3-10. As one can see from XRD profiles, BFO becomes crystal on TiN (001)-oriented layers. And different BFO phases (T, R and pc) appear. When T_s = 700 °C, all the

peaks can be attributed to BFO phases. If lowing T_s to 650 and 600 °C, a small peak coming from secondary phase $Bi_2Fe_4O_9$ emerges. The perfect crystallinity of BFO can also be confirmed by AFM images, where square facets are clearly observed.

Different from prevalent conception, BFO also grows at low temperature range (T_s < 600 °C). Figure 3-11 lists XRD profiles and AFM images of BFO/TiN grown under T_s = 550, 500 and 450 °C, respectively. Quite exited, crystal BFO phase can still be obtained despite of the low diffraction intensity. And AFM images clearly indicates the crystal facets shape of BFO phase at 500 °C.

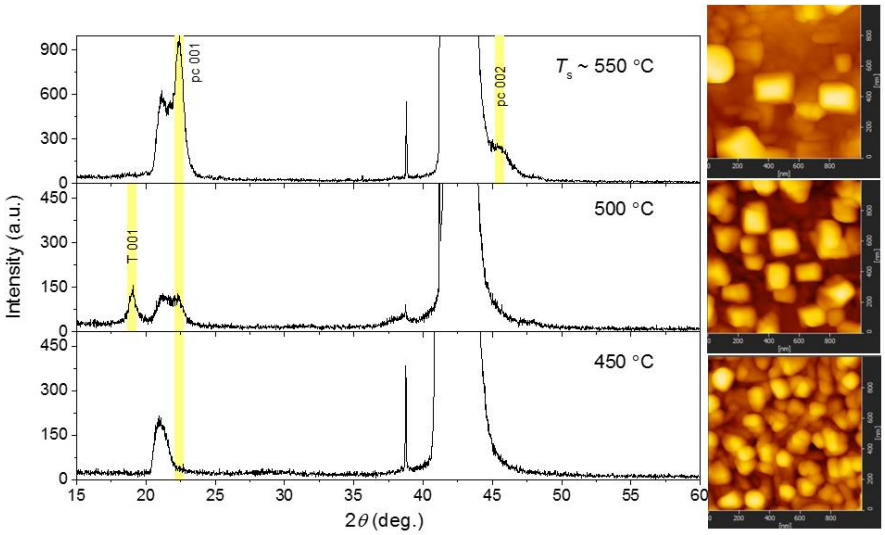

Figure 3-11 XRD profiles of BFO/TiN/MgO (001) grown at T_s = 550, 500, 450 °C. Right-hand row is corresponding AFM image.

When T_s = 550 ° C, only R phase exists. At T_s = 500 ° C, both T and pc phases exist and seems (001)-oriented films. 500 ° C is the minimum substrate temperature to get crystal BFO phase, since there is no detected peak at T_s = 450 ° C. From AFM images, BFO grain size becomes smaller as lowering T_s, which goes well with XRD profiles. Considering practical application, substrate temperature should be as low as possible. Thus we mainly focus our attention to BFO/TiN/MgO at T_s = 500 °C. Detail characterization results will be present in the following section.

In all, BFO phase can grow on (001)-oriented TiN bottom layers under wide T_s range. At high T_s region, BFO present various phases with good crystallinity, demonstrated by both XRD profiles and AFM images. While at low T_s region, BFO crystal size becomes smaller. 500 ° C is proved to be the minimum T_s to grow crystalline BFO phases. In the next section, we will mainly focus on the structure characterization of this condition prepared samples.

3.4.4 Characterization of BFO/TiN/MgO (001) grown at T_s = 500 °C

3.4.4.1 XRD profiles

Figure 3-12 shows XRD profiles and pole figures of BFO/TiN/MgO (001) films. In out-of-plane XRD profiles, two peaks around 19.01 ° and 22.27° were observed, respectively in the wide range of 2θ angles (Figure 3-12 (a)). This two peaks can be attributed to BFO T and R phases, indicating (001) orientation. In the in-plane scan with χ ~ 90 ° (Figure 3-12 (b)), there also exist the two peaks originating from (100) of T and R BFO phases, respectively. No impurity phase can be detected in both in-plane and out-of-plane scan. This results suggest that two BFO phases grew on TiN under layers together and c-axis BFO (both R and T phases) was likely perpendicular to the film plane. The lattice parameters ratio can be calculated from 001 and 100 peak positions and are listed as: T phase: c/a ~ 4.66 Å/3.78 Å ~ 1.24; R phase: c/a ~ 3.97 Å/3.96 Å ~ 1.

Pole figures measurements were also conducted (Figure 3-12 (c), (d) and (e)) to confirm the crystallographic orientation relationship between BFO and MgO substrates. First of all, four sharp 90 °- spaced diffraction spots from {101} planes of MgO substrates emerge in Figure 3-12 (c). And the same situation for both BFO T and R phase pole figures (spots instead of diffracted ring shape), indicating the epitaxial growth of BFO thin films. Besides, the diffraction peaks observed at χ ~ 51.2 ° for T and χ ~ 45.6 ° for R phase have a

four-fold symmetry, meaning a tetragonality 1.24 for T and 1.02 for R phase, respectively. Moreover, we can say that both T and R phases grow with the same crystalline orientation of MgO substrate, as demonstrated by the fact that the four φ values of T and R phases coincide with that of the MgO substrate. And their relationship can be expressed as T-BFO (001) [100] // MgO (001) [100] and R-MgO (001) [100] // MgO (001) [100].

Co-existence of T and T phases is double-checked by (011) reciprocal space mapping, as recorded in Figure 3-13. Two stripes diffracted from T and R phases, respectively, are cleared separated. From the diffraction peak position, $\tan^{-1}(c/a)$ values are calculated as 45.64 ° (for R) and 51.17 ° (for T), which are consistent with the value obtained from XRD profiles within measurement error.

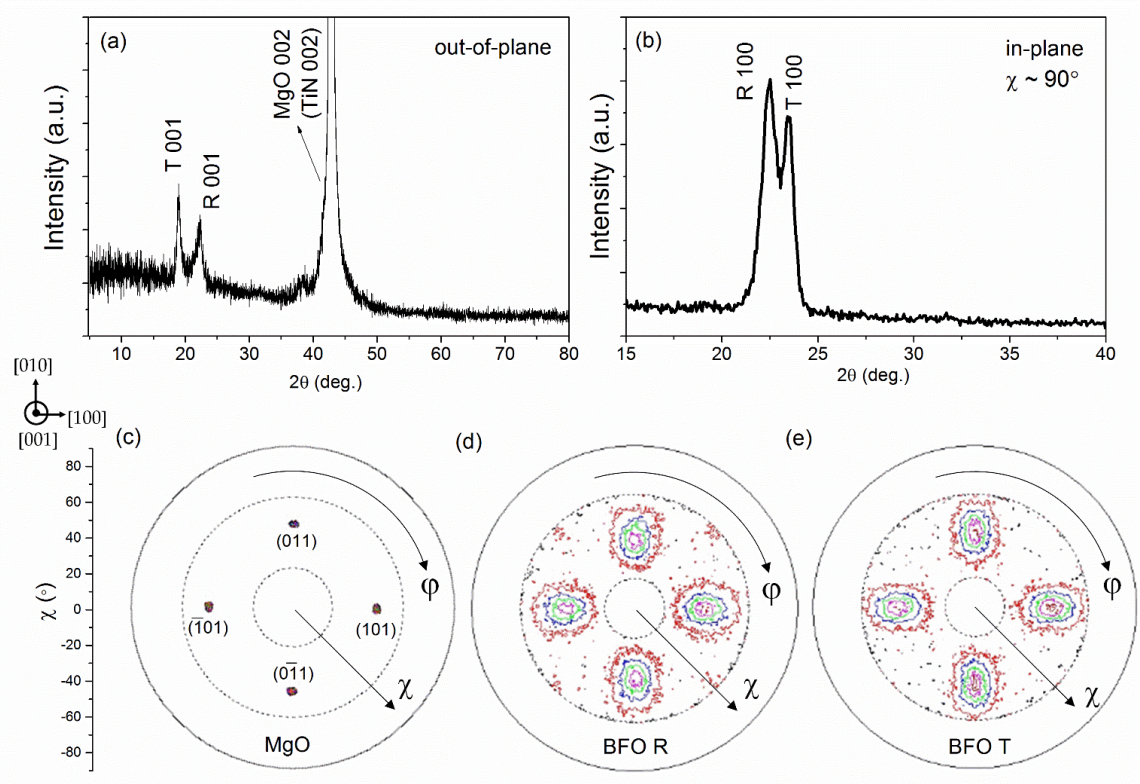

Figure 3-12 X-ray diffraction θ-2θ scan in out-of-plane (a) and in-plane (b), respectively. Pole figure maps of {101} reflection of MgO (c), BFO R phase obtained at 31.6 ° ~ 32.3 ° 2θ range (d) and BFO T phase obtained at 30.5 °~ 31.2 ° 2θ range (e).

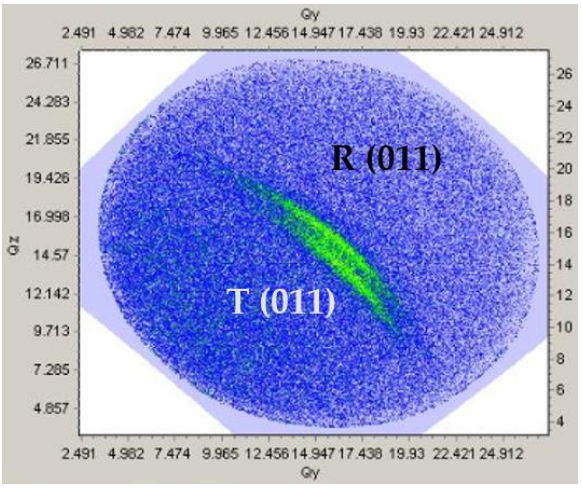

Figure 3-13 BFO (011) reciprocal space mapping with measurement centered at 2θ ~ 31 ° and χ ~ 45 ° configuration.

3.4.4.2 TEM measurement results

The BFO/TiN/MgO structures were also recorded by the cross-sectional STEM observations and images are shown in Figure 3-14. Clearly defined boundaries between T and R phase can be seen in Figure 3-14 (a). High angle annular dark-field (HAADF) images of each phase are shown in Figure 3-14 (b) and (c), respectively. At first glance there exist two obvious different c/a ratios, confirming the co-existence of T and R phases in BFO films, which agree well with previous XRD results. The c/a ratio values are calculated as 1.27 for T and 1.09 for R phase, indicated by the drawn red lines of ten-unit cell length. You may see that the exact values of lattice parameter are a bit different from those obtained in XRD profiles. This is probably due to the strain during TEM sample preparation[29].

In HAADF images shown in Figure 3-14 (d), clear interface between each layers is observed indicated by the image contrast. Besides, an unexpected layer (~ 21 nm) between BFO and TiN appears. To further help us clarify this interlayer, EDS mapping was conducted, as shown in Figure 3-15. This additional layer is found to be oxidized TiN (denote as TiNOx), suggested by the existence of Ti, N and O elements. This is due to the easy oxidization of TiN layers.[30] The right-hand column images from top to bottom are

nano-beam diffraction patterns for each layers labeled as Figure 3-14 (e), (f), (g) and (h). Both TiN and MgO layers exhibit typical squared diffracted spots, indicating fcc structure. The diffraction pattern of TiNOx layer is clearly different. However, diffraction pattern from BFO layers shares the similar arrangement to that of TiN and MgO, despite of existence of $TiNO_x$ layer. These results agree with XRD profiles and it means the (001) oriented TiN facilitates the growth of (001)-oriented BFO films.

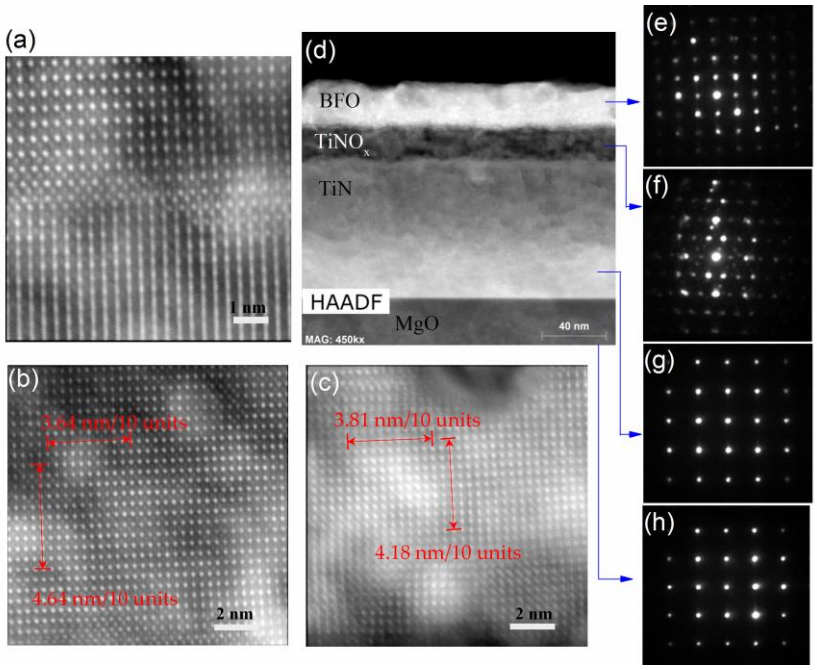

Figure 3-14 High angle annular dark-field images of T/R phase boundary (a), T phase (b), R phase (c) and BFO/TiN/MgO samples. The right-hand column shows diffraction patterns of BFO (e), TiNOx (f), TiN (g) and MgO (h), respectively.

3.4.4.3 Auger electron spectroscopy (AES) depth profiles

To further elucidate where the oxygen come from, two different samples were prepared for Auger electron spectroscopy (AES) depth profiling (as shown in Figure 3-16). One of the two samples are prepared as usual. That is a mixture gas of Ar and O_2 is supplied during the whole BFO deposition process. This film is labeled as regular sample. For the other film, initial 2 nm BFO layer is deposited in pure Ar gas without O_2 gas and

the remaining 28 nm BFO is grown in Ar and O_2 mixture as usual. We call it oxygen-less sample. From the AES depth profiles, one can see the clearly defined layered structure. By comparison, $TiNO_x$ layers exist (the sputtered time is around 50 – 70 s) regardless of different deposition conditions for the initial BFO layers. This indicates TiN layer is quite easy be oxidized and the oxygen supply is probably provided by BFO layers instead of gas atmosphere in the chamber. Besides, you may find that oxygen concentration is higher in oxygen-less sample than that of regular one. Such results can be explained by the preparation differences. We believe lots of vacancies come into being in the first 2 nm layer of the oxygen-less sample and these vacancies will further facilitate oxygen diffusion from BFO to TiN layers. So far we get the impression that TiN layer is easily oxidized as long as the deposition temperature is at 500 °C.

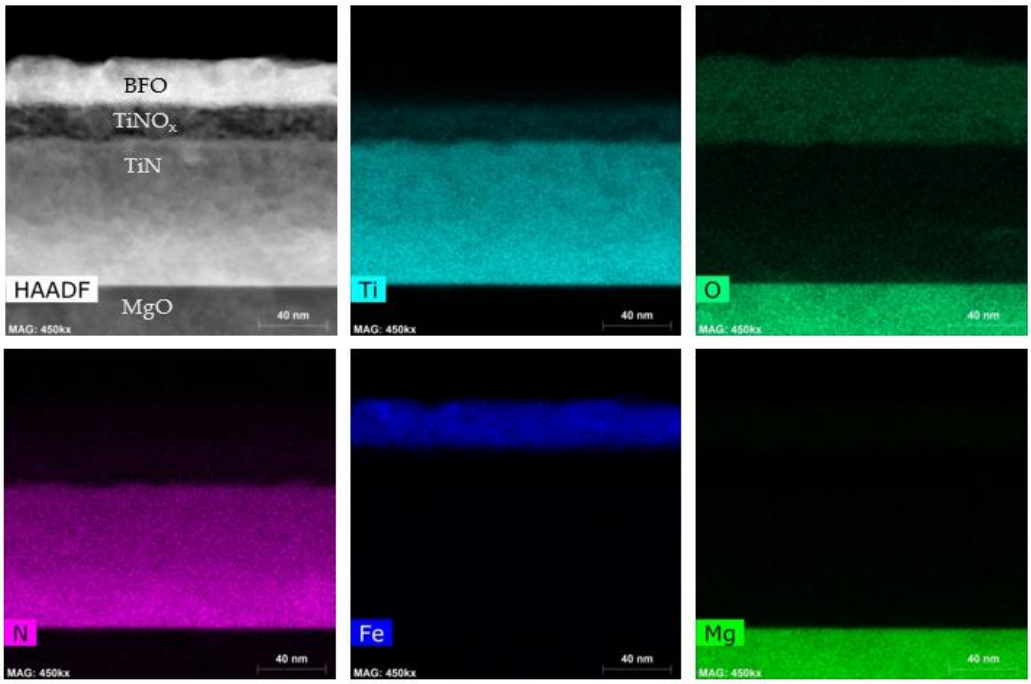

Figure 3-15 Energy dispersive spectroscopy elementary mapping of BFO/TiN/MgO (001) cross-section. Existence of Ti, O, N elements can be seen in the interlayer between BFO and TiN. Apart from this additional layer, no other phases can be attributed from the elementary mapping. Fe element is uniformly distributed in BFO layer. Bi information cannot be detected due to its large characteristic X-ray energy.

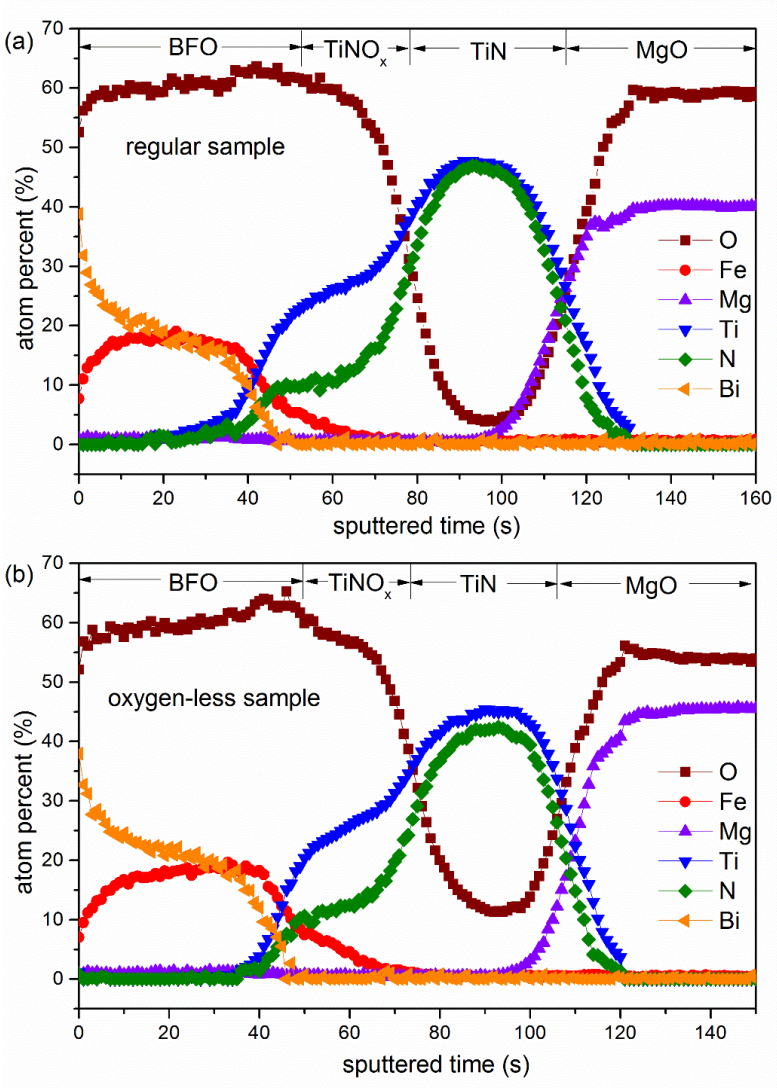

Figure 3-16 Auger electron spectroscopy (AES) depth profiles of BFO/TiN/MgO regular sample (a) and oxygen-less sample (b).

3.4.4.4 Ferroelectric measurement

Figure 3-17 shows P-E hysteresis loops of BFO films measured at room temperature. We use TiN under layer as bottom electrode and CoPt pattern as top electrode. Experiment details are described previously. The measurement has a scanning frequency of 1000 Hz. Clearly loops shows typical ferroelectric character. Our measured saturation polarization value is ~ 3.7 μC/cm^2, while the remnant polarization is only ~ 0.8 μC/cm. This value is one

order of magnitude smaller than current results obtained on STO substrates. This lack of saturation behavior may be explained by the small crystal size of BFO.[31] However the electric field, which can be applied on BFO film, is surprisingly large ~ 49 MV/cm. This is easily understood by the existence of $TiNO_x$ under layers, since it is insulator. The similar type of high field application and low remnant polarization behavior is also reported on BFO films grown on Nd-doped $SrTiO_3$ substrates, suggesting the bottom electrode affects the polarization behavior of ferroelectric thin films. The existence of $TiNO_x$ layer is proved to be helpful to prevent leak current of BFO films.

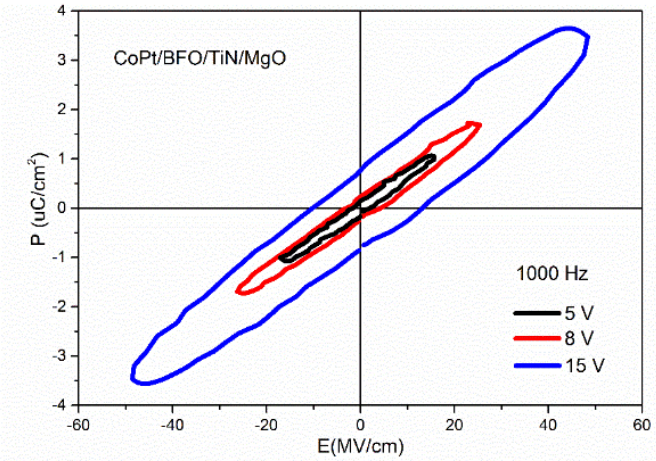

Figure 3-17 Polarization-electric field hysteresis loops of BFO measured at 1000 Hz at various voltages (5-15 V)

3.4.4.5 $BiFeO_3$ growth mechanism

Figure 3-18 depicts BFO growth process and explains the epitaxial BFO growth despite of $TiNO_x$ layers. We believed that before the deposition of BFO, $TiNO_x$ does not exist because oxygen concentration in the chamber is negligible. TiN surface will offer the nucleation sites to the first several atomic layers of BFO phase. With the growth of BFO, Ti gradually become oxidized due to the diffusion of oxygen from BFO to TiN layer. In other words, $TiNO_x$ come into being during the formation of BFO phases. First TiN film grows

epitaxially on MgO substrates (Figure 3-18 (a)) and TiN can offers nucleation sites to the first several atomic BFO layers, as show in Figure 3-18 (b). Thus the initial BFO film is epitaxial. During the BFO growth, oxygen diffuses from BFO to TiN layers and forms $TiNO_x$ interlayer (Figure 3-18 (c)). However the existence of $TiNO_x$ does not affect the BFO epitaxial growth, since BFO growth and $TiNO_x$ formation occur simultaneously (Figure 3-18 (d)).

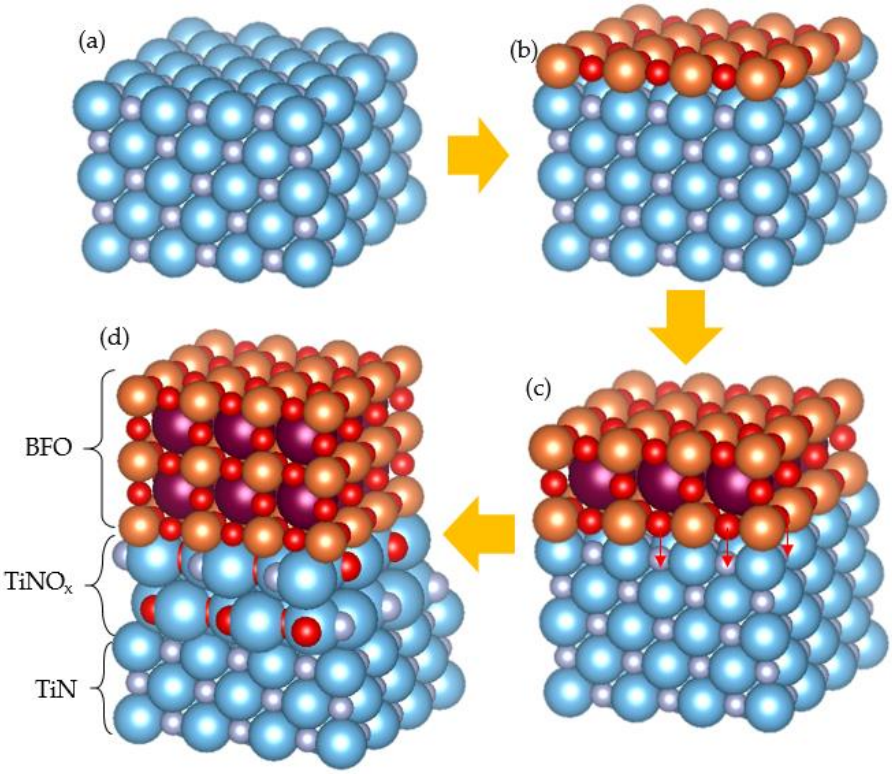

Figure 3-18 Schematic illustration of BFO growth process. (a) TiN under layer. (b) TiN layer offers nucleation sites to the first several atomic layer of BFO. (c) Oxygen diffuses from BFO layer to TiN layer as BFO grows. (d) The existence of $TiNO_x$ does not affect the epitaxial growth of BFO.

3.5 $BiFeO_3$/TiN/MgO (111) films

This section work is conducted mainly to testify TiN (111) orientation is more difficult to trigger BFO crystal growth than that of (001) orientation.

3.5.1 Experimental details

Both TiN under layer and BFO layer growth conditions in this section are the same with that on MgO (001) substrates, described in section 3.4.1.

3.5.2 Microstructure analysis

As shown in Figure 3-19, no crystalized BFO phase can be detected in this XRD profiles. Blue bar indicates possible position of BFO 111 peak.

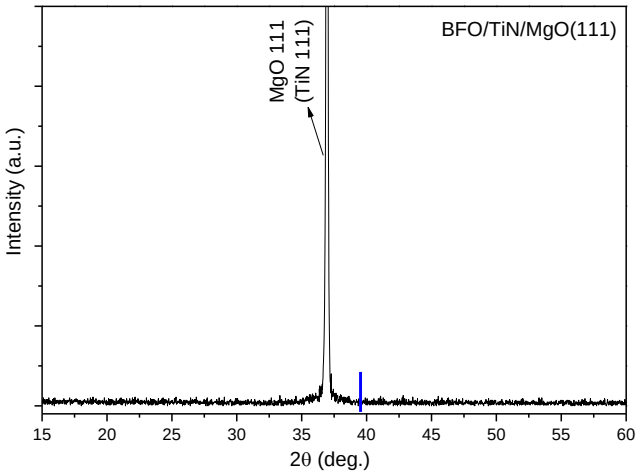

Figure 3-19 XRD profiles of BFO/TiN/MgO (111) samples. Only MgO 111 (TiN 111) peak is observed. And there are no sign of BFO peaks. Blue bar indicates possible position of BFO 111 peak.

This results is quite different from films grown on MgO (001) substrates, where epitaxial BFO phases can be obtained. However, it is similar to films grown on a-SiO_2. We think the reason lies in the orientation of TiN under layers. Once TiN presents (111) orientation, it cannot provide enough energy for BFO crystallization. Since BFO (111) surfaces are energetically unfavourable suggested by first principle calculations. On the other hand, such big differences also suggest BFO film growth is quite sensitive to under layers or substrates.

3.6 CoPt/$BiFeO_3$/TiN/MgO (001) films

Since epitaxial BFO films can be obtained on MgO (001), we continue to try couple a ferromagnetic layer CoPt on top of BFO in the hope to get magnetic interaction, such as exchange bias effect.

3.6.1 Experimental details

Both TiN and BFO films growth conditions are the same with that described in section 3.4.1. CoPt growth conditions are listed as following in table 3-4.

Table 3-4 Sputtering parameters of CoPt layers in this section work

deposition pressure	0.5 Pa
inlet sputtering gas	5 ccm
substrate temperature	200, 300, 400
sputtering power	100 mA ~ 350 V
sputtering rate	10 nm/min
thickness	10 nm

As can be seen from this table, the variations mainly focus on deposition temperature of CoPt layer, while all the growth conditions of BFO and TiN remain the same.

3.6.2 Microstructure analysis

Figure 3-20 draws XRD profiles of CoPt/BFO/TiN/MgO layered samples. According to our previous results, BFO films show epitaxial growth on TiN buffer layer. And so does this set XRD patterns. As for CoPt layer, clearly (002) peak becomes stronger as increasing CoPt deposition temperature. Normally, CoPt (111) is the most energetically favorable orientation. (002) peak appears in this work mainly because epitaxial BFO provide a c-axis orientation despite of large lateral lattice mismatch between BFO (a ~ 3.96 Å) and CoPt (a ~ 3.8 Å). Detail CoPt phase information is discussed in section 4.1.1

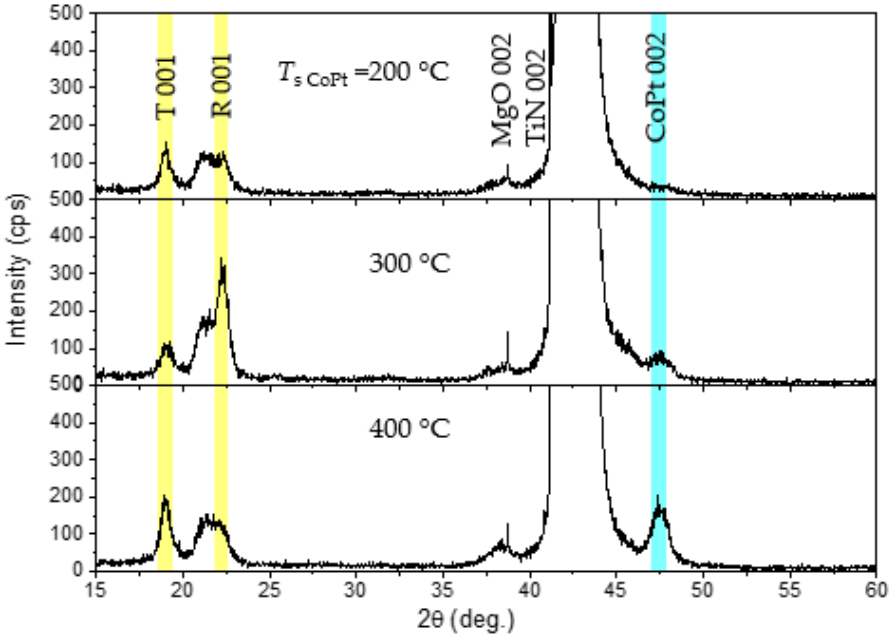

Figure 3-20 XRD profiles of CoPt/BFO/TiN/MgO (001) samples prepared at various CoPt T_s = 200, 300, 400 °C.

3.6.3 Magnetic hysteresis characterization

Magnetic hysteresis loops of single CoPt layer (10 nm) and $CoPt_{10nm}/BFO_{30nm}$/TiN layered structures are compared in Figure 3-21. Figure 3-21 (a) draws a typical hysteresis loop of CoPt films, which shows longitudinal easy axis. The saturation moment M_s value is ~ 700 emu/cc. Layered structure with various CoPt deposition temperature 200, 300, 400 °C are shown in (b), (c) and (d), respectively. At first glimpse, the overall shape remains the same despite of different deposition temperature. That is easy axis still lies in in-plane direction and samples' coercivity values H_c of in-plane are all several hundred Oersted. The only difference is the M_s gradual reduction from 700 emu/cc (RT deposition) to 540 emu/cc (200 °C), 500 emu/cc (300 °C) and 400 emu/cc (400 °C). This M_s loss is expected because of CoPt oxidization. Since CoPt layer is prepared in pure Argon gas, the oxygen source may come from oxygen dissolved in BFO layers. As we have proved in section

3.4.4.3, oxygen diffusion easily occurs. Thus the higher deposition temperature, the more severe oxidization is. Other than this, BFO antiferromagntic property seems to have no effect to ferromagnetic property of CoPt layers.

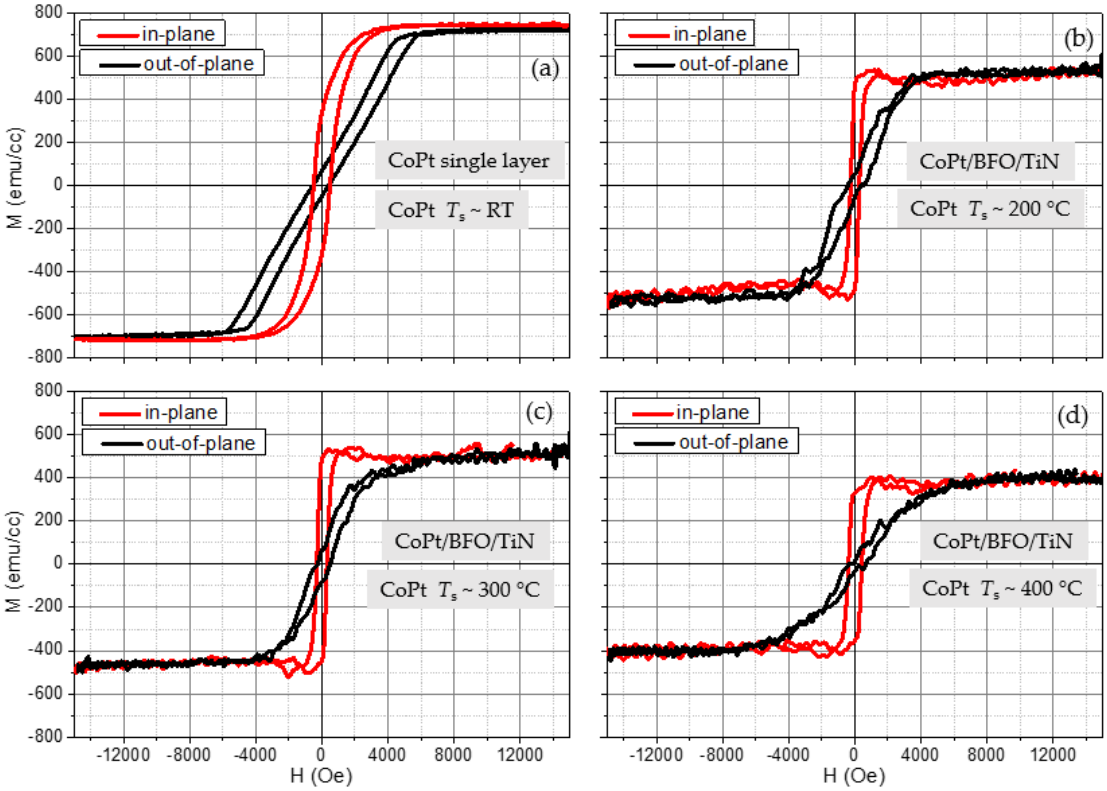

Figure 3-21 Magnetic hysteresis loops of CoPt single layer (a) and CoPt/BFO/TiN layered samples with various CoPt deposition temperature 200 °C (b), 300 °C (c) and 400 °C (d), as indicated in each loops.

Further hysteresis measurements of field-cooled layered sample are conducted to confirm whether exchange bias effect exist or not, as shown in Figure 3-22. As shown, no coercivity enhancement nor loop shift appears after field cooling treatment. This means no exchange bias effect exist in this sample. This is probably due to oxidization layer is too thick to block the interaction between BFO and CoPt films. Another thing needs to be pointed out is the M_s value decrease to ~ 400 emu/cc after field cooling treatment from 380 °C, which also indicates occurrence of oxidization.

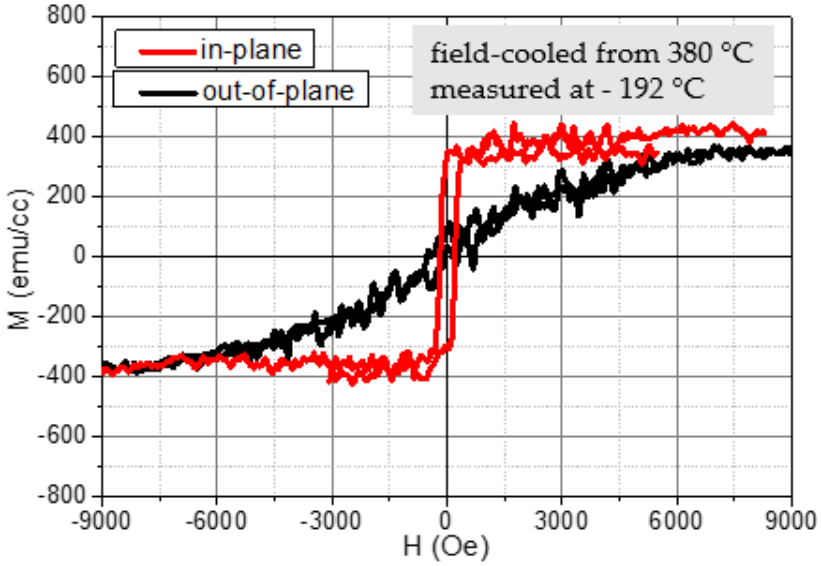

Figure 3-22 Magnetic hysteresis loop measured at – 192 °C of field-cooled CoPt (200 °C deposition)/BFO/TiN layered sample

3.7 Summary

We use TiN film as under layer to grow BFO films, since TiN can serve as bottom electrode due to its conductive property and is compatible with Si-based technology, which broadens BFO application prospect once succeed. Two kinds of TiN orientations have been prepared: (001) and (111). On (001)-oriented TiN under layers (induced by MgO (001) substrates), epitaxial BFO T and R phases can be obtained at reduced deposition temperature 500 °C. This temperature is smaller than current reported BFO epitaxial growth temperature (~ 600 – 700 °C). Their crystallographic relationship is T-BFO (001)[100] // TiN (001)[100] // MgO (001)[100] and R-BFO (001)[100] // TiN (001)[100] // MgO (001)[100], confirmed by both in-plane XRD and TEM results. On (111)-oriented TiN under layers (on a-SiO_2 substrates and MgO (111) substrates), no crystalized BFO films can be obtained. Such differences can be explained by stability variations between (001) and (111) surfaces. (001) surface have the lowest surface energy, and thus (001)-oriented BFO can be prepared on (001) TiN under layer.

Further a 10 nm ferromagnetic film CoPt is sputtered on epitaxial BFO films, in the aim to obtain exchange bias effect. However, such effect has not been detected by varying CoPt deposition temperatures. Besides, the higher CoPt deposition temperature, the severe oxidization occurs. Inspired by this, we made an improvement in next chapter by inserting Pt layer in between.

Reference

[1] F. Kubel and H. Schmid, *Acta. Cryst.* **B46**, 698 (1990)

[2] J. Wang, J. B. Neaton, H. Zheng, V. Nagarajan, S. B. Ogale, B. Liu, D. Viehland, V. Vaithyanathan, D. G. Schlom, U. V. Waghmare, N. A. Spaldin, K. M. Rabe, M. Wuttig, R. Ramesh, *Science* **299**, 1719 (2003)

[3] J. Li, J. Wang, M. Wuttig, R. Ramesh, N. Wang, B. Ruette, A. P. Pyatakov, A. K. Zvezdin and D. Viehland, *Appl. Phys. Lett.* **84**, 5261 (2004)

[4] K. Y.Yun, M. Noda, M. Okuyama, H. Saeki, H. Tabata and K. Saito, *J. Appl. Phys.* **96**, 3399 (2004)

[5] K. Y. Yun, D. Ricinschi, T. Kanashima and M. Okuyama, *Appl. Phys. Lett.* **89**, 192902 (2006)

[6] J. C. Yang, Q. He, S. J. Suresha, C. Y. Kuo, C. Y. Peng, R. C. Haislmaier, M. A. Motyka, G. Sheng, C. Adamo, H. J. Lin, Z. Hu, L. Chang, L. H. Tjeng, E. Arenholz, H. J. Podraza, M. Bernhagen, R. Uecker, D. G. Schlom, V. Gopalan, L. Q. Chen, C. T. Chen, R. Ramesh and Y, H, Chu, *Phys. Rev. Lett.* **109**, 247606 (2012)

[7] L. W. Martin, Y. H. Chu, Q. Zhan, R. Ramesh, S. J. Han, S. X. Wang, M. Warusawithana and D. G. Schlom, *Appl. Phys. Lett.* **91**, 172513 (2007)

[8] Y. H. Chu, L. W. Martin, M. B. Holcomb, M. Gajek, S. J. Han, Q. He, N. Balke, C. H. Yang, D. Lee, W. Hu, Q. Zhan, P. L. Yang, A. F. Rodríguez, A. Scholl, S. X. Wang and R. Ramesh, *Nature Mater.* **7**, 478 (2008)

[9] S. S. Rao, J. T. Prater, F. Wu, C. T. Shelton, J. P. Maria and J. Narayan, *Nano Lett.* **13**, 5814 (2013)

[10] C. B. Eom, A. F. Marshall, S. S. Laderman, R. D. Jacowitz and T. H. Geballe, *Science* **249**, 1549 (1990)

[11] R. R. Das, D. M. Kim, S. H. Baek, C. B. Eom, F. Zavaliche, S. Y. Yang, R. Ramesh and Y. B. Chen, X. Q. Pan, X. Ke, M. S. Rzchowski and S. K. Streiffer, *Appl. Phys. Lett.* **88**, 242904 (2006)

[12] Y. H. Lee, C. S. Liang and J. M. Wu, *Electro. Solid State Lett.* **8**, F55 (2005)

[13] J. Chao, J. Xing, B. He, Z. Zhang, Y. Duan, J. Gu, *Adv. Mater. Research* **684**, 64 (2013)

[14] H. W. Chang, F. T. Yuan, Y. C. Yu, S. Y. Tu, P. C. Lin, C. R. Wang, A. B. Yang, C. S. Tu and S. U. Jen, *J. Appl. Phys.* **117**, 17C721 (2015),

[15] S. K. Singh, R. Ueno, H. Funakubo, H. Uchida, S. Koda and H. Ishiwara, *Jpn. J. Appl. Phys.* **39**, L1231 (2005)

[16] F. Tyholdt, H. Fjellvåg, A. E. Gunnæs and A. Olsen, *J. Appl. Phys.* **102**, 074108 (2007)

[17] R. Ueno, S. Okaura, H. Funakubo and K. Saito, *Jpn. J. Appl. Phys.* **39**, L1231 (2005)

[18] S. Y. Yang, F. Zavaliche, L. M. Ardabili, V. Vaithyanathan, D. G. Schlom, Y. J. Lee, Y. H. Chu, M. P. Cruz, Q. Zhan, T. Zhao, and R. Ramesh, *Appl. Phys. Lett.* **87**, 102903 (2005)

[19] Y. Wang, Y. Lin and C. W. Nan, *J. Appl. Phys.* **104**, 123912 (2008)

[20] V. Shelke, V. N. Harshan, S. Kotru and A. Gupta, *J. Appl. Phys.* **106**, 104114 (2009)

[21] V. Shelke, D. Mazumdar, G. Srinivasan and A. Gupta, *J. Appl. Phys.* **109**, 07D914 (2011)

[22] H. Y. Go, N. Wakiya, H. Funakubo, K. Satoh, M. Kondo, J. S. Cross, K. Maruyama, N. Mizutani and K. Shinozaki, *Jpn. J. Appl. Phys.* **46**, 3491 (2007)

[23] R. Zheng, X. Gao, J. Wang and S. Ramakrishna, *J. Am. Ceram. Soc.* **91**, 463 (2008)

[24] S. Ryu, J. Y. Son, Y. H. Shin, H. M. Jang and J. F. Scott, *Appl. Phys. Lett.* **95**, 242902 (2009)

[25] K. Lal, A. K. Meikap, S. K. Chattopadhyay, S. K. Chatterjee, M. Ghosh, K. Baba and R. Hatada, *Physica B*, **307**, 150 (2001)

[26] J. Narayan, P. Tiwari, X. Chen, J. Singh, R. Chowdhury and T. Zheleva, *Appl. Phys. Lett.* **61**, 1290 (1992)

[27] J. Graciani, J. Fdez Sanz, T. Asaki, K. Nakamura and J. A. Rodriguez, *J. Chem. Phys.* **126**, 244713 (2007)

[28] R. I. Eglitis, *Ferroelectrics* **483**, 53 (2015)

[29] Z. Chen, Z. Lou, Y. Qi, P. Yang, S. Wu, C. Huang, T. Wu, J. Wang, C. Gao, T. Sritharan and L. Chen, *Appl. Phys. Lett.* **97**, 242903 (2010)

[30] D. B. Lee, G. Y. Kim and J. K. Lee, *Met. Mater. Int.* **9**, 43 (2003)

[31] W. N. Su, D. H. Wang, Q. Q. Cao, Z. D. Han, J. Han, J. Yin, J. R. Zhang and Y. W. Du, *Appl. Phys. Lett.* **91**, 092905 (2007)

Chapter 4 Perpendicular exchange coupling in $BiFeO_3$/CoPt layered structures

4.1 Introduction

Perpendicular magnetized system is always a pursuit for its relatively higher density compared to longitudinal direction. Besides, it can also reduce required electric current density in spin-transfer mode.[1] To deal with thermal instability problem, material with relatively large uniaxial magnetocrystalline anisotropy energies are needed. In this chapter, I will involves a high perpendicular anisotropy material – cobalt platinum CoPt.

4.1.1 Structure and characteristics of CoPt

CoPt alloy can take on many structures, such as A1, $L1_0$, $L1_1$, $L1_2$ and other hexagonal metastable ordered structures.[2] Here I mainly focus on A1 and $L1_0$ structures. A1 structure crystalize in face-centered cubic (fcc), where Co or Pt atoms randomly occupy at fcc sites. Thus A1 is a disordered structure. Its structure details are listed in Figure 4-1. Usually upon annealing, A1 CoPt alloy will transfer to $L1_0$ ordered structure, where Co and Pt atom planes alternate with each other along c-axis, as shown in Figure 4-2. By comparison, we can know that once ordered, c/a ratio becomes smaller than 1. Besides, (002) peak of A1 phase ~ 47.8° splits to (020) and (002) two peaks in $L1_0$ phase at 47.8° and 49.1°, respectively. Another character of $L1_0$ phase is the appearance of (001) sublattice peak at 23.9°. General a parameter S caller long-range order degree are used to evaluate the ordering degree and it can be calculated from the XRD data. For a certain peak, the integrated intensity (I) is proportional to structure factor (F), the complex conjugate (F^*), Lorentz-polarization factor (L) and absorption factor (A).[3] Thus $I_{(001)}/I_{(002)} = (FF^*LA)_{(001)}/(FF^*LA)_{(002)} = \{|F^2_{(001)}|/|F^2_{(002)}|\}$

$\{(LA)_{(001)}/(LA)_{(002)}\}$. Here $|F^2_{(001)}|/|F^2_{(002)}|$ can be further expressed as $4S^2(f_{Co} - f_{Pt})/4(f_{Co}+f_{Pt})$, where f is atomic scattering factor for Co and Pt atoms, respectively. Combining the above, S is given as $(I_{(001)}/I_{(002)})^{1/2}\times((LA)_{(001)}/(LA)_{(002)})^{1/2}\times((f_{Co}-f_{Pt})/(f_{Co}+f_{Pt}))$. L and A is calculated from equation $L = (1+\cos^2 2\theta)/(\sin^2\theta\cos\theta)$ and $A = [1-e^{-\mu(2\Lambda/\sin\theta)}]/2\mu$, where μ is linear absorption coefficient and 2Λ/sinθ is X-ray path length. The calculated S value is between 0 (disordered) and 1 (fully ordered).

Formation of $L1_0$ ordered phase requires sufficient energy to ensure atom diffusion. Thus high temperature deposition or post annealing treatment are necessary. According to Co-Pt binary phase diagram[4], the critical temperature T_c for CoPt is 825 °C, which is the highest temperature needed for ordering. Besides, the Co/(Co + Pt) ratio needs to be refined within 41% to 74 %. The more concentration shift from 50%, the harder ordering is.

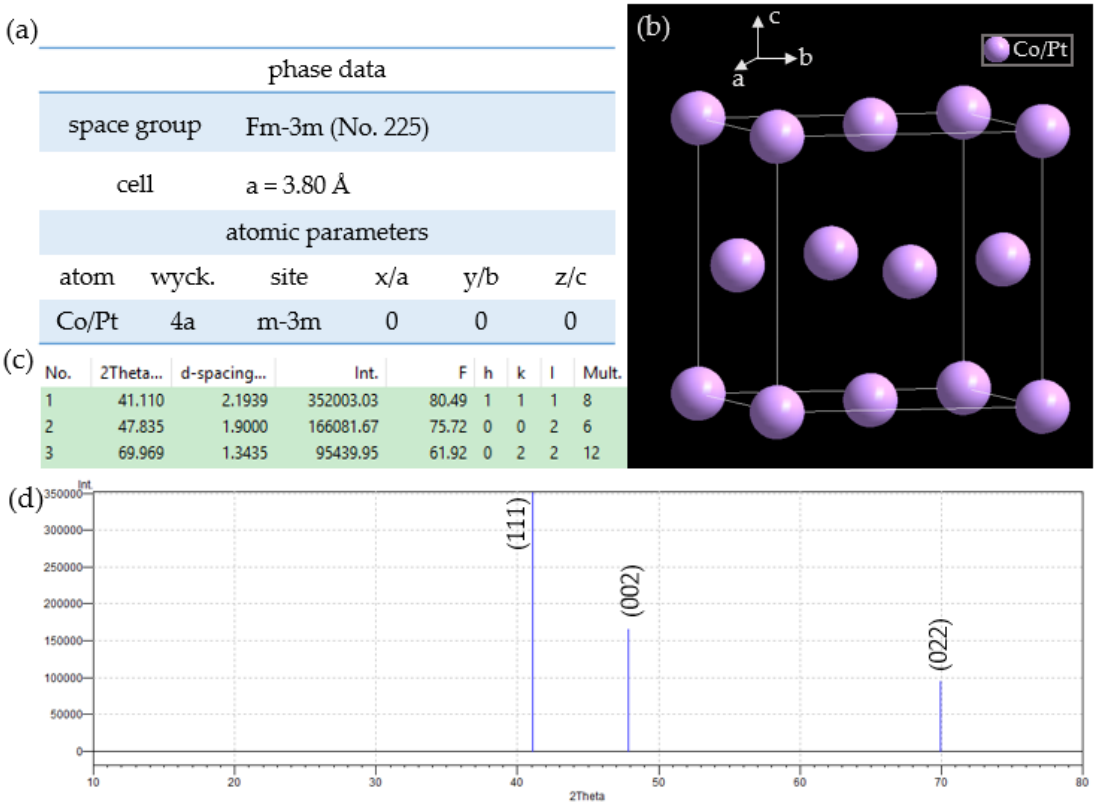

Figure 4-1 Face-centered cubic phase (A1) of CoPt alloy. (a) Detail structure information; (b) Cubic unit cell schematic structure; (c) Calculated diffraction peak information; (d) Calculated diffraction pattern.

(a)

phase data					
space group	P4/mmm (No. 123)				
cell	a = 3.80 Å ; c = 3.71 Å				
atomic parameters					
atom	wyck.	site	x/a	y/b	z/c
Co	2e	mmm.	0	0.5	0.5
Pt 1	1a	4/mmm	0	0	0
Pt 2	1c	4/mmm	0.5	0.5	0

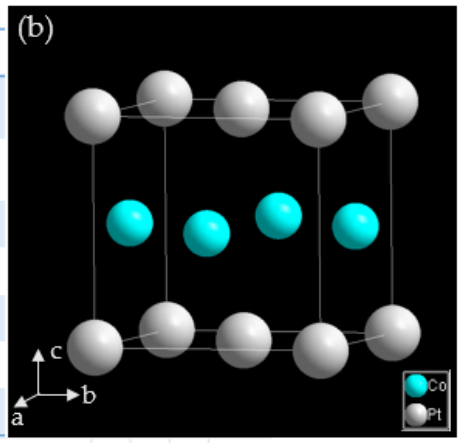

(c)

No.	2Theta...	d-spacing...	Int.	F	h	k	l	Mult.
1	23.967	3.7100	402747.63	96.21	0	0	1	2
2	33.318	2.6870	362466.94	91.66	1	1	0	4
3	41.460	2.1762	1502938.75	167.91	1	1	1	8
4	47.835	1.9000	497347.28	160.49	0	2	0	4
5	49.071	1.8550	230631.16	159.10	0	0	2	2
6	54.194	1.6911	195956.55	82.10	0	2	1	8
7	60.610	1.5266	143196.52	79.64	1	1	2	8
8	69.969	1.3435	158716.34	138.31	2	2	0	4
9	70.950	1.3273	304915.94	137.46	0	2	2	8
10	75.148	1.2632	80818.09	74.75	2	2	1	8
11	77.054	1.2367	19035.60	74.17	0	0	3	2
12	79.737	1.2017	70474.80	73.39	1	3	0	8

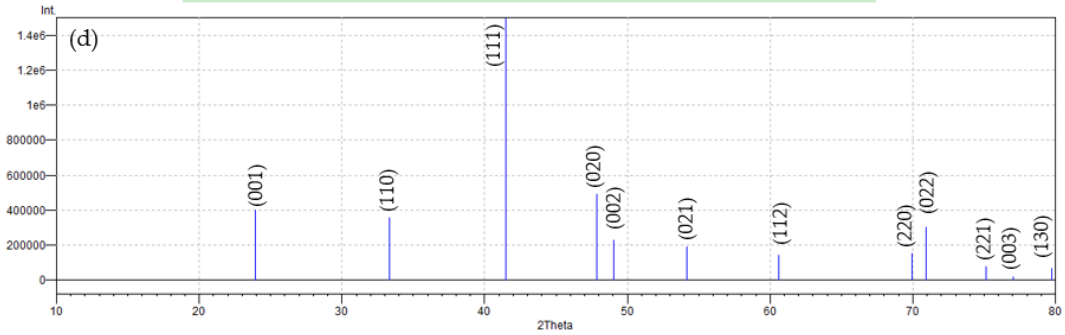

Figure 4-2 Tetragonal phase ($L1_0$) of CoPt alloy. (a) Detail structure information; (b) Tetragonal unit cell schematic structure; (c) Calculated diffraction peak information; (d) Calculated diffraction pattern.

Recent research reveals that a reduced T_c is applicable to ultra-thin film case.[5] However the ultra-thin film dimension will hinder the ordering process mainly due to the limited heat absorption.[6]

Once ordering, $L1_0$ structure shows large perpendicular magnetocrystalline anisotropy. The intrinsic magnetic properties are listed as: K_1 ~ 4.9 * 107 ergs/cc and M_s ~ 800 emu/cc.[7]

4.1.2 Objectives in this chapter

At the end of last chapter, although we prepared CoPt/BFO bilayers, no significant magnetic property change (neither coercivity enlargement nor hysteresis shift) has been detected. This indicates antiferromagnetism of BFO has no expected influence to the ferromagnetism of CoPt, probably due to the formation of oxidization layer in between.

In this chapter, we sputtered CoPt layer first and then followed by in-situ annealing, which induce perpendicular anisotropy. To prevent oxidization, an ultra Pt layer was prepared afterwards. At last, deposited BFO films on the top. In this way, we manage to produce direct interaction between BFO and CoPt films and can find out exotic magnetic interface effects, such as exchange coupling and exchange bias effect. As far as we know, there have been no report about magnetic property of BFO in perpendicular direction.

4.2 Experimental details

4.2.1 CoPt preparation details

$Co_{0.5}Pt_{0.5}$ alloy film is prepared by bombing Co and Pt metal simultaneously. We use 2 inch Co metal target and Pt is supplied from Pt plate, as shown in Figure 4-3 (a). Co and Pt ratio is adjusted by the width of Pt plate. In our experiment, 17mm width Pt plate is used to realize Co:Pt ~ 1:1 ratio in the film. The Co and Pt atom ratio is measured by Energy-dispersive spectroscopy (EDS), as shown in Figure 4-4. In order to keep atom ratio consistent, frequent check-up about the target (especially Pt deficiency) is needed. DC power supply is used and the current is controlled as 100 mA with voltage ~ 310 – 330 V. The growth rate is ~ 10 nm/min and working pressure is 0.6 Pa.

The substrate temperature of CoPt is 300 – 400 °C, where only non-ordered magnetic phase A1 (Co and Pt atoms randomly occupy at fcc units) grows. To realize perpendicular anisotropy, in-situ annealing process is followed without breaking vacuum state. We apply

700 -750 °C annealing for 3 hours. This high temperature can overcome energy barrier for atomic diffusion and form ordered magnetic phase $L1_0$, which consists of monoatomic layer of Co and Pt alternating along c-axis. [8,9] The order degree can be quantified by the order parameter S, as we described previously.

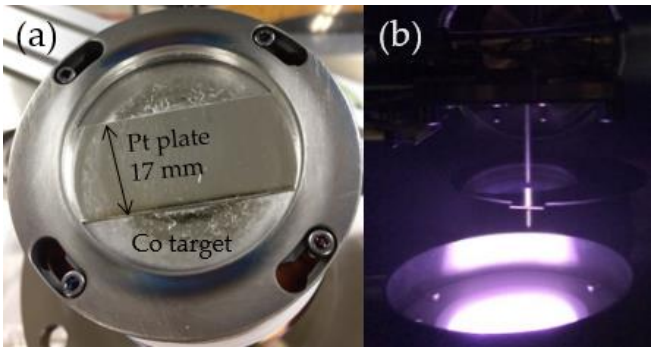

Figure 4-3 (a) CoPt target (b) CoPt deposition plume

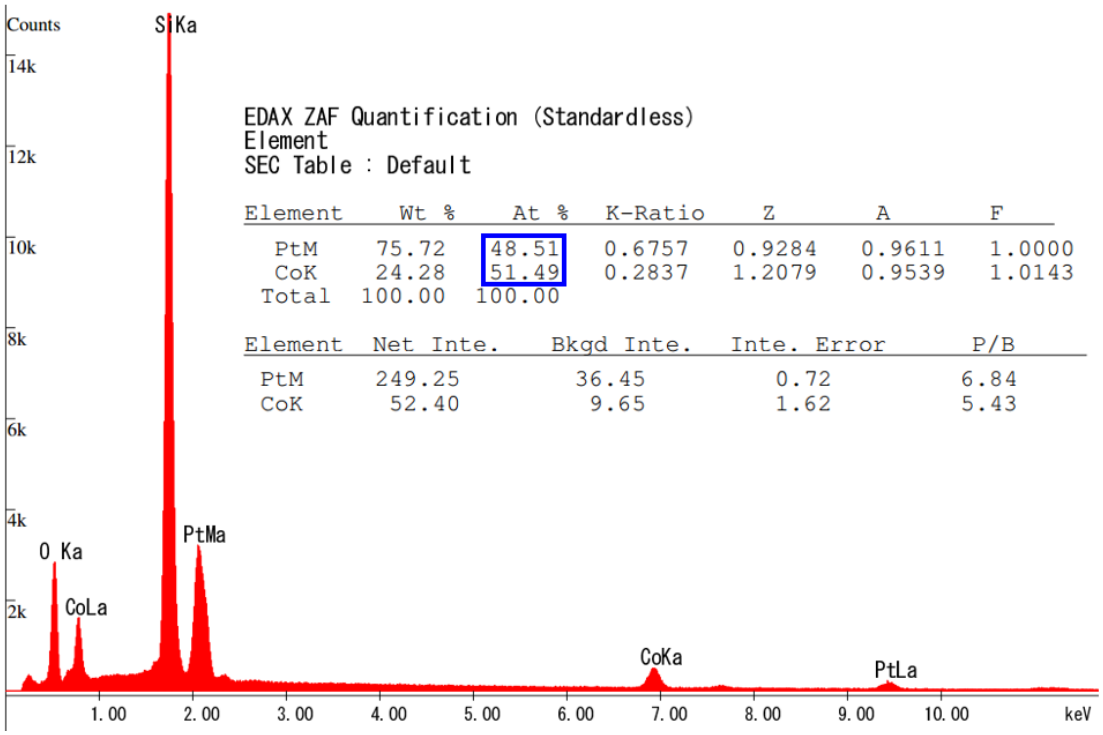

Figure 4-4 Energy dispersive spectroscopy (EDS) results of CoPt films deposited from Co 2-inch target with Pt 1.7 mm plate.

4.2.2 Pt preparation details

Pt layer is prepared in our experiment as needed. The Pt target size in 1 inch (Figure 4-5 (a)) due to the high deposition rate of Pt metal. To precisely control the Pt layer

thickness, DC deposition current is merely 20 mA, while the corresponding voltage is ~ 290 – 320 V. The working pressure is 0.3 Pa and substrate temperature is held at 300 °C. Pt deposition plume picture is shown in Figure 4-5 (b).

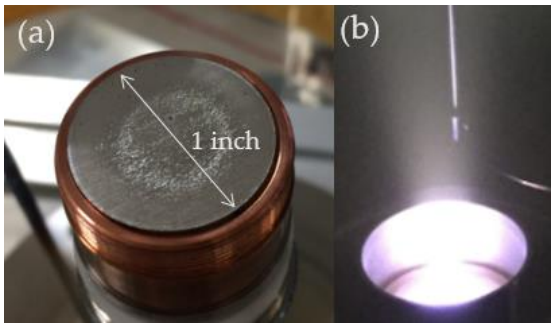

Figure 4-5 (a) Pt 1-inch target (b) Pt deposition plume

4.2.3 Layered structure preparation details

Growth condition of each films are summarized in Table 4-1.

Table 4-1 Growth conditions of CoPt layers in this section work

	CoPt		Pt	$BiFeO_3$
substrate	MgO (001)			
base pressure	< 5.0 ×10^{-5} Pa		< 8.0 ×10^{-5} Pa	< 5.0 ×10^{-5} Pa
inlet sputtering gas	3 ccm		3 ccm	5 ccm
sputtering power	100 mA ~ 350 - 360V		20 mA ~ 280- 290V	100 W
deposition pressure	0.5 Pa		0.3 Pa	0.2 Pa
thickness	10 nm	4 nm	0.5, 1, 1.5, 2 nm	30 nm
substrate temperature	300 °C	400 °C	300 °C	600 °C
annealed temperature	750 °C	700 °C	none	

In this chapter, all of the samples are prepared in four steps. First, CoPt layers are sputtering at low T_s ~ 300 – 400 °C depending thickness. Then the CoPt layers are in-situ post annealed at high temperature T_a ~ 700 – 750 °C for structure ordering. Afterwards, an ultra-thin layer (~ 0.5 – 2 nm) Pt films are deposited. This Pt layer can both prevent CoPt oxidation during BFO deposition and promote BFO epitaxial growth as well. Last step is

to prepare 30 nm BFO layers by sputtering on the top. The variates on this chapter work is thickness of CoPt and Pt. Depending on CoPt thickness, T_s and T_a are different mainly due to prevention of island structures. Usually, for 4 nm CoPt layer, T_s and T_a are 400 and 700 °C, respectively. In 10 nm CoPt case, T_s and T_a are selected to be 300 and 750 °C, respectively. For 10 nm CoPt case, Pt layer thickness is varied from 0.5, 1, 1.5, 2 nm.

4.3 Perpendicular anisotropy enhancement

In this chapter, we will discuss the existence of BFO films may affect the perpendicular anisotropy of this layered structures.

4.3.1 Sample description

I'll compare four samples in this section. For easy understanding, sample illustration are shown in Figure 4-6. Figure 4-6 (a) is CoPt film grown at low temperature (~ 300 °C), with disordered A1 structure, while (b) is further post-annealed at high temperature (~ 750 °C), inducing $L1_0$ ordered structure. As we have mentioned, ultra-thin Pt layer is used to prevent oxidization of CoPt, and thus layered structure (c) and (d) are prepared. As for the Pt thickness, films with 0.5 – 2 nm Pt all show similar tendency. In this section, we just select 0.5 nm as an example. One more thing need to be emphasized about preparation of sample (c). This film is made as a control sample for (d). Thus everything growth condition is the same except no BFO deposition. This includes keeping chamber atmosphere (inserting O_2 and Ar gas mixture) for the same time to that of sample (d) after Pt sputtering and deposition temperature of each layer.

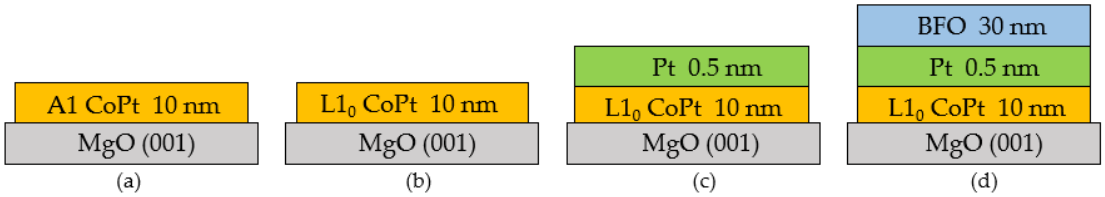

Figure 4-6 Sample illustration of four kinds of films.

4.3.2 Structure and magnetic measurements

Structure and magnetic characterization are conducted by XRD and VSM method. Figure 4-7 shows the XRD profiles of four samples, in the same sequence of illustration of Figure 4-6. Since Pt/CoPt sample (Figure 4-7 (c)) is measured by a different XRD machine, its intensity is different from the other three. Besides, MgO (001) peak cannot be detected. However these minor differences have no influence on the CoPt diffraction peak analysis. Clearly, without annealing there is no CoPt (001) peak, which is a characteristic peak of $L1_0$ structure.

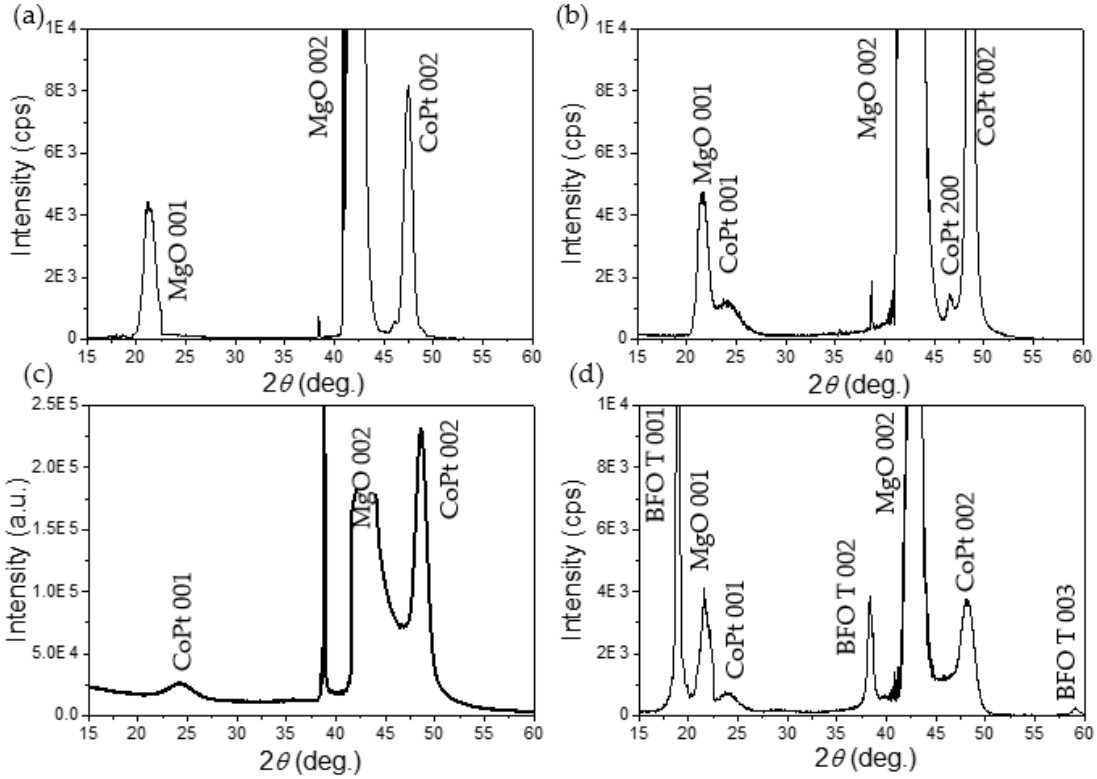

Figure 4-7 XRD profiles of each sample. (a) A1 $CoPt_{10nm}$/MgO. (b) $L1_0$ $CoPt_{10nm}$/MgO. (c) $Pt_{0.5nm}$/$L1_0$ $CoPt_{10nm}$/MgO. (d) BFO_{30nm}/$Pt_{0.5nm}$/L10 $CoPt_{10nm}$/MgO.

The same results obtained from magnetic hysteresis loops, as compared in Figure 4-8. Non-ordered A1 structure is longitudinal anisotropy (Figure 4-8 (a)), while $L1_0$ CoPt shows isotropic (Figure 4-8 (b)). This is probably due to the low ordering degree, which is also suggested from XRD pattern (Figure 4-7 (b)). If we compare $L1_0$ CoPt MH curves to that of

BFO/Pt/$L1_0$ CoPt layers, clear perpendicular anisotropy is enhanced. The anisotropy constant K is roughly calculated as 1.9 *10^6 erg/cm^3. Compared from this two samples, existence of BFO film clearly increases perpendicular anisotropy. However, the Pt/$L1_0$ CoPt layers also shows perpendicular anisotropy and its value is calculated as 3.6 *10^6 erg/cm^3. This result seems BFO film reduces the perpendicular anisotropy to some extent. We believe such reduction mainly originates from oxidization of CoPt, indicated by the smaller M_s value in Figure 4-8 (d).

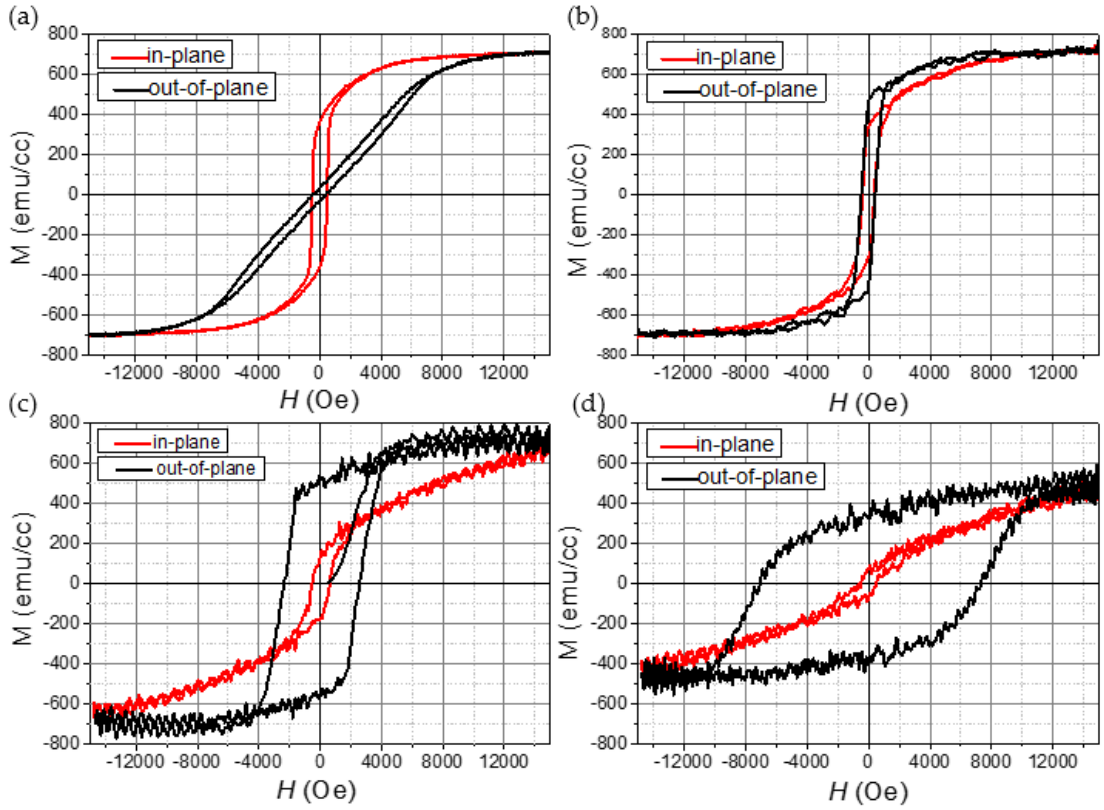

Figure 4-8 Magnetic hysteresis loops of each sample. (a) A1 $CoPt_{10nm}$/MgO. (b) $L1_0$ $CoPt_{10nm}$/MgO. (c) $Pt_{0.5nm}$/$L1_0$ $CoPt_{10nm}$/MgO. (d) BFO_{30nm}/$Pt_{0.5nm}$/$L1_0$ $CoPt_{10nm}$/MgO.

4.3.3 Summary and discussions

In this section, we observe both the structure and magnetic property difference between disordered A1 CoPt and $L1_0$ CoPt films. As the same with reported, $L1_0$ structure can induce perpendicular anisotropy. Further perpendicular anisotropy is enhanced with

the existence of BFO films. Such enhancement can be understood from the following two aspects.

First is interface effect during BFO deposition. As can be seen from the illustration in Figure 4-9. Before BFO is prepared, CoPt layer is already ordered and perpendicular anisotropy is induced. The deposition temperature (600 °C) of BFO is higher than its $T_{Néel}$ (~ 380 °C), and thus at this condition BFO is paramagnetic state. As it cools down, CoPt affects the first monolayer of BFO and align them is perpendicular direction. This magnetized BFO spin in return produce an effect on CoPt layer, and enhances the perpendicular anisotropy.

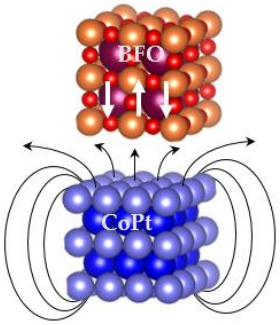

Figure 4-9 Schematic illustration of spin configuration of CoPt and BFO layers.

This interface effect during BFO deposition is further suggested by hysteresis comparison between as-deposition and field-cooled samples, as shown in Figure 4-10. One can see that after field-cooling treatment, no exchange bias effect is detected (neither loop shift nor H_c enlargement). This means that the as-deposited sample has already experienced field cooling treatment during BFO deposition.

The other factor may lie in the tensile strain imposed by BFO to CoPt layers. It has been reported that tensile strain can increase perpendicular anisotropy of CoPt film in CoPt/AlN multilayer structures.[10] If we compare the in-plane lattice parameters of BFO (~ 3.8 Å) and CoPt (~ 3.7 Å) layers, we can clearly see that BFO also impose a tensile to CoPt layer. Thus we believe such tensile strain is also part of the reason to explain the

perpendicular anisotropy enhancement phenomenon, although such strain cannot be detected from XRD profiles.

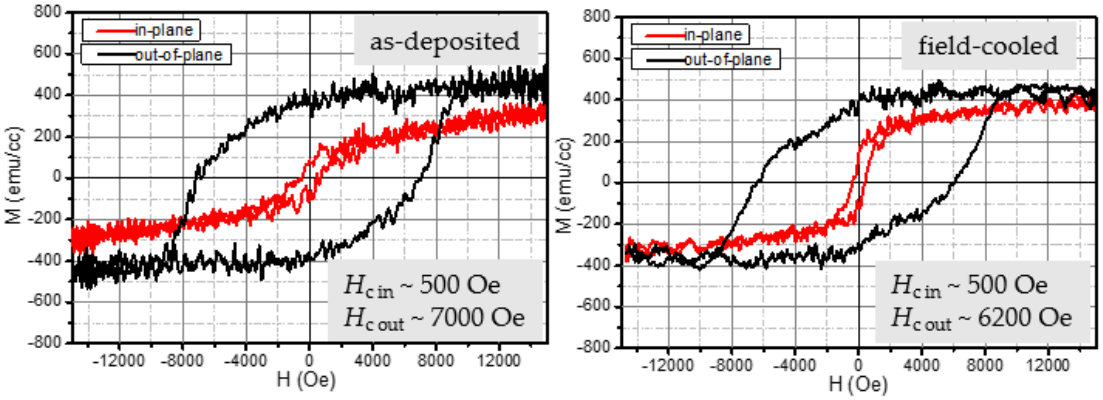

Figure 4-10 Magnetic hysteresis loops comparison between as-deposited and field-cooled $BFO_{30nm}/Pt_{1nm}/CoPt_{10nm}$ layered films.

4.4 Perpendicular exchange bias effect

Perpendicular exchange bias effect has been observed in two samples. Exchange bias effect, also known as unidirectional exchange anisotropy, is an interface coupling effect between ferromagnetic and anti-ferromagnetic layers. The manifestation of exchange bias is (1) a shift of hysteresis loops along negative magnetic field direction after field cooling process and (2) a coercivity enhancement of field-cooled samples compared to that of before. Sometimes there is also accompanied by training effect. Our exchange bias effect was observed in perpendicular direction (easy-axis of $L1_0$ ordered CoPt).

4.4.1 $BiFeO_{3\ 30nm}/Pt_{2nm}/CoPt_{10nm}$/MgO (001) films

Out-of-plane XRD profile of this sample is depicted in Figure 4-11. Both (001) and (002) diffraction peaks of CoPt are observed, indicating $L1_0$ well-ordered structure. Besides, CoPt (200) peak also appears. This suggests a small part of ordered CoPt are in the longitudinal direction, and this may originate from large mismatch between MgO substrates (4.2 Å) and CoPt lattice (3.9 Å for A1 structure). For BFO phase, (001)-textured

tetragonal structure labeled as T is detected. In all, this XRD shows (001)-textured BFO/CoPt growth.

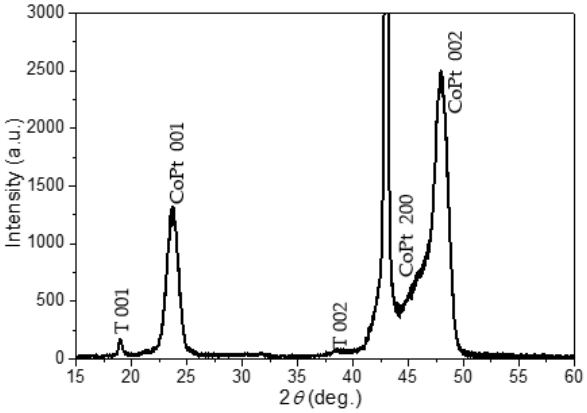

Figure 4-11 Out-of-plane XRD profile of $BFO_{30nm}/Pt_{2nm}/CoPt_{10nm}$ films.

The VSM measurements are recorded in Figure 4-12. Right-hand side is as-deposited measurement and left-hand side is 5000 Oe field-cooled result. One can clearly see that easy axis mostly lies in out-of-plane and a small part in in-plane direction. This results go well with XRD pattern (existence of (001) and (200) peaks). For the as-deposited condition, coercivity in out-of-plane direction is 7000 Oe. However, the coercivity decreases a bit to 62000 Oe after field cooling. The existence of perpendicular exchange bias is difficult to tell, since the measurement resolution is not that high. Besides, we need to know that the loop shape changes after field cooling. That is the squareness of the hysteresis decreases upon field-cooling.

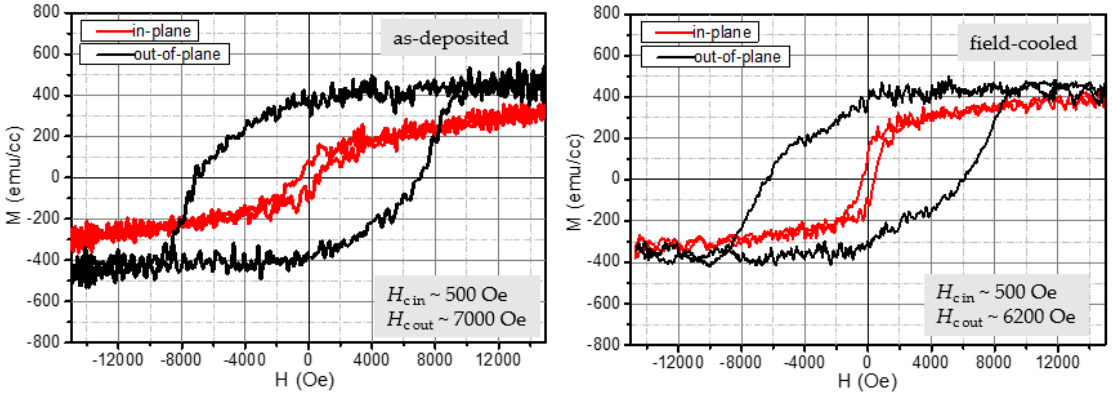

Figure 4-12 VSM hysteresis loop measurements of as-deposited and field-cooled $BFO_{30nm}/Pt_{2nm}/CoPt_{10nm}$ films.

This sample was further cut into small pieces (~ 1 mm * 2 mm) for more accurate measurements by SQUID-VSM. This time we only focus on out-of-plane results and check whether exchange bias exists or not in perpendicular direction. As shown in Figure 4-13, measurements were conducted at 50 K and 300 K, respectively. At low temperature (Fgiure 4-12 (a)), there is an obvious loop shift, indicating exchange bias effect. The coercivity and exchange bias value is 5522 Oe and 646 Oe, respectively. However, when measuring at room temperature, the exchange bias effect disappear and the coercivity value is only 2100 Oe. This may because the CoPt layer thickness is a bit large (~ 10 nm). Besides, if we compare the results measured by VSM and SQUID, we find that the coercivity decreases very quickly, probably because of the training effect. A similar phenomenon was also reported in BFO/NiFe bilayer structures,[11] where the exchange bias value shows an exponential decay.

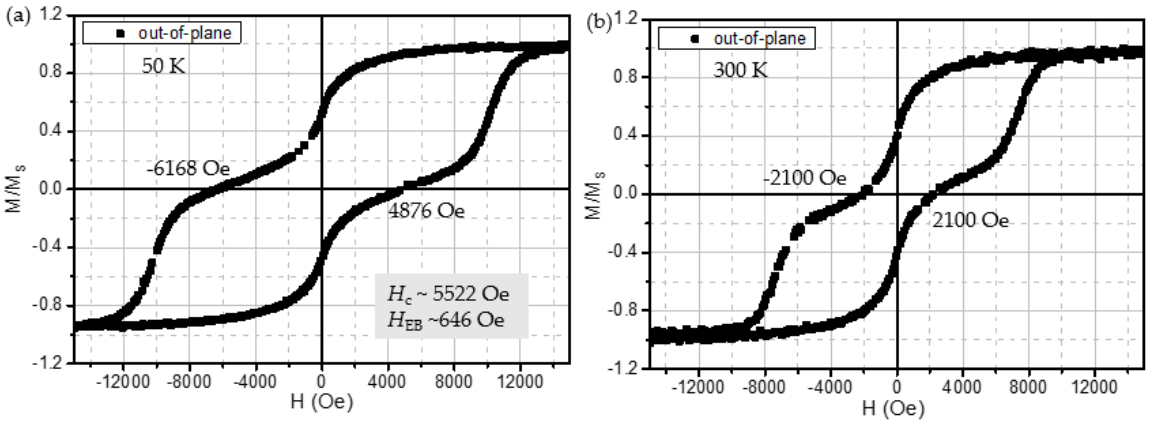

Figure 4-13 Magnetic hysteresis loops measured at 50 K (a) and 300 K (b) of field-cooled $BFO_{30nm}/Pt_{2nm}/CoPt_{10nm}$ films by SQUID.

4.4.2 $BiFeO_{3\ 30nm}/Pt_{1nm}/CoPt_{4nm}/MgO$ (001) films

In order to detect room temperature perpendicular exchange bias effect, CoPt layer thickness was reduced from 10 nm to 4 nm. Accordingly the interlayer Pt thickness was also reduced from 2 nm to 1 nm. This time, out-of-plane XRD profile is shown in Figure 4-

14. Similar to previous sample, (001)-textured BFO and CoPt bilayer forms. Because of the relatively thin CoPt, the ordering degree becomes smaller.

After field cooling, the hysteresis loops measured by SQUID at 50 K and 300 K are depicted in Figure 4-15. Similar to $BFO_{30nm}/Pt_{2nm}/CoPt_{10nm}$ sample, the loop shape exhibits a two-step magnetization. This unique shape will be discussed in next section. The most exciting result is the existence of room temperature perpendicular exchange bias effect. One can see from the loops, the coercivity and exchange bias value is 3547 Oe and 137 Oe, respectively at 50 K. And at 300 K, the two values become to 2806 Oe and 83 Oe. This is the first time to detect exchange bias phenomenon in perpendicular direction in BFO-based FM/AFM bilayers.

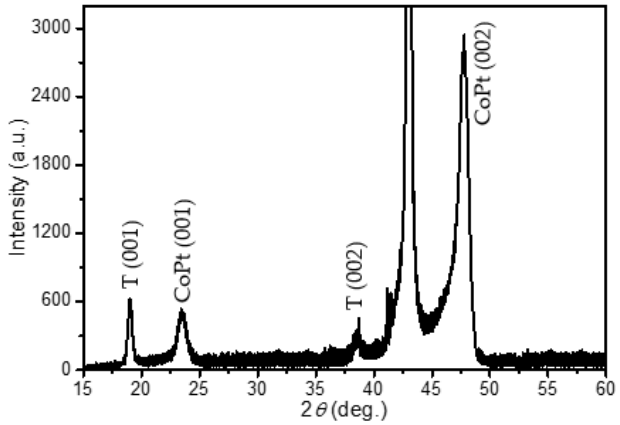

Figure 4-14 Out-of-plane XRD profile of $BFO_{30nm}/Pt_{1nm}/CoPt_{10nm}$ film

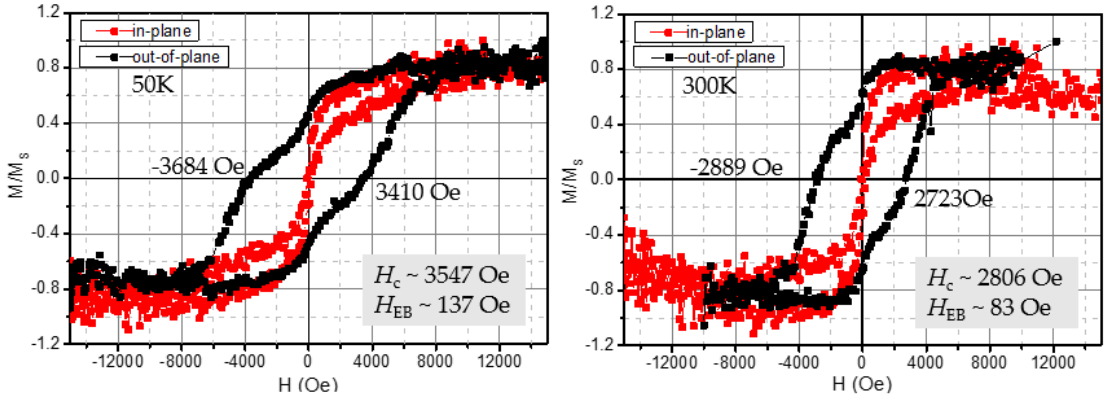

Figure 4-15 Magnetic hysteresis loops measured at 50 K (a) and 300 K (b) of field-cooled $BFO_{30nm}/Pt_{1nm}/CoPt_{4nm}$ by SQUID.

Auger electron spectroscopy (AES) depth profile was further conducted to confirm whether there is a Pt accumulation at the CoPt and BFO interface. The whole pattern and enlarged Co/Pt pattern are shown in Figure 4-16. Both Co and Pt show peak distribution across CoPt layer and there is no obvious Pt accumulation detected at the interface. Thus we believe Pt atoms are evenly distributed through the whole CoPt layer and the exchange bias effect indeed comes from interface coupling between CoPt and BFO layers.

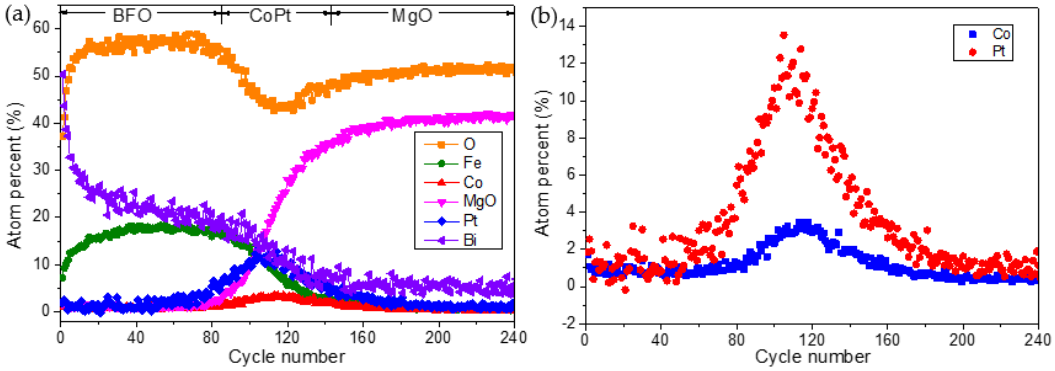

Figure 4-16 Auger electron spectroscopy depth profile of $BFO_{30nm}/Pt_{1nm}/CoPt_{4nm}$ sample. (a) is whole element pattern and (b) is Co/Pt atom pattern.

4.4.3 Summary and discussions

We have observed perpendicular exchange bias effect in two samples ($BFO_{30nm}/Pt_{1nm}/CoPt_{4nm}$ and $BFO_{30nm}/Pt_{2nm}/CoPt_{10nm}$). Since the magnitude of loop shift is far beyond the measurement resolution, we believe perpendicular exchange bias effect has been realized in this layered structure. However, to be honest, there exist a big issue with the reproducibility, which is a common problem for BFO film preparation. We have prepared around 20 samples under the similar growth conditions, but only these two samples exhibit exchange bias. Although few paper mentioned the BFO reproducibility, this is indeed a universal encountered problem, which many peopled discussed in the last year MMM conference (61st annual conference on magnetism and magnetic materials). This problem is irrelevant of the preparation method (magnetron sputtering or pulsed

laser deposition) and may hinder further application if not properly solved. I believe this may be one of the reasons that BFO-related publication numbers has decreased compared to that in 2012.[12]

4.5 Exchange coupling effect

In the last section, the measured MH loops not only shows perpendicular exchange bias, but also exhibits a two-step switching. In this section, we will discuss that this two-step switching behavior originates from exchange coupling effect. One thing need to point out is samples in section 4.4 and section 4.5 are actually fabricated under the similar growth condition. One difference is the Pt element growth rate. For samples in 4.4 section, Pt growth rate is relatively high ~ 1 nm/s, meaning deposition time is only 2 seconds for merely 2 nm due to the platinum intuitive high deposition rate. 2 seconds is tricky to control, and thus I think nominal 2 nm may differ from the real Pt thickness. On the contrary, in this section Pt thickness can be well controlled, since the target-substrate distance is increased. Meanwhile, 60 seconds are needed for 2 nm Pt thickness. For experimental details, please refer to section 2.1 and section 4.2.3. In all, Pt thickness is more accuracy in this section than that in section 4.4.

4.5.1 $BiFeO_{3\ 30nm}/Pt_{2nm}/CoPt_{10nm}$/MgO (001) films

Structure information are shown in Figure 4-17. As can been seen in out-of-plane XRD profile (Figure 4-17 (a)), all of the peaks can be attributed to (00*l*)-orientation BFO T phase and CoPt phase. Besides, the existence of superlattice (001) peak of CoPt means CoPt phase is ordered to $L1_0$ structure. The (001) epitaxial growth is also confirmed by TEM results. In Figure 4-17 (b), clearly layered structure can be seen. The red arrows indicate BFO layer thickness. Within BFO layer, there seems to exist separated layer around interface with CoPt and surface with difference grain size distribution. Although CoPt layer is a bit thick

to clear obverse (TEM image is too dark to detect plane arrangement and no diffraction spots in the diffraction pattern can be attributed to CoPt phase), BFO is epitaxial grow on CoPt indicated in (c) and (d) images.

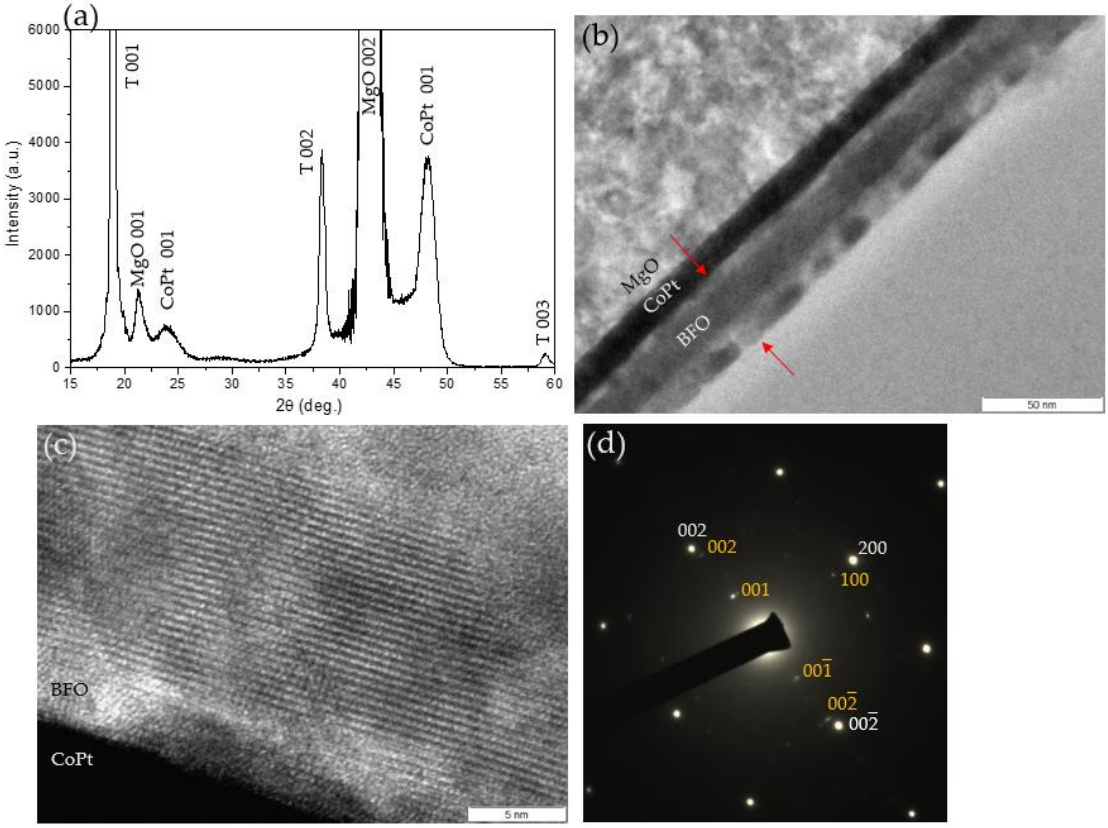

Figure 4-17 Structure information of $BFO_{30nm}/Pt_{2nm}/CoPt_{10nm}/MgO$. (a) Out-of-plane XRD profile. (b) and (c) are cross-section TEM image with different magnification factor. Two red arrows indicate BFO layer thickness. (d) is diffraction pattern containing MgO and BFO information. Yellow color indicates BFO while white color is MgO. CoPt layer is too thick to detect diffraction pattern.

Magnetic MH loops (after field cooling treatment) are depicted in Figure 4-18. At room temperature (Figure 4-18 (a)), the coercivity is only 4000 Oe and no loop shift can be detected. Further decrease measurement temperature to 50 K, the coercivity increases from 4000 Oe to 8000 Oe mainly due to the thermal excitation reduction. And there are still no exchange bias manifestation (clear hysteresis shift). We believe the absence of interface

effect between CoPt and BFO may lie in the Pt relatively large thickness, which hinders interaction.

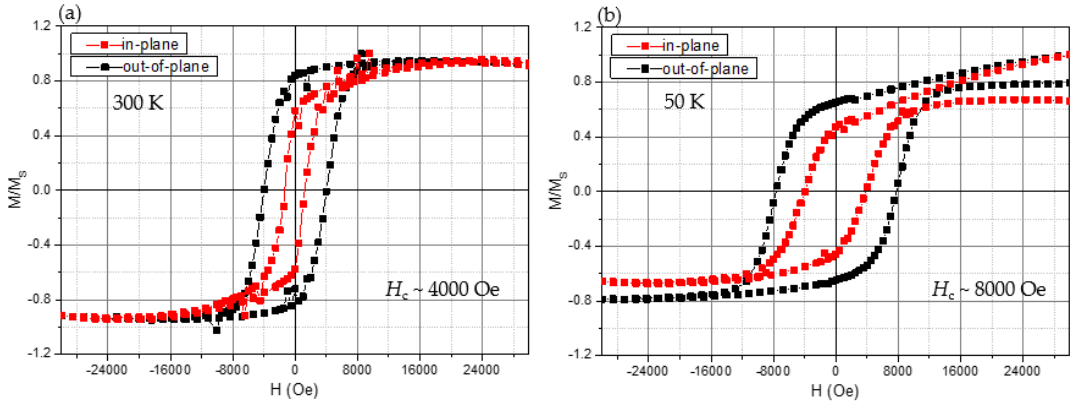

Figure 4-18 Magnetic hysteresis loops of field-cooled $BFO_{30nm}/Pt_{2nm}/CoPt_{10nm}$/MgO sample. Measurement temperature is 300 K (a) and 50 K (b), respectively.

4.5.2 $BiFeO_{3\ 30nm}/Pt_{2nm}/CoPt_{10nm}/a\text{-}SiO_2$ films

This sample is prepared at the same condition with the previous, and the only difference is amorphous SiO_2 substrates instead of MgO (001) single crystal substrates. According to our experiment results, BFO growth is quite sensitive to substrates and crystalized BFO phase cannot grow directly on a-SiO_2 substrates. In 2015, a paper reported that (111)-oriented CoPt layer can serve as buffer layer to grow (110)-textured BFO phase.[13] Enlighted by this paper, we replaced MgO by a-SiO_2 substrates. XRD profiles and MH curves are shown in Figure 4-19 and Figure 4-20, respectively.

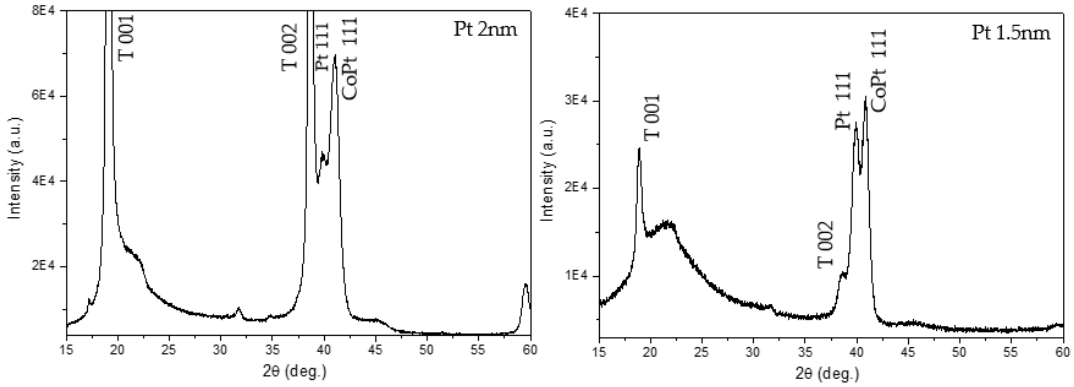

Figure 4-19 XRD profiles of $BFO_{30nm}/Pt_{2nm}/CoPt_{10nm}/a\text{-}SiO_2$ (a) and $BFO_{30nm}/Pt_{1.5nm}/CoPt_{10nm}/a\text{-}SiO_2$ (b)

Figure 4-19 presents XRD profiles of BFO/Pt/CoPt/a-SiO_2 samples with thickness of Pt around 2 nm and 1.5 nm, respectively. CoPt and Pt shows (111) orientation without MgO substrate. (The separation of CoPt and Pt peaks also indicates Pt is too thick to completely inter-diffuse into CoPt lattice. On a side-note, we need to decrease Pt thickness in order to obtain interface effect between CoPt and BFO.) Surprisingly, BFO can exhibit (001)-oriented T phase on (111)-textured CoPt, since they do not share similar lattice distance. However, this results go well with the reported paper.

The hysteresis loops of $BFO_{30nm}/P_{2nm}/CoPt_{10nm}$/a-$SiO_2$ are demonstrated in Figure 4-20 with measurement temperature ~ 300 and 50 K, respectively. In-plane and out-of-plane curves are almost isotropic and it is also an open loop at low temperature, which is the same with samples on MgO (001) substrates.

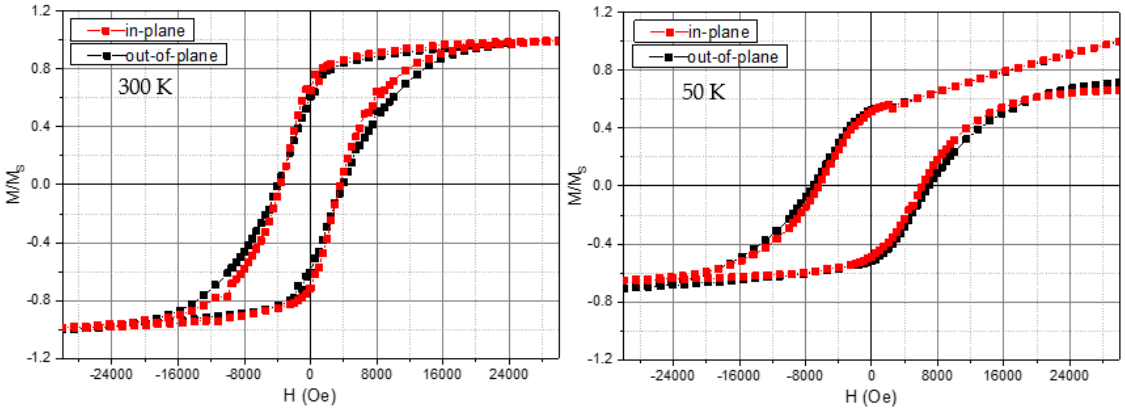

Figure 4-20 Magnetic hysteresis loops of field-cooled $BFO_{30nm}/Pt_{2nm}/CoPt_{10nm}$/a-$SiO_2$ sample. Measurement temperature is 300 K (a) and 50 K (b), respectively.

4.5.3 $BiFeO_{3\ 30nm}/Pt_{1.5nm}/CoPt_{10nm}$/MgO(001) films

The thickness of interlayer Pt is decreased by 0.5 nm. XRD profile and MH curves are shown in Figure 4-21 and 4-22, respectively. As shown in the Figure 4-21, the structure is almost the same with that of $BFO_{30nm}/Pt_{2nm}/CoPt_{10nm}$/MgO. Besides, Pt (002) peak separates from CoPt, indicating leftover of Pt atoms at the interface. Confirmed by magnetic

hysteresis loops, shown in Figure 4-22, there is still no interface effect. Thus Pt thickness should be reduced further.

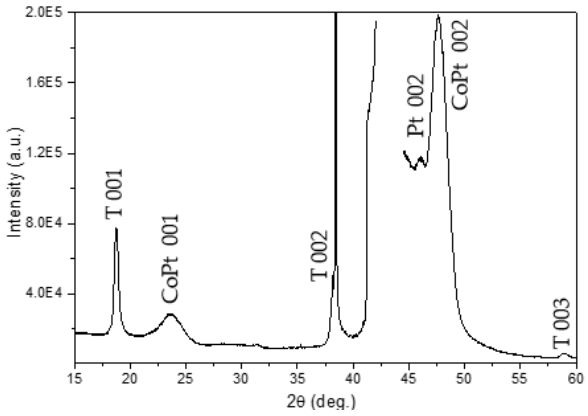

Figure 4-21 XRD profile of $BFO_{30nm}/Pt_{1.5nm}/CoPt_{10nm}$/MgO films.

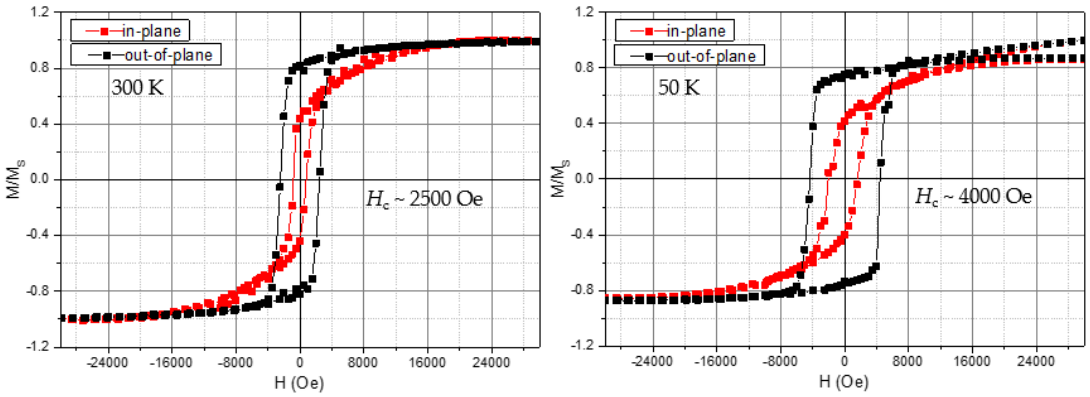

Figure 4-22 Magnetic hysteresis loops of field-cooled $BFO_{30nm}/Pt_{1.5nm}/CoPt_{10nm}/a\text{-}SiO_2$ sample. Measurement temperature is 300 K (a) and 50 K (b), respectively.

4.5.4 $BiFeO_{3\ 30nm}/Pt_{1nm}/CoPt_{10nm}$/MgO (001) films

Figure 4-23 and Figure 4-24 present the XRD profile and MH hysteresis loops measured at different conditions, respectively. From XRD, Both BFO and CoPt phases are still (001)-textured.

Besides, Pt (002) peak around 48 ° is not detected, indicating total inter-diffusion of Pt atoms. In order to further clarify the mechanism of open loops, magnetic hysteresis curves are measured as sequence shown in Figure 4-24.

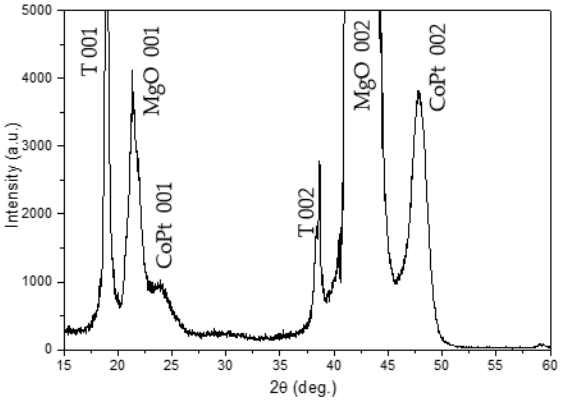

Figure 4-23 XRD profile of $BFO_{30nm}/Pt_{1nm}/CoPt_{10nm}$/MgO (001) films.

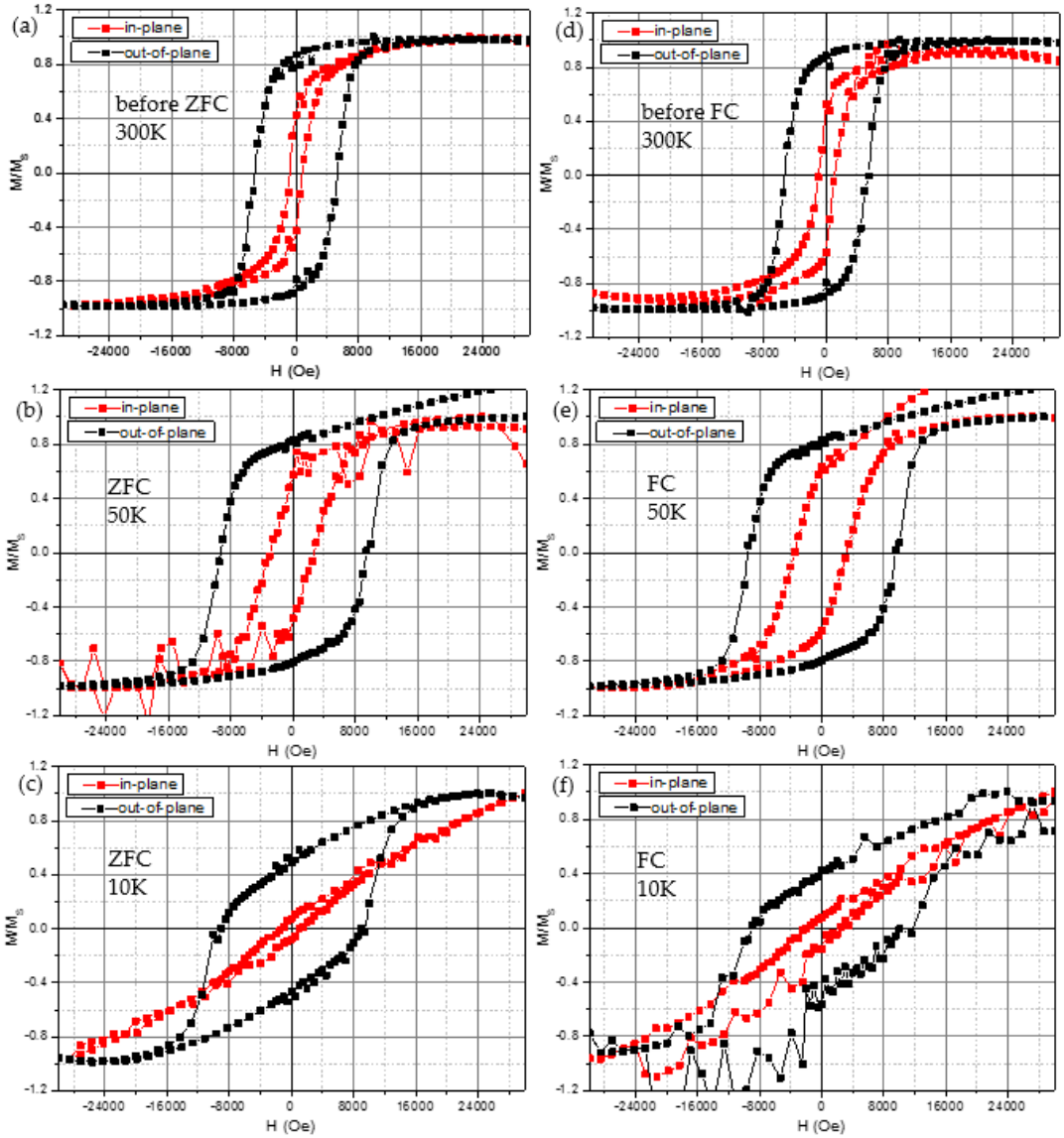

Figure 4-24 Magnetic hysteresis loops of field-cooled $BFO_{30nm}/Pt_{1.5nm}/CoPt_{10nm}/a\text{-}SiO_2$ samples. Measurement sequence is 300 K (a), zero field cooling to 50 K (b), zero field cooling to 10 K (c), raise to 300 K (d), field cooling to 50 K (e), field cooling to 10 K (f).

The MH curve is first measured at 300 K (Figure 4-24 (a)), then zero field cooling to 50 K (Figure 4-24 (b)), and continue zero field cooling to 10 K (Figure 4-24 (c)). After zero field cooling process, we raise the temperature to 300 K (Figure 4-24 (d)), 1 T field cooling to 50 K (Figure 4-24 (e)) and followed by 1 T field cooling to 10 K (Figure 4-24 (f)). As one can see from Figure 4-24, room temperature hysteresis loops is closed curve with the coercivity ~ 5300 Oe. However, measurement at 50 K all hysteresis loops are open curves regardless of zero-field cooling or field cooling process. This indicates the enhanced moment at upward field (or decreased moment at return field journey) is intrinsic property and has nothing to do with external field treatment. Interestingly, when further decrease measurement temperature to 10 K, the open curve return back to closed curve. However, the curve shape is different from previous. Such exotic phenomenon needs further exploration. We expect this comes from interface effect, since CoPt layer does not exhibit similar property.

4.5.5 $BiFeO_{3\ 30nm}/Pt_{0.5nm}/CoPt_{10nm}/MgO$ (001) films

When the Pt thickness is decreased to 1 nm, clearly no Pt accumulation at the interface and exotic enhanced moment phenomenon happens, which may result from interface effect. In this part, we continue to reduce the thickness of Pt to 0.5 nm. The structure information are shown in Figure 4-25.

As expected, Pt accumulation is not detected in XRD profiles (Figure 4-25 (a)) and both BFO and CoPt show (001)-epitaxial growth. Clear layered structure with strong contract can be seen in Figure 4-25 (b). Compare to that in Figure 4-17, this BFO layer is uniform and dense. In magnified image (Figure 4-25 (c)), BFO epitaxial lattice starting from the interface can be observed. Although CoPt layer is a bit thick to detect the lattice growth information, the diffraction pattern (Figure 4-25 (d)) reveals the epitaxial growth. In

summary, both BFO and CoPt exhibit (001) epitaxial growth in MgO (001) substrates. Besides, clear interface contract indicates there is no Pt accumulation at the interface.

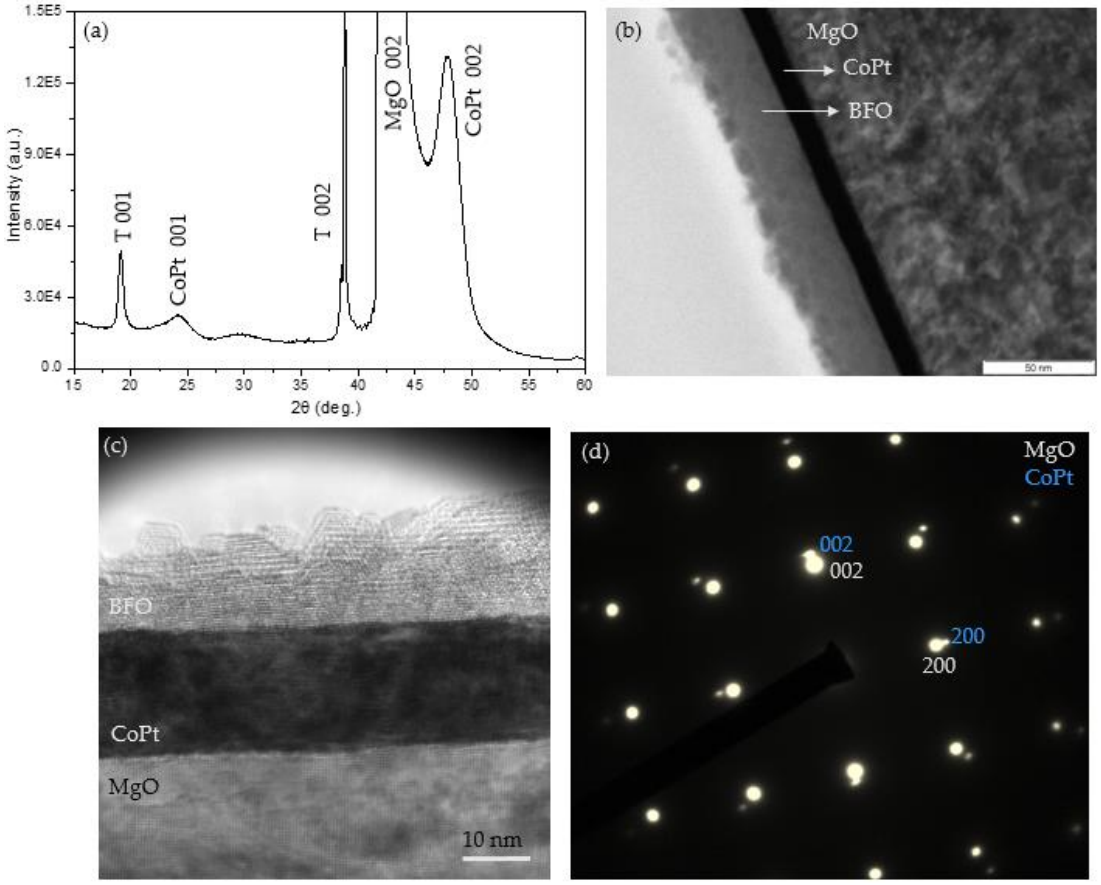

Figure 4-25 Structure information of $BFO_{30nm}/Pt_{0.5nm}/CoPt_{10nm}$/MgO samples. (a) XRD profile, (b) and (c) are Cross-section transmission electron microscopy images, (d) diffraction pattern.

As we measure the perpendicular MH curves at room temperature, a new phenomenon is observed. That is there exist two separate magnetic states and these two states can be manipulated by external magnetic field. Detail is drawn in Figure 4-26.

As demonstrated in Figure 4-26, each loop is recorded after applying static in-plane or out-of-plane magnetic field (5000 Oe) as noted. Clearly, there are two disparate magnetic states. One state (Figure 4-26 (a) and (c)) exhibits two-step magnetization process, a distinctive behavior of a decoupled system.[14] The saturation moment M_s is 580 emu/cc and

coercivity H_c is around 4500 Oe. Figure 4-26 (b) and (c) depict typical exchange-coupled loops[15,16], where uniform magnetization switching is observed. Guided by blue dashed lines, one can see that loops in Figure 4-26 (b) and (d) have a smaller M_s (~ 480 emu/cc) compared to that of loops in Figure 4-26 (a) and (c). The two magnetic states can be repeatedly switched by static field. That is the typical exchange coupling loop behavior is induced by in-plane direction magnetic field and vanished upon out-pf-plane field.

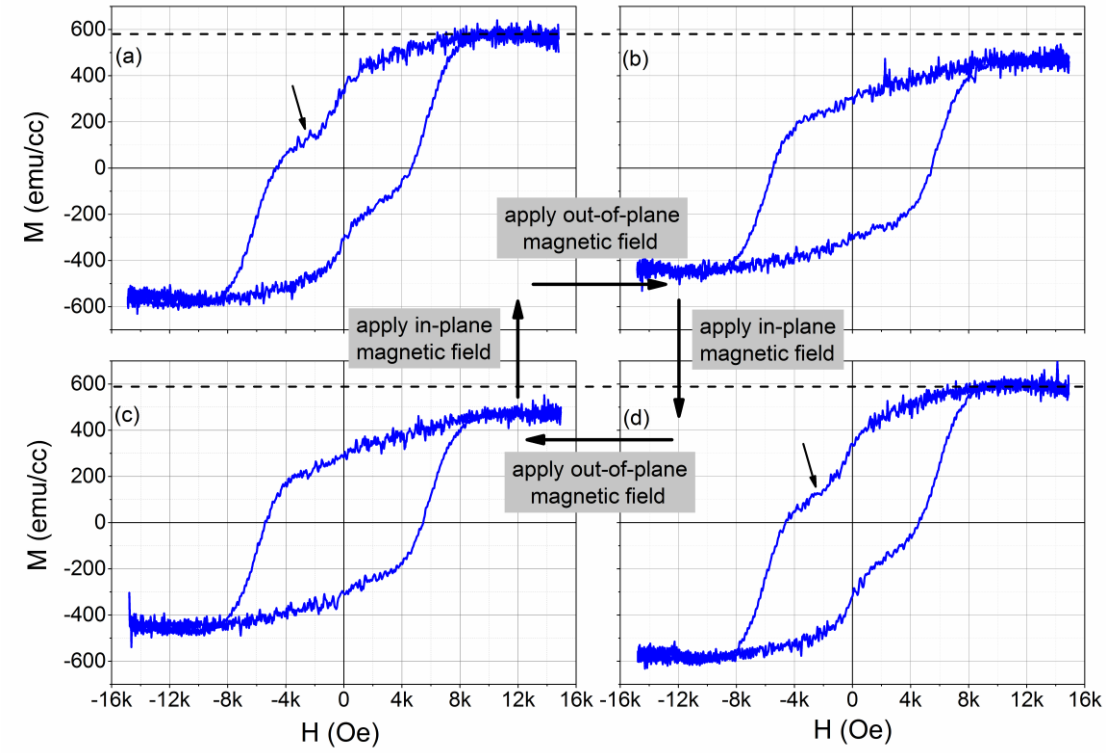

Figure 4-26 Perpendicular magnetic hysteresis loops of $BFO_{30nm}/Pt_{0.5nm}/CoPt_{10nm}$ sample measured at room temperature. (a) and (c) are recorded after applying 5000 Oe in-plane external magnetic field. (b) and (d) are recorded after applying 5000 Oe out-of-plane external magnetic field.

To clearly determine the composition of each layer, element mapping is conducted, as illustrated in Figure 4-27. From Figure 4-27, element distribution is clear seen. In Co mapping image, there is a Co-deficient layer near the interface at CoPt side. Besides, Co atoms also exist near the interface at BFO side, suggesting Co-containing BFO layer formed

due to Co diffusion. In all, the film structure (from substrate to top direction) can be expressed as following: CoPt $L1_0$ layer (6.5nm)/ CoPt Co-deficient layer (1.5 nm)/ Co-containing BFO layer (2 nm)/ BFO layer. The film thickness is estimated according to Co mapping image.

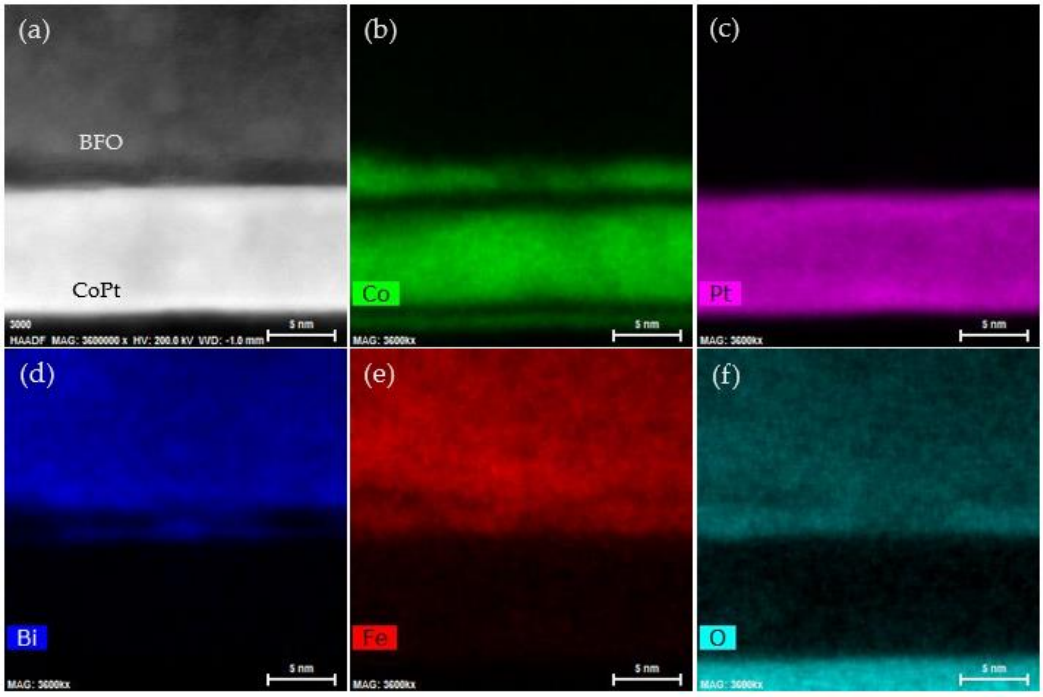

Figure 4-27 (a) High angle annular dark-field (a) image of BFO/CoPt interface. Energy dispersive spectroscopy (EDS) elementary mapping of BFO/CoPt interface. (b), (c), (d), (e) and (f) correspond to Co, Pt, Bi, Fe and O, respectively.

Based on the above layered structure, we establish a model to illustrate the field-mediated exchange coupling phenomenon, as demonstrated in Figure 4-28. The $L1_0$ ordered CoPt (ordered CoPt) has a high perpendicular anisotropy (K ~ $4*10^7$ erg/cm^3)[17] and most moments remain in perpendicular direction even after the in-plane field applied. On the contrary, Co-deficient CoPt is prone to respond to external field as this CoPt layer is not ordered structure due to the composition deviation. We denote this layer as non-ordered CoPt in the following paragraph. The Co-containing BFO is believed to display ferromagnetic property[18],[19], although non-doped BFO is antiferromagnet.

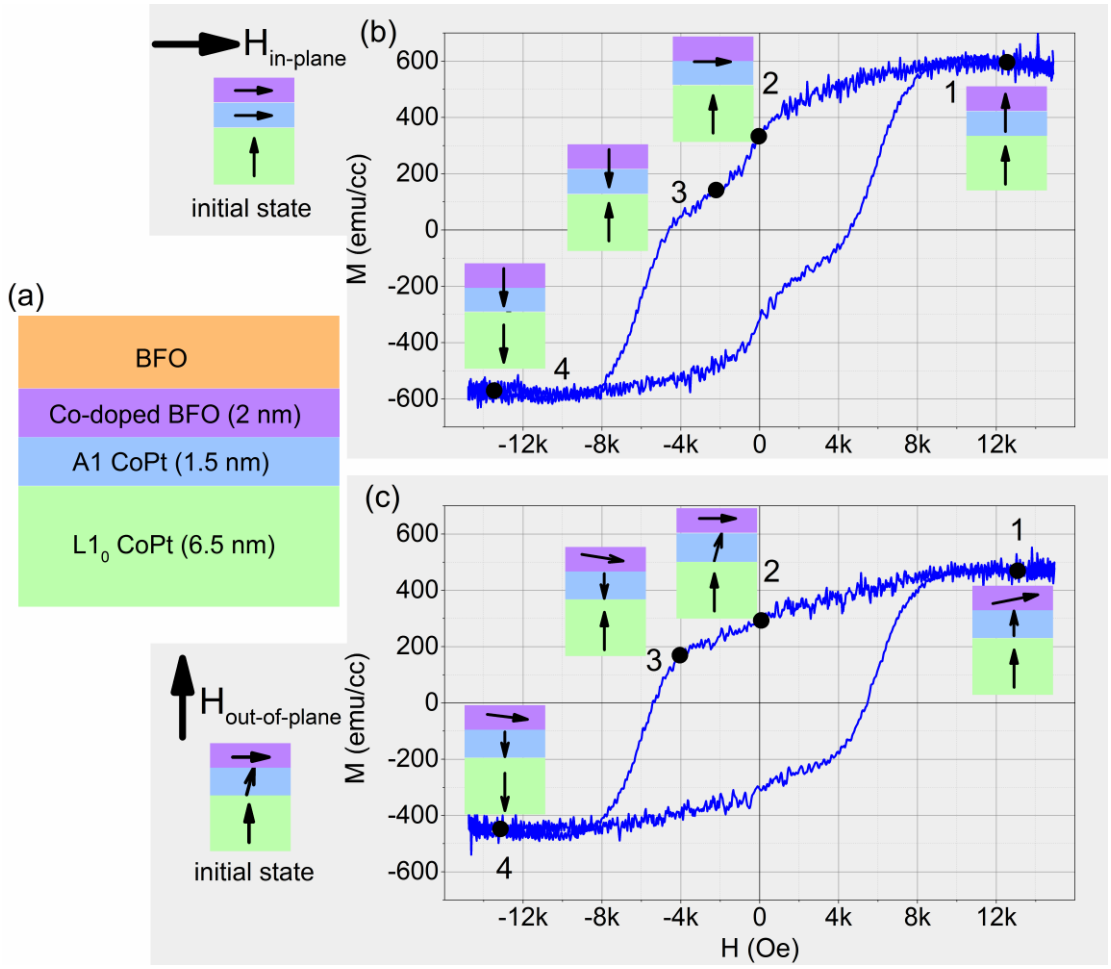

Figure 4-28 (a) is layered structure illustration. Schematic diagram of moment configuration at each step in in-plane magnetic field case (b) and out-pf-plane magnetic field case (c), respectively.

Applying an in-plane magnetic field (5000 Oe), the moments in both non-ordered CoPt layer and Co-containing BFO layer lie in longitudinal direction. This makes the two layers coupled together and can be treated as a whole. On the contrary, most moments of the order CoPt layer (hard magnet) still lie in perpendicular direction once removing the in-plane magnetic field. Thus the perpendicular moments and the longitudinal moments are actually in a decoupled state. When measuring perpendicular hysteresis loop, the coupled longitudinal moments in non-order CoPt and Co-containing BFO can also respond to the perpendicular field and align to perpendicular direction, as shown in Figure

4-28 (b) 1 stage. Therefore the M_s value contains information from three parts: ordered CoPt, non-ordered CoPt and Co-containing BFO. When decreasing the applied field, the moments of the coupled non-ordered CoPt and Co-containing BFO layers tend to rotate back in the longitudinal direction, as drawn in Figure 4-28 (b) 2 stage. Because of the above-mentioned decoupling, there shows two-step switching. The moments of the non-ordered CoPt and Co-doped BFO are gradually rotated upon the opposite field (~ 1500 Oe) and then comes a plateau shape in the hysteresis loop (shown in Figure 4-28 (b) 3 stage). After the applied field becomes large enough, the ordered CoPt is reversed (shown in Figure 4-28 (b) 4 stage). When applying static out-of-plane field, the moments of non-ordered CoPt layer align itself mainly in perpendicular direction and tend to couple with the ordered CoPt layer. The moments of Co-doped BFO mainly lie in longitudinal direction, probably due to a large anisotropy, and thus decouple with the non-ordered CoPt layer. As measuring hysteresis loop, the M_s value is smaller compared to that of in-plane magnetic field case (shown in Figure 4-28 (c) 1 stage), since a part of moments from Co-containing BFO is not included. Owing to the exchange coupling between ordered and non-ordered CoPt, the loop displays uniform switching instead of two-step switching. In summary, the external magnetic field controls the moment direction in ordered, non-ordered CoPt and Co-containing BFO layers. In in-plane field case, non-ordered CoPt couples with Co-doped BFO, leading to two-step switching loops. In out-of-plane case, non-ordered CoPt couples with ordered CoPt, which shows only one-step switching loops.

Since this phenomenon is new to us, we prepare other samples in the same condition and try to repeat what we have observed. Such repetition can eliminate the possibility from external influence and confirm the intrinsic property of BFO/CoPt bilayer structures. Figure 4-29 depicts the repeated results. The same with previous that clearly two different magnetic states can be controlled by magnetic field. Although M_s and H_c values are a bit

different from the previous measured, the tendency is the same. We believe the slightly difference may be related to the Co (or Pt) atoms diffusion level.

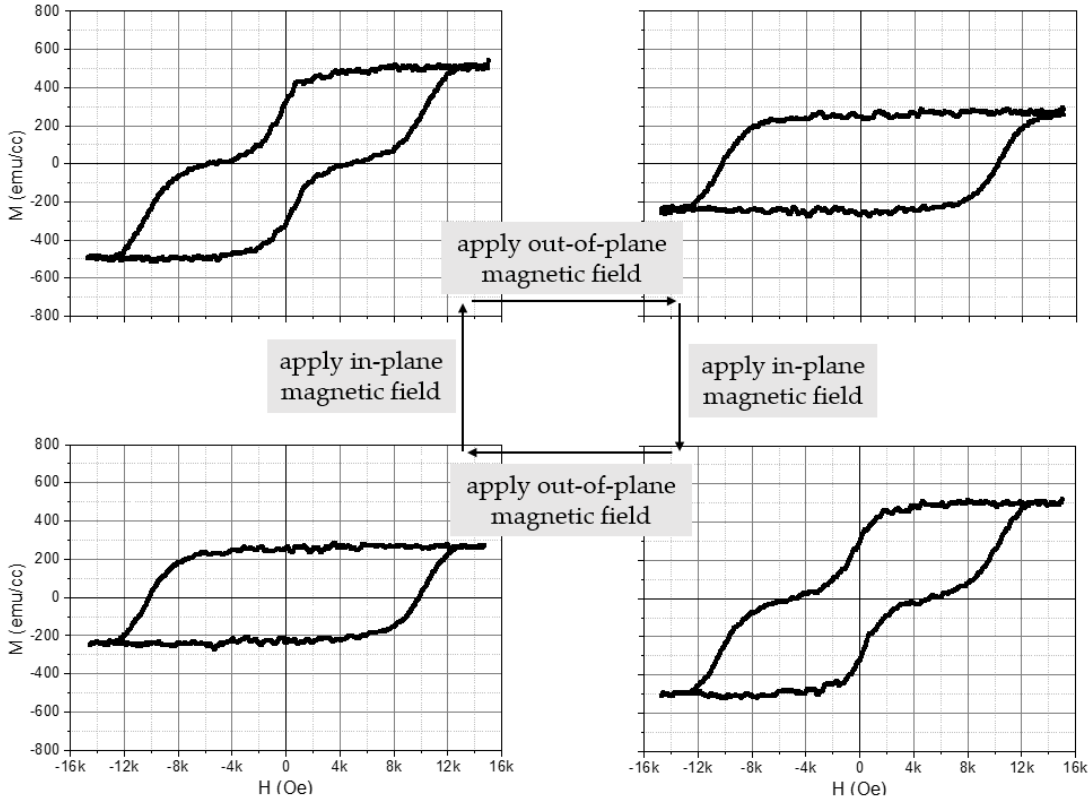

Figure 4-29 Perpendicular magnetic hysteresis loops measured at room temperature after orthogonal external field treatment. All of the experiment conditions including film preparation and measurement sequences are the same with that in Figure 4-25.

Afterwards we decide to check whether perpendicular exchange bias effect exists or not, which is the original purpose of this experiment. Based on the above field-mediated results, we plan to try both in-plane and out-of-plane field cooling and measure perpendicular hysteresis loops. Figure 4-30 shows magnetic hysteresis loops after in-plane 380 °C field-cooling treatment. Although there are some noise, we can still defer that no exchange bias effect can be seen (indicated by neither clear H_c enlargement nor loop shift). The same situation occurs for out-of-plane field cooled sample, as shown in Figure 4-31. We believe absence of the exchange bias effect can be understood by the existence of Co-

containing BFO layer, which separate CoPt and BFO interaction. Another reason may due to the interface coupling during BFO deposition, as we discussed in section 4.3.3.

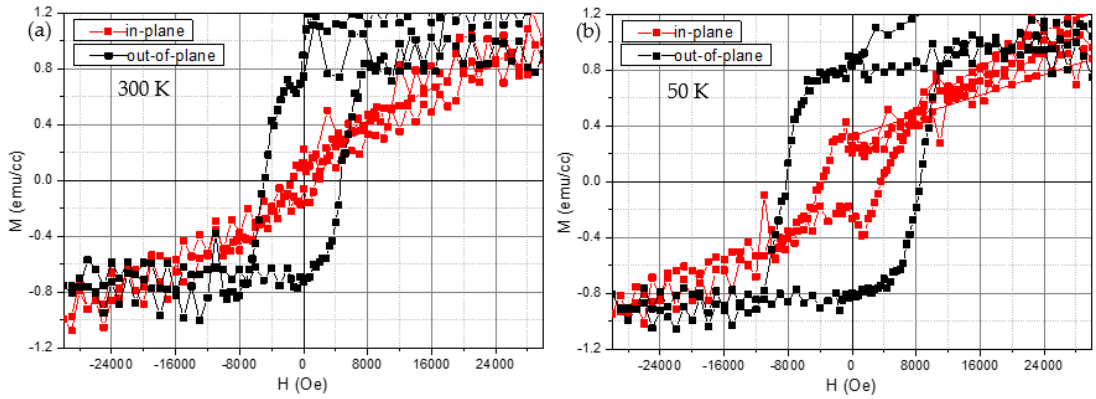

Figure 4-30 Magnetic hysteresis loops of field-cooled $BFO_{30nm}/Pt_{0.5nm}/CoPt_{10nm}$/MgO (001) sample after in-plane field cooling process from 380 °C. Measurement temperature is 300 K (a) and 50 K (b), respectively.

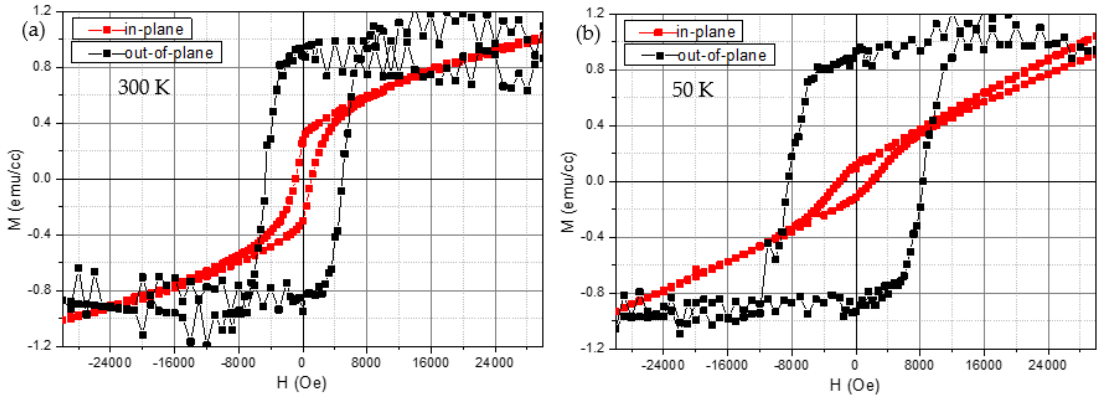

Figure 4-31 Magnetic hysteresis loops of field-cooled $BFO_{30nm}/Pt_{0.5nm}/CoPt_{10nm}$/MgO (001) sample after out-of-plane field cooling process from 380 °C. Measurement temperature is 300 K (a) and 50 K (b), respectively.

4.6 Summary

In this chapter, we have prepared $BFO_{30nm}/Pt_{0.5\text{-}2nm}/CoPt_{10nm}$/MgO (001) layered samples. CoPt film are first deposited at low temperature (300 – 400 °C) and followed by

high temperature (700 – 750 °C) annealing for 3 hours to get ordered $L1_0$ phase. Thus all the magnetic properties are achieved in perpendicular direction.

Perpendicular anisotropy enhancement has been observed with existence of BFO layers compared to that single ordered CoPt layers.

Perpendicular exchange bias effect has been detected in two layered samples: $BFO_{30nm}/Pt_{2nm}/CoPt_{10nm}$ and $BFO_{30nm}/Pt_{1nm}/CoPt_{4nm}$. The exchange bias value is as large as ~ 646 Oe measured at 80 K.

Besides, (001)-epitaxial $BFO_{30nm}/Pt_{0.5nm}/CoPt_{10nm}$ layers are also fabricated. An external magnetic field-mediated exchange coupling phenomenon was observed in this layered structures. Element mapping results suggest there exist two additional layers across the interface: Co-deficient CoPt (~ 1.5 nm) and Co-containing BFO layer (2 nm). This exact discrepant Co-distribution leads to exchange coupled and decoupled states, which can be induced by orthogonal external fields. However, no perpendicular exchange bias effect can be observed in this layered samples, probably due to the existence of addition two layers (total thickness ~ 3.5 nm) between CoPt and BFO interface.

Refenrence

[1] A. Hirohata,. H. Sukegawa, H. Yanagihara, I. Zutic, T. Seki, S. Mizukami and R. Swaminathan, *IEEE Trans. Magn.* **51**, 10 (2015)

[2] M. Ohtake, D. Suzuki, F. Kirino and M. Futamoto, *IEICE Trans. Electron.*, **E96-C**, 12 (2013)

[3] B. D. Cullity, *Elements of X-Ray Diffraction*. Addison-Wesley, pp. 104-137, 1956

[4] H. Okamoto, *Binary Alloy Phase Diagrams*, II Ed., Ed. T. B. Massalski, pp. 1225-1226, 1990

[5] Y. K. Takahashi, T. Ohkubo, M. Ohnuma and K. Hono, *J. Appl. Phys.* **93**, 7166 (2003)

[6] F. Kurth, M. Weisheit, K. Leistner, T. Gemming, B. Holzapfel, L. Schultz and S. Faehler, *Phys. Rev. B* 82, 184404 (2010)

[7] T. Klemmer, D. Hoydick, H. Okumura, B. Zhang and W. A. *Soffa, Scr. Metall. Mater.* **33**(10-11), 1793 (1995)

[8] H. Zeng, M. L. Yan, N. Powers and D. J. Sellmyer, *Appl. Phys. Lett.* **80,** 2350 (2002)

[9] D. E. Laughlin, K. Srinivasan, M. Tanase and L. Wang, *Scr. Mater.* **53**, 383 (2005)

[10] Y. Yu, J. Shi and Y. Nakamura, *J. Appl. Phys.* **108**, 023912 (2010)

[11] J. Dho and M. G. Blamire, *J. Appl. Phys.* **106**, 073914 (2009)

[12] D. Sando, B. Xu, L. Bellaiche and V. Nagarajan, *Appl. Phys. Rev.* **3**, 011106 (2016)

[13] H. W. Chang, F. T. Yuan, Y. C. Yu, S. Y. Tu, P. C. Lin, C. R. Wang, A. B. Yang, C. S. Tu and S. U. Jen, J. Appl. Phys. **117**, 17C721 (2015)

[14] J. P, Wang, W. K. Shen and J. M. Bai, IEEE TRANSACTION ON MAGNETICS, **41**, 10 (2005)

[15] J. P. Wang, W. K. Shen, J. M. Bai, R. H. Victora, J. H. Judy and J. L. Song, *Appl. Phys. Lett.* **86**, 142504 (2005)

[16] G. Asti, M. Ghidini, R. Pellicelli, C. Pernerchele and M. Slozi, *Phys. Rev. B* **73**, 094406 (2006)

[17] A. Tsoukatos, H. Wan, G. C. Hadjipanayis, Y. J. Zhang and M. Waite, *J. Magn. Magn. Mater.* **118**, 387 (1993)

[18] H. Naganuma, J. Minura and S. Okamura, *Appl. Phys. Lett.* **93**, 052901 (2008)

[19] V. R. Singh, V. K. Verma, K. Ishigami, G. Shibata, Y. Yamazaki, A. Fujimori, Y. Takeda, T. Okane, Y. Saitoh, H. Yamagami, Y. Nakamura, M. Azuma and Y. Shimakawa, *J. Appl. Phys.* **114**, 103905 (2013)

Chapter 5 Longitudinal exchange bias effect in $Co_2FeSi/BiFeO_3$ layered structures

5.1 Heusler compounds

5.1.1 Brief introduction about Heusler compounds

In 1903, professer Fritz Heusler discovered that compound Cu_2MnAl consisting of non-magnetic elements turned out to be ferromagnetic.[1] This attracted lots of interest from magnetic community and now such ternary intermetallic are known as Heusler compounds. Up till now Heusler compounds have ~ 1500 members with various element combinations and tunable properties.[2] There are two families of Heusler: one is XYZ formula with 1:1:1 composition (also known as half Heusler); the one is X_2YZ chemical formula with 2:1:1 stoichiometry (known as full Heusler). Both families are crystalized in cubic structures with lattice parameter ranging from ~ 5.6 Å to 7.2 Å. In general, X and Y are transition metals and Z comes from main group. Detail element combinations are summarized in Figure 5-1, with X, Y, Z place indicated by different colors.

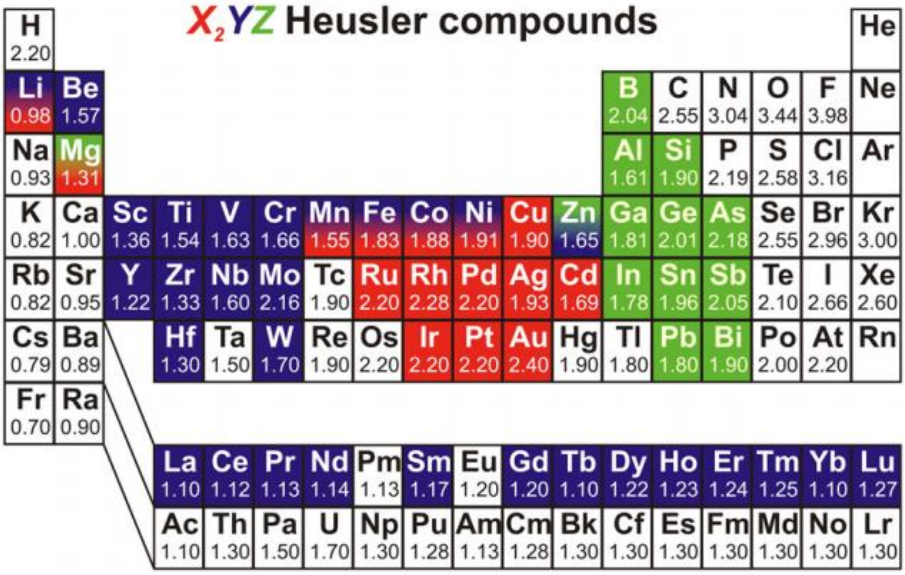

Figure 5-1. Element combination of Heusler compounds.[2]

The properties of Heulser compounds can also be manipulated via such diversity element combinations. What is unexpected is that the properties can simply be predicted by counting valence electron number per formula unit.[3] For example, Heusler compounds with 27 valence electrons are superconductors (palladium-based Heusler).[4,5] 17 or 19 valence electrons Heusler compounds are ferromagnetic (such as Ni2MnAl).[6] 8 or 18 valence electrons Heusler compounds are semiconductor (such as LiMgN, YNiAs).[7] Detail information is summarized in Figure 5-2.

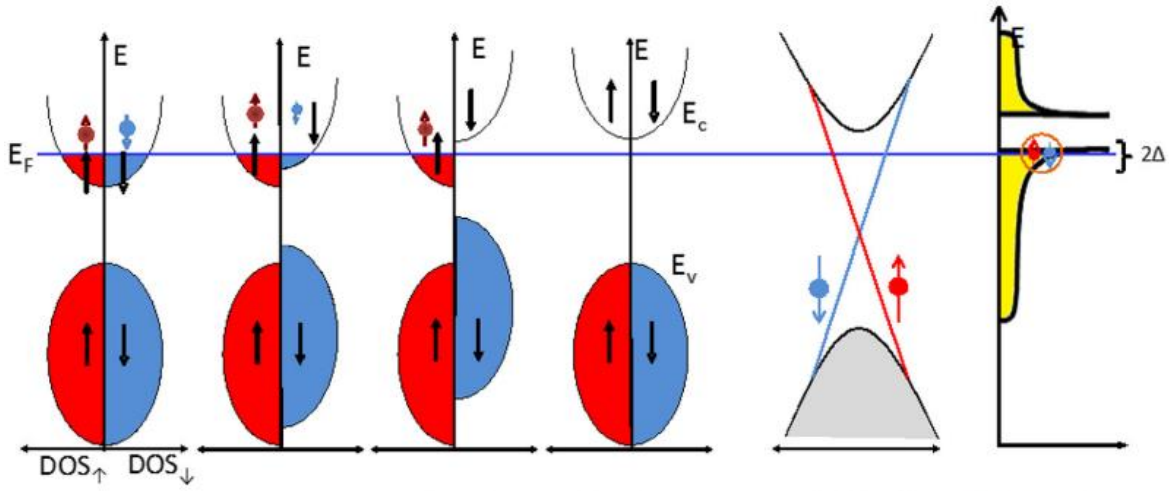

Figure 5-2 Different electronic properties of Heusler compounds depending on the number of valence electrons per formula unit.[8]

This suggests the possibility to tune properties of Heusler compounds via various element combinations so as to vary the valence electron numbers.

One of the most interesting topic about Heulser compounds is spintronic field. This is ferromagnetic and half metal Heusler compounds. As demonstrated in band gas structure in Figure 5-2, one spin band is semiconducting and the other direction spin band is metallic in half metal. Thus the free carrier spin polarization will be 100 % at the Fermi level. This unique property makes half meal an ideal candidate for spintronic application. Among all

kinds of Heusler compounds, Co-based Heusler compounds are widely explored and used due to its high Curie temperature (1120 K) and large saturation moment value (~ 6 μ_B/f.u. or ~ 1200 emu/cc).

5.1.2 Typical structures of Heusler compounds

As we all know, the property is closely related to the structures (atom order and distribution). This section will discuss the typical crystal structure of both half and full Heusler compounds. Ordered Heusler compounds can be derived from combination of NaCl-type structure and ZnS-type structure, as drawn in Figure 5-3.

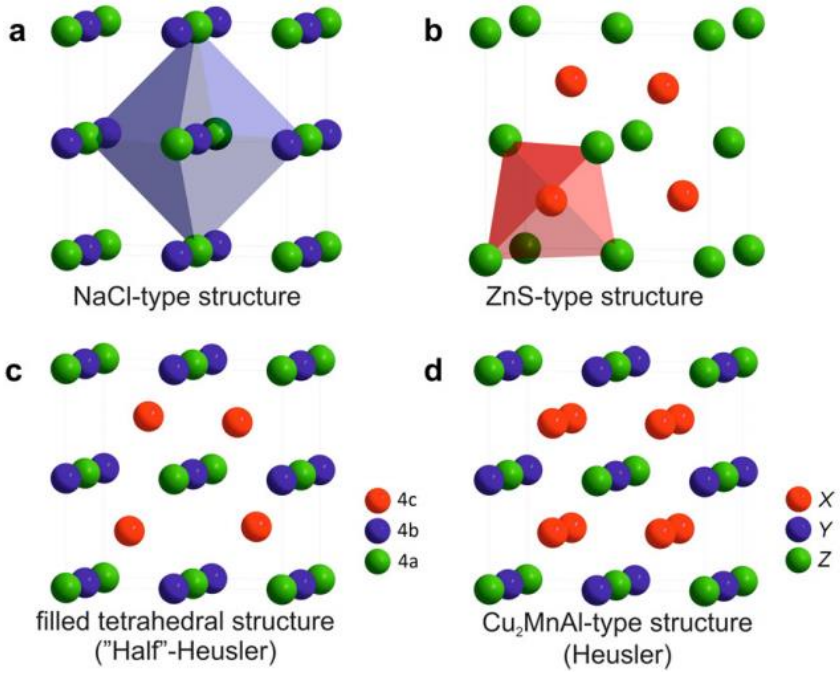

Figure 5-3 (a) Rock salt structure, (b) zinc blende structure, (c) half Heusler structure (CaF_2-type) and (d) full Heusler structure (Cu_2MnAl-type).[2]

There are three Wyckoff positions in half Heusler structures: 4a (0, 0, 0), 4b (1/2, 1/2, 1/2) and 4c (1/4, 1/4, 1/4) sites (Figure 5-3 (c)). This structure can treated as octahedral sites (4b) occupied ZnS-lattice. Besides, atoms on 4a and 4b sites together also compose NaCl-type structure. The two ground structures (ZnS-type and NaCl-type) emphasize on different bonding interactions. ZnS-type presents covalent bonding while NaCl-type has

an ionic character. Thus how does the X, Y, Z three elements occupy the three sites depends on the atom size and their relative electronegativity as well.[9,10] Similarly, full Heusler also has three Wyckoff positions: 8c (1/4, 1/4, 1/4), 4a and 4b. However there is only on possible atom arrangement in full Heusler, that is X atoms on 8c, Y and Z on 4a and 4b, respectively. Full Heusler can be viewed as NaCl-type structure where all tetrahedral are filled by X atoms (8c). On the other hand, it can also be understood as ZnS-type structure consisting of one X and Z with the other X on tetrahedral sites and Y at octahedral sites. Some literature also view full Heusler as CsCl-like superstructure.[11] This makes sense if i) Y and Z atoms are disordered and ii) unit cell is shifted by (1/4, 1/4, 1/4) from original point. In such case, X atoms locate at 8 edge points of unit cell and Y or Z fills at the center of the cubic, forming CsCl-type structure.

5.1.3 Co_2FeSi brief introductions

Co_2FeSi (CFS) is a half-metallic Heusler compound with the highest magnetic moment of 5.97 μ_B (5 K) and the highest Curie temperature of 1100 K.[12,13] This makes Co_2FeSi a good candidate material in tunneling magnetoresistance (TMR) devices. The TMR value of CFS and AlO_x barrier can reach 67.5 % at 5 K and 43.6 % at 298 K.[14] Further adjusting the Fermi level by doping, the TMR value ($Co_2FeAl_{0.5}Si_{0.5}$ electrode and MgO barrier) can increase to 175 % at room temperature.[15] Now this TMR value reaches to 386 % at 300 K and 832 % at 9 K.[16] In this section we mainly focus on Co_2FeSi brief review.

Many methods have been used to calculate the magnetic performance of Co_2FeSi. At first, first principle calculation with linearized muffin tin orbital (LMTO) method predicts Co_2FeSi is a ferromagnet and magnetic moment is ~ 5.08 μ_B per formula unit using the lattice parameter a = 5.64 Å.[17] However as we know this calculated value is smaller than experiment value 6 μ_B. Further more detail calculations are used to refine the simulation

results, such as muffin tin and the atomic sphere approximations allowance and coherent potential approximation. The calculated total magnetic moments ranges from 4.9 μ_B to 5.7 μ_B, which is still small compared to experiment value. Then a structural refinement is performed to minimize the total energy, and this time researchers find that experimentally obtained moment value occurs only at larger lattice parameter. Besides, from band structure the Fermi level lies inside the band gap if the lattice parameter expands 2.4 – 4 %.[18,19] Using local density approximation (LDA) + the Hubbard U scheme provided by Wien2K package[20], band structure and density of states (DOS) of Co_2FeSi are depicted, as shown in Figure 5-4.

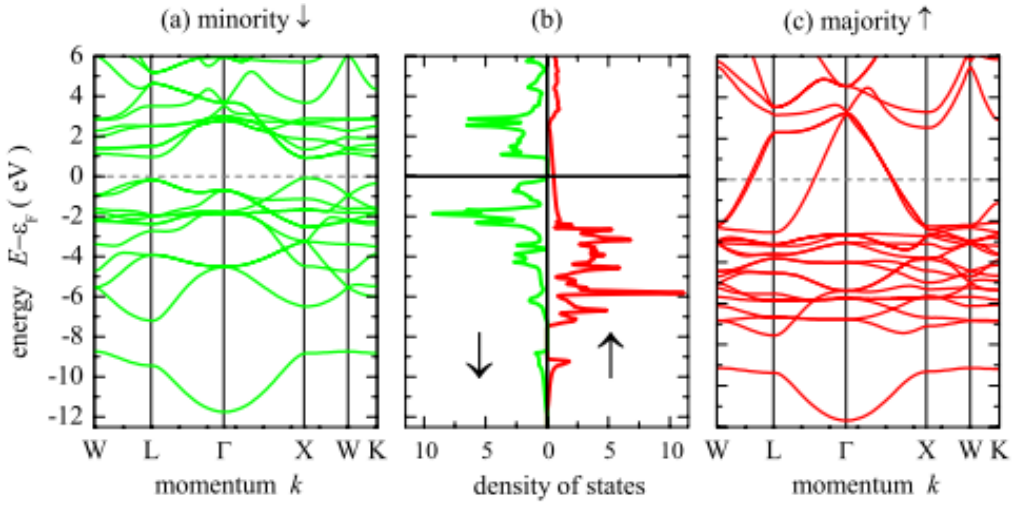

Figure 5-4 Band structure and DOS of Co_2FeSi.[11]

Obviously, Fermi level lies in minority gap region, suggesting the half-metallic character. For majority spin, a small value of DOS around Fermi level. This is mainly derived from states located at Co and Si sites.[11] One thing needs to be pointed out is that all of the above mentioned simulation results is based on $L2_1$ ordered Co_2FeSi structure with a lattice parameter of 5.64 Å. In other words, the half-metallicity of CFS (full-Heusler alloys) depends on its atomic ordered crystal structure. Speaking of the structure, now we need to specify each structure character. Figure 5-5, 5-6, 5-7 describe $L2_1$ structure, DO_3

structure and B_2 structure, respectively. For $L2_1$ and DO_3 structure, one unit cell is drawn. While for B2, four unit cells (2*2) are drawn for easy comparison.

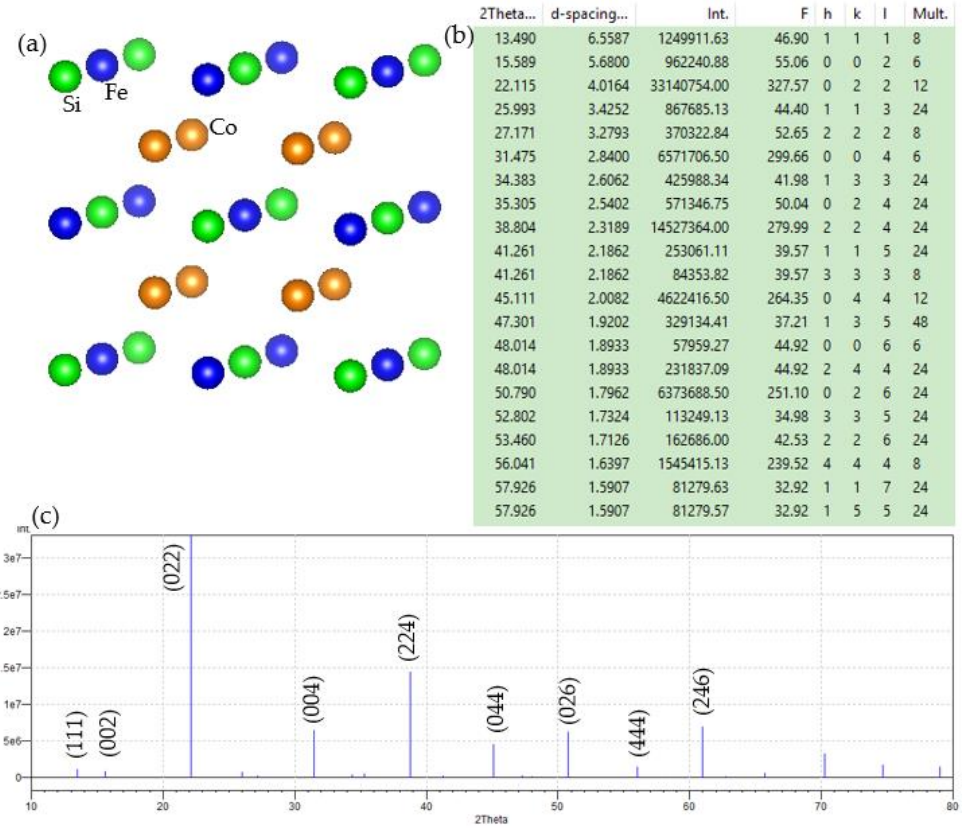

2Theta...	d-spacing...	Int.	F	h	k	l	Mult.
13.490	6.5587	1249911.63	46.90	1	1	1	8
15.589	5.6800	962240.88	55.06	0	0	2	6
22.115	4.0164	33140754.00	327.57	0	2	2	12
25.993	3.4252	867685.13	44.40	1	1	3	24
27.171	3.2793	370322.84	52.65	2	2	2	8
31.475	2.8400	6571706.50	299.66	0	0	4	6
34.383	2.6062	425988.34	41.98	1	3	3	24
35.305	2.5402	571346.75	50.04	0	2	4	24
38.804	2.3189	14527364.00	279.99	2	2	4	24
41.261	2.1862	253061.11	39.57	1	1	5	24
41.261	2.1862	84353.82	39.57	3	3	3	8
45.111	2.0082	4622416.50	264.35	0	4	4	12
47.301	1.9202	329134.41	37.21	1	3	5	48
48.014	1.8933	57959.27	44.92	0	0	6	6
48.014	1.8933	231837.09	44.92	2	4	4	24
50.790	1.7962	6373688.50	251.10	0	2	6	24
52.802	1.7324	113249.13	34.98	3	3	5	24
53.460	1.7126	162686.00	42.53	2	2	6	24
56.041	1.6397	1545415.13	239.52	4	4	4	8
57.926	1.5907	81279.63	32.92	1	1	7	24
57.926	1.5907	81279.57	32.92	1	5	5	24

Figure 5-5 $L2_1$ structure (Cu_2MnAl-prototype) of Co_2FeSi. (a) Schematic unit cell; (b) Calculated diffraction peak information; (c) Calculated diffraction pattern.

From application aspect, $L2_1$ structure is the most desired. Generally speaking, DO_3 type disorder (random atom arrangement between Co and Fe) can be detected by the Rietveld refinement of XRD pattern.[21] However the random atom arrangement between Fe and Si (B2 disorder) is a bit difficult to distinguish by Rietveld refinement of XRD or even neutron scattering. This is mainly due to the low intensity of (111) and (002) diffraction peaks.[22] To further detect the site specific information, extended X-ray absorption fine structure (EXAFS) measurements can be used.[22] Since this method is not daily accessible and B2 disorder does not make big difference for properties, we do not distinguish B2 and $L2_1$ structures.

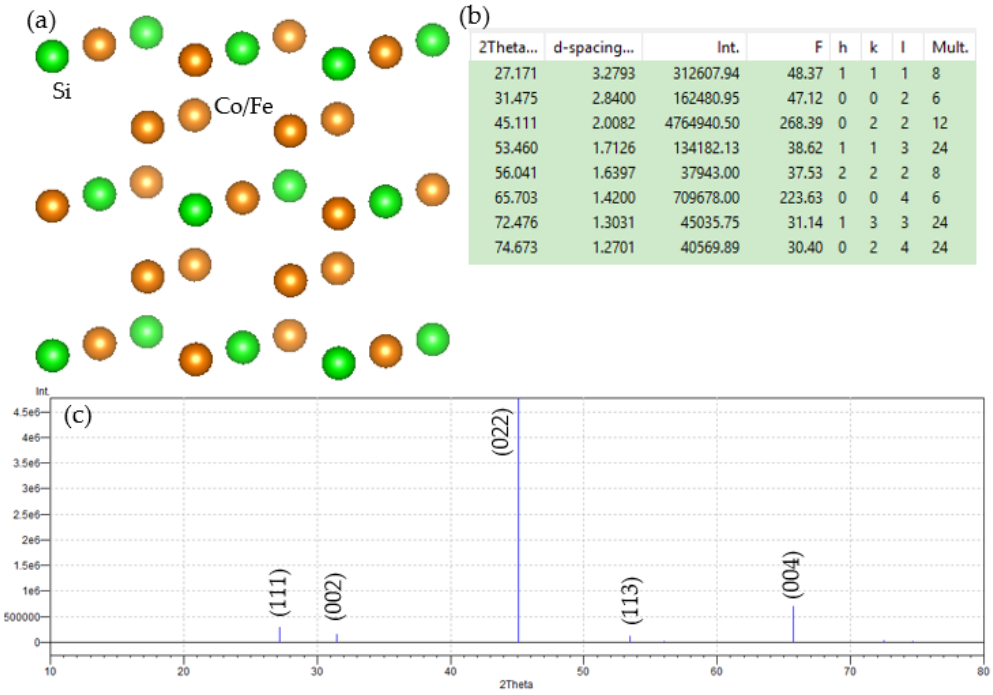

2Theta...	d-spacing...	Int.	F	h	k	l	Mult.
27.171	3.2793	312607.94	48.37	1	1	1	8
31.475	2.8400	162480.95	47.12	0	0	2	6
45.111	2.0082	4764940.50	268.39	0	2	2	12
53.460	1.7126	134182.13	38.62	1	1	3	24
56.041	1.6397	37943.00	37.53	2	2	2	8
65.703	1.4200	709678.00	223.63	0	0	4	6
72.476	1.3031	45035.75	31.14	1	3	3	24
74.673	1.2701	40569.89	30.40	0	2	4	24

Figure 5-6 DO_3 structure (BiF_3-prototype) of Co_2FeSi. (a) Schematic unit cell; (b) Calculated diffraction peak information; (c) Calculated diffraction pattern.

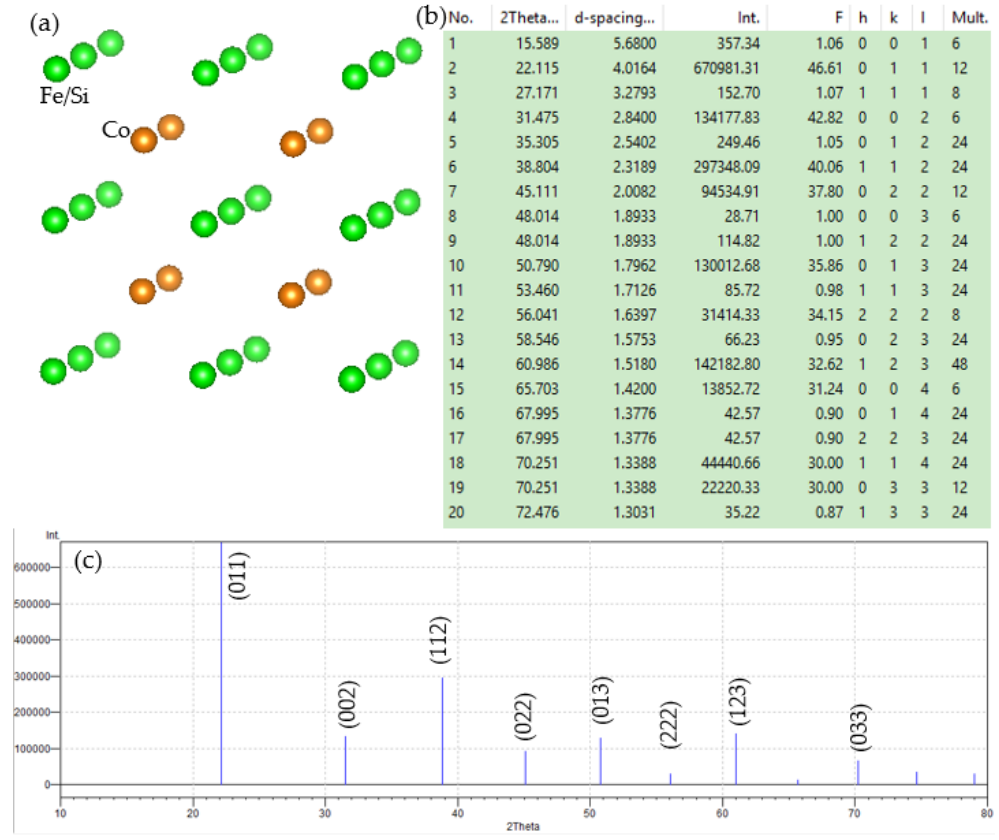

No.	2Theta...	d-spacing...	Int.	F	h	k	l	Mult.
1	15.589	5.6800	357.34	1.06	0	0	1	6
2	22.115	4.0164	670981.31	46.61	0	1	1	12
3	27.171	3.2793	152.70	1.07	1	1	1	8
4	31.475	2.8400	134177.83	42.82	0	0	2	6
5	35.305	2.5402	249.46	1.05	0	1	2	24
6	38.804	2.3189	297348.09	40.06	1	1	2	24
7	45.111	2.0082	94534.91	37.80	0	2	2	12
8	48.014	1.8933	28.71	1.00	0	0	3	6
9	48.014	1.8933	114.82	1.00	1	2	2	24
10	50.790	1.7962	130012.68	35.86	0	1	3	24
11	53.460	1.7126	85.72	0.98	1	1	3	24
12	56.041	1.6397	31414.33	34.15	2	2	2	8
13	58.546	1.5753	66.23	0.95	0	2	3	24
14	60.986	1.5180	142182.80	32.62	1	2	3	48
15	65.703	1.4200	13852.72	31.24	0	0	4	6
16	67.995	1.3776	42.57	0.90	0	1	4	24
17	67.995	1.3776	42.57	0.90	2	2	3	24
18	70.251	1.3388	44440.66	30.00	1	1	4	24
19	70.251	1.3388	22220.33	30.00	0	3	3	12
20	72.476	1.3031	35.22	0.87	1	3	3	24

Figure 5-7 B2 structure (CsCl-prototype) of Co_2FeSi. (a) Schematic unit cell (2*2 cells); (b) Calculated diffraction peak information; (c) Calculated diffraction pattern.

5.1.4 Objectives in this chapter

Similar to last chapter, this chapter try to clarify the effect of antiferromagnetism of BFO to Co_2FeSi magnetic property (ferromagnetism). Compared to CoPt, Co_2FeSi exhibits half-metallic property, which has been widely use in spintronic devices. We expect longitudinal exchange bias effect will be detected in Co_2FeSi/BFO layered structures, which expressed as either coercivity enlargement or hysteresis loop shift or both.

5.2 Experimental details

5.2.1 Co_2FeSi preparation details

Co_2FeSi target and plume is shown in Figure 5-8. Co_2FeSi is metallic and thus shows metallic shine. Target size is 2 inch diameter and power supply is DC power.

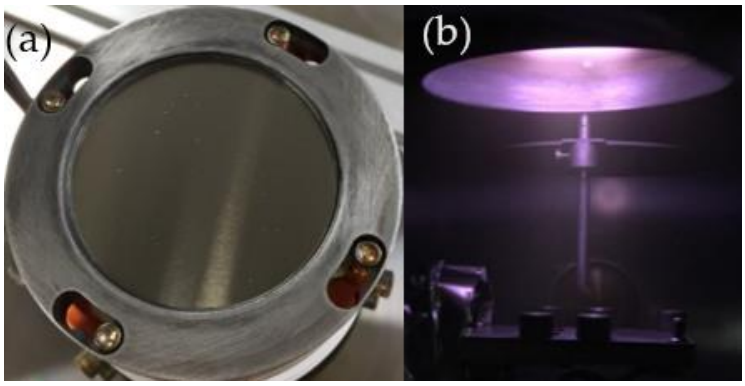

Figure 5-8 (a) Co_2FeSi target and (b) Co_2FeSi deposition plume

For single Co_2FeSi film preparation, detail growth condition are summarized in Table 5-1. The variate mainly focuses on the film thickness. This part experiment results are demonstrated in section 5.3.

5.2.2 Layered structure preparation details

In this chapter, bilayer structure CFS/BFO are prepared. Similar as last chapter, an ultra-thin Pt layer (0.5 -2 nm) was sputtered in between to prevent oxidization. Detail growth conditions for layered structure preparation are summarized in Table 5-2.

Table 5-1 Growth conditions of Co_2FeSi films in section 5.3 work

substrate	MgO (001)
base pressure	< 5.0 ×10^{-5} Pa
inlet sputtering gas	3 ccm
sputtering power	40 mA ~ 370 - 380V
deposition pressure	0.3 Pa
thickness	100, 60, 20 nm
substrate temperature	300 °C
annealed temperature	500, 600 °C (1h)

Table 5-2 Growth conditions of layered structure in section 5.4 work

	$BiFeO_3$	Pt	Co_2FeSi
substrate	STO (001) & MgO (001)		
base pressure	< 5.0 ×10^{-5} Pa	< 8.0 × 10^{-5} Pa	< 5.0 × 10^{-5} Pa
working gas	O_2 : Ar = 1 : 4	pure Ar	
sputtering power	40 mA ~ 370 - 380V	20 mA ~ 390 – 400 V	100 W
deposition pressure	0.2 Pa	0.3 Pa	0.3 Pa
thickness	30 nm	0, 0.5, 1, 1.5, 2 nm	6 nm
substrate temperature	700 °C	300 °C	300 °C

5.2.3 Patterned $Co_2FeSi/BiFeO_3$ bilayer preparation

To examine oxidization layer effect on leakage current property of BFO, patterened CFS/BFO bilayer were prepared in section 5.5. The basic growth condition is the same as listed in Table 5-2 except there is no Pt layer and thickness of BFO and CoPt is different. In section 5.5 work, BFO thickness is 50 nm and patterned CFS is 20 nm. Besides, 0.5 % wt Nd doped $SrTiO_3$ (001) substrates are used, which can also be treated as bottom electrode. For IV measurements, CFS pattern was prepared by mask. Mask detail is described in section 2.5.1. The preparation flow is illustrated in Figure 5-9.

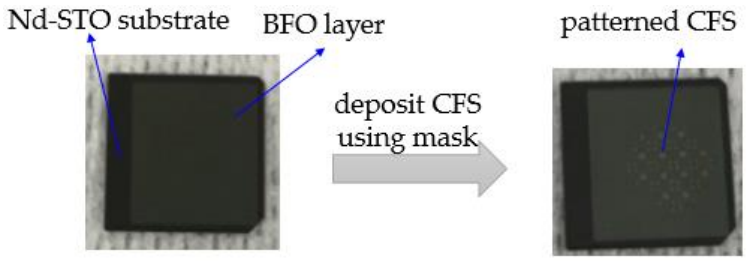

Figure 5-9 Preparation flow of patterned CFS/BFO bilayers. The pattern mask is the same as described in section 2.5.1 and the pattern area is 5 mm diameter large.

5.3 Preparation and characterization of single Co_2FeSi films

XRD profiles of single Co_2FeSi films on MgO (001) substrates with various thickness are shown in Figure 5-10. When thickness is 100 nm, CFS present (001)-orientation and has at least B2 order. As we mentioned previously, the present θ-2θ scan cannot distinguish B2 structure and $L2_1$ structure. With reducing CFS film thickness, CFS crystallinity also decreases. Small diffraction peaks still exist at t = 60 nm. Further decrease thickness to 20 nm, no crystalized CFS phase can be detected in XRD pattern, leaving on MgO substrates peaks. This indicates thin CFS films have difficulty in crystalizing when film is too thin (< 20 nm). Since our following experiments mainly concentrate on magnetic interface effect, which means CFS thickness is usually no more than 20 nm. This results makes it difficult for us to realize spintronic properties.

In order to overcome the crystallinity problem in 20 nm thickness film, we further apply rapid thermal annealing (RTA) at 500 °C and 600 °C (temperature rise finishes in 20 minutes and hold for 60 minutes), respectively. Figure 5-11 depicts the XRD profiles of annealed results. CFS peaks are labeled by yellow color. One can see, 500 °C annealing does not make any obvious differences compared to that as-deposited pattern shown in Figure 5-10. While 600 °C annealing treatment makes CFS crystalized, indicated by existence of (002) and (004) diffraction peaks. Besides, no other orientation peaks can be

detected. This means, post annealing at 600 °C can induce CFS crystal phase at thin thickness (~ 20 nm).

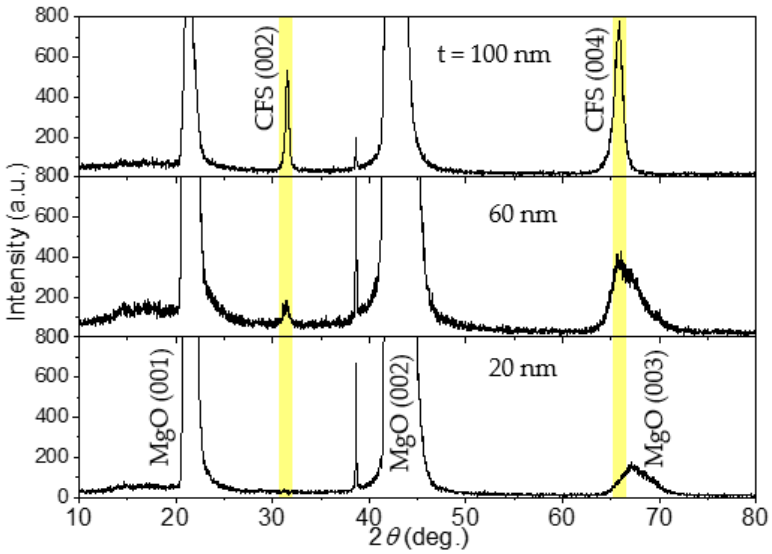

Figure 5-10 XRD profiles of Co_2FeSi films with various thickness (100, 60, 20 nm).

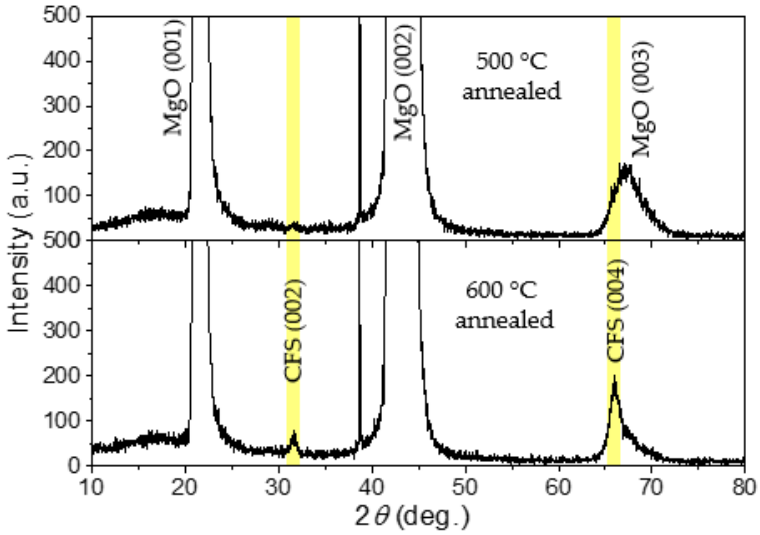

Figure 5-11 XRD profiles of 20 nm CFS films annealed at 500 °C and 600 °C, respectively.

A typical magnetic hysteresis loop of CFS is demonstrated in Figure 5-12. Quite obvious, CFS easy axis lies in in-plane direction and is longitudinal anisotropy. The in-plane coercivity is only ~ 20 Oe. The measured M_s value is 990 emu/cc, which is slightly smaller than reported. Thus for simplicity, following magnetic hysteresis in this chapter only shows in-plane loops.

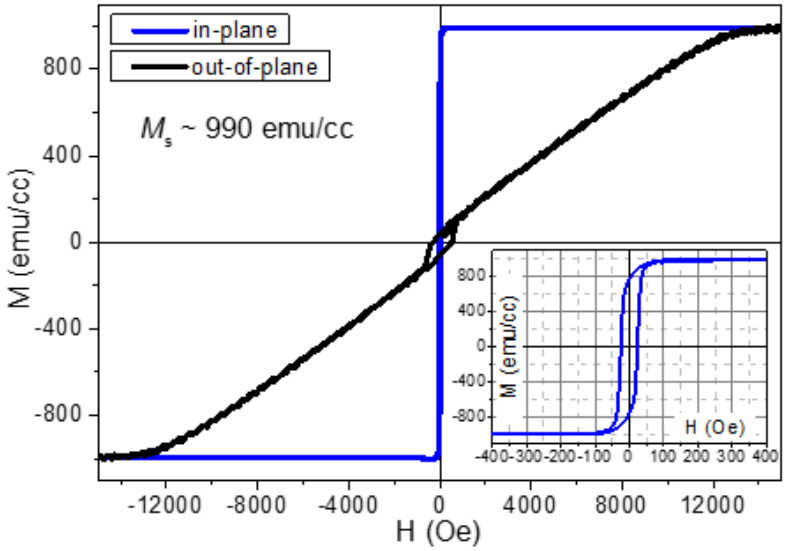

Figure 5-12 Typical magnetic hysteresis loops of CFS single films. Inset is zoomed-out image of in-plane loop.

5.4 Exchange bias in $Co_2FeSi/Pt/BiFeO_3$ layered structures

5.4.1 $Co_2FeSi/Pt/BiFeO_3$ annealing treatment

In last section, we get the results that CFS with 20 nm thickness cannot crystalize as deposited at 300 °C and 600 °C post annealing treatment can improve CFS crystallinity. To get crystal CFS phase in layered structure, we try 600 °C post annealing treatment. The XRD profiles comparison between as-deposited ($CFS_{20nm}/Pt_{0.5nm}/BFO_{30nm}/MgO$) and post-annealed samples are drawn in Figure 5-13.

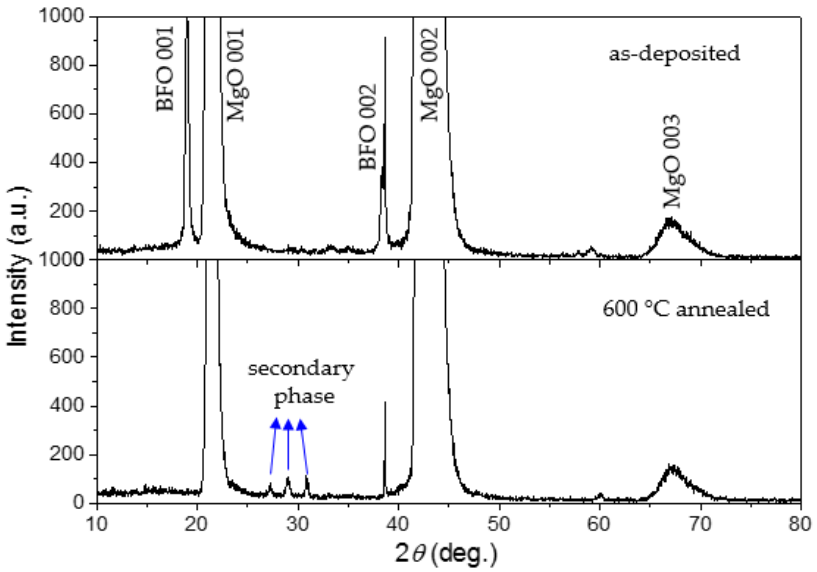

Figure 5-13 XRD profiles of as-deposited and 600 °C post-annealed samples.

To prevent the CFS oxidization during 600 °C annealing, a 0.5 nm Pt layer is sputtered in between. In the XRD result of as-deposited one, only BFO T phase (001)-oriented peaks exist. After 600 °C annealing, unexpectedly not only does BFO phase disappear, but also secondary phase emerge. Although it is hard to identify the phase information of the secondary phase, we believe it is related with Pt alloy, such as $PtBi_3$ or PtSi. Clearly severe interface diffusion occurs during annealing process. Thus post annealing treatment does not work for layered structure. And we have to admit the fact that it is difficult to obtain CFS crystal phase in CFS/Pt/BFO layered structures.

5.4.2 $Co_2FeSi_{6nm}/BiFeO_{3\ 30nm}$ films

Normally, the thickness of ferromagnet should be less than 10 nm to detect exchange bias effect.[23] Thus we fix the thickness of CFS to 6 nm. XRD profiles are drawn in Figure 5-14. Regardless of which type of substrates, BFO phase exhibits two phases: tetragonal phase (T) and rhombohedral phase (R). Both phases shows (001)-orientation. Besides, no other peaks attributed to secondary phase (such as $Bi_2Fe_4O_9$) can be found.

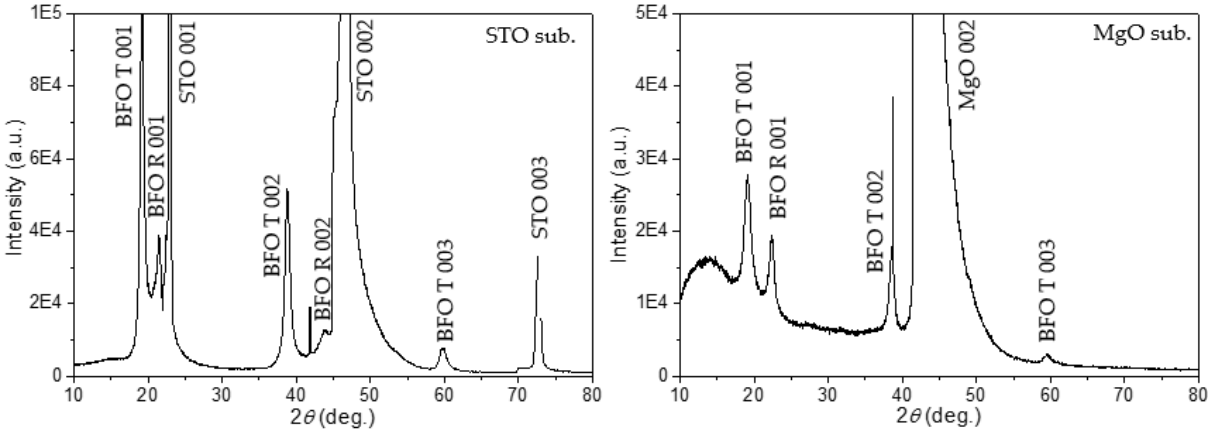

Figure 5-14 XRD profiles of CFS_{6nm}/BFO_{30nm} samples prepared on STO (001) and MgO (001) substrates, respectively.

Magnetic characterization is draw in Figure 5-15. Figure 5-15 (a) is the hysteresis loop of as-deposited sample measured at room temperature (RT). The M_s is only 560 emu/cc,

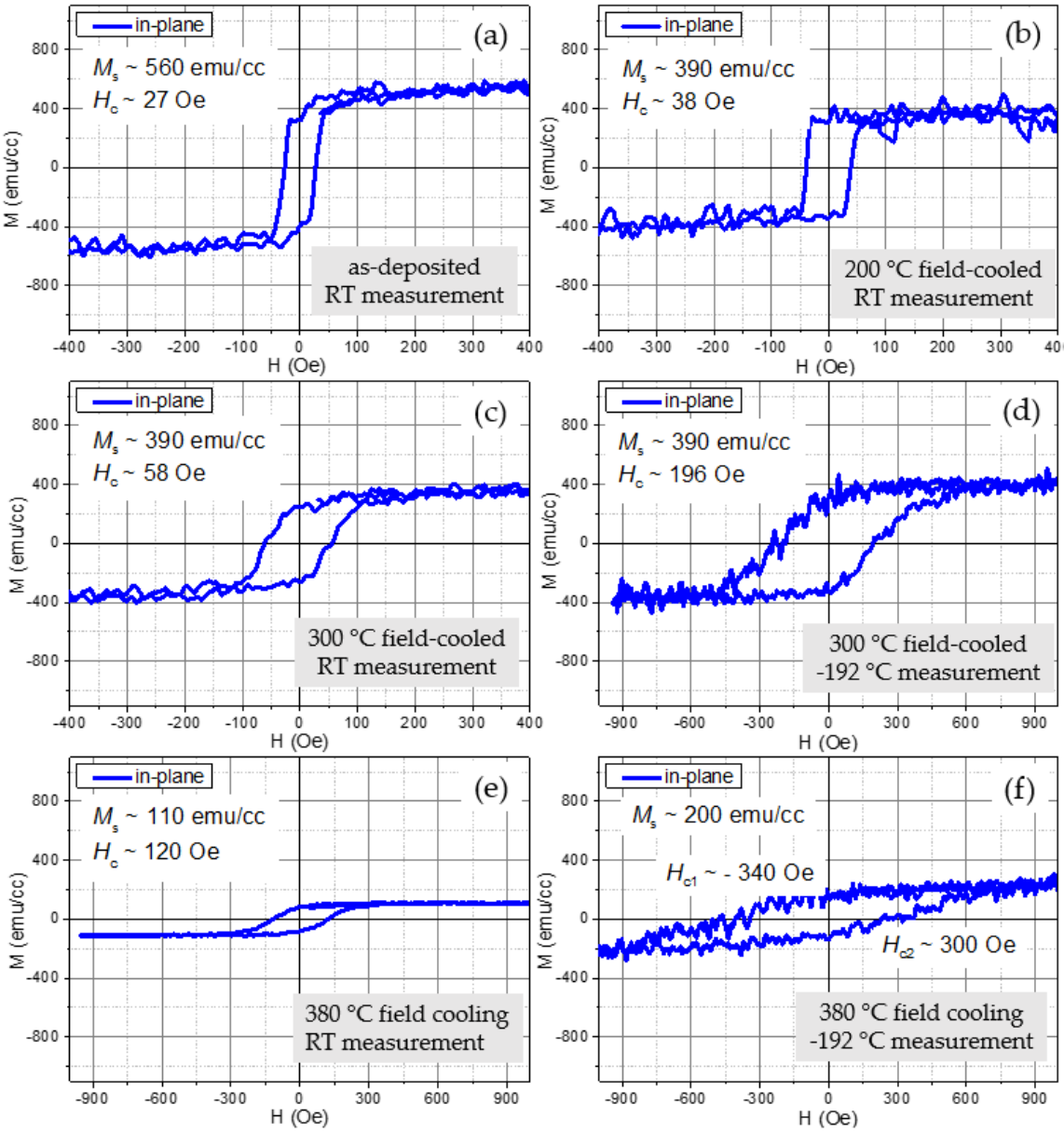

Figure 5-15 Magnetic hysteresis loops of CFS_{6nm}/BFO_{30nm}/MgO (001).

probably because of oxidization. To induce exchange bias effect, field cooling treatment from T_N (Néel temperature), that is 375 °C reported for bulk BFO, is needed. To prevent oxidization as much as possible during the field cooling process, we apply field cooling temperature from 200, 300 finally to 380 °C, in the hope that T_N will be smaller for thin film form.[24,25] Figure 5-15 (b) is the 200 °C field-cooled sample measured at room temperature (RT). Clearly slightly oxidization still happens, since the M_s reduces from 560 emu/cc to 390 emu/cc. Besides, we believe exchange bias effect occurs because the

coervicity increases from 27 to 38 Oe. Similarly, figure 5-15 (c) and (d) are the 300 °C field-cooled sample measured at RT and -192 °C, respectively. The M_s value remains at 390 emu/cc and meanwhile H_c increases to 58 Oe at RT and 196 Oe at -192 °C. Although there is no clearly observed loop shift, the H_c enlargement proves the existence of exchange bias. Figure 5-15 (e) and (f) are the 380 ° field-cooled sample measured at RT and -192 °C, respectively. Unexpectedly, the M_s dramatically decreases to 110 emu/cc (The -192 °C measurement M_s value is unconvinced due to the large noise influence.) and H_c is as large as 120 Oe at RT. Delightfully, both loop shift and coercivity enlargement are detected at -192 °C, indicating the exchange bias. The values are calculated as $H_c = (H_{c1}+H_{c2})/2 = 320$ Oe, $H_{EB} = (H_{c2}-H_{c1})/2 = 20$ Oe.

5.4.3 $Co_2FeSi_{6nm}/Pt_{0.5nm}/BiFeO_{3\ 30nm}$ films

Although exchange bias is an interface effect, many literature has reported it can still survive even with a non-magnetic layer in between.[26,27,28,29] Thus Pt layer is sputtered in the middle to prevent oxidization as much as possible.

Figure 5-16 illustrates XRD profiles of $CFS_{6nm}/Pt_{0.5nm}/BFO_{30nm}$ on STO (001) and MgO (001) substrates, respectively. Similar to that without Pt layer, both BFO T and R phase shows (001)-orientation. And there exist no peaks that can be attributed to CFS or BFO secondary phase.

Magnetic hysteresis loop measurements of CFS_{6nm} /$Pt_{0.5nm}$ /BFO_{30nm} /MgO(001) substrates are shown in Figure 5-17. For this sample, we apply 300 °C and 380 ° C field cooling process, respectively. Figure 5-17 (a) is the as-deposited films measured at room temperature. The measured M_s value is 650 emu/cc and H_c is 23 Oe. Upon 300 °C field cooling process, M_s decreases to 400 emu/cc and H_c increases to 80 Oe (Figure 5-17 (b)). After 380 °C field cooling, M_s decreases to 200 emu/cc and H_c remains at 80 Oe at RT (Figure

5-18 (c)). When measured at -192 °C, loop shift appears again. The coercivity and exchange bias field is calculated as H_c = 240 Oe and H_{EB} = -20 Oe.

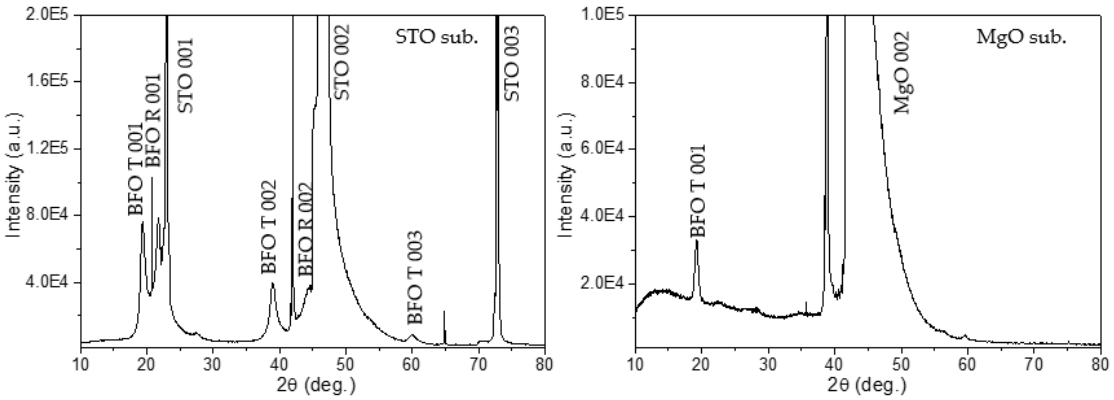

Figure 5-16 XRD profiles of $CFS_{6nm}/Pt_{0.5nm}/BFO_{30nm}$ samples prepared on STO (001) and MgO (001) substrates, respectively.

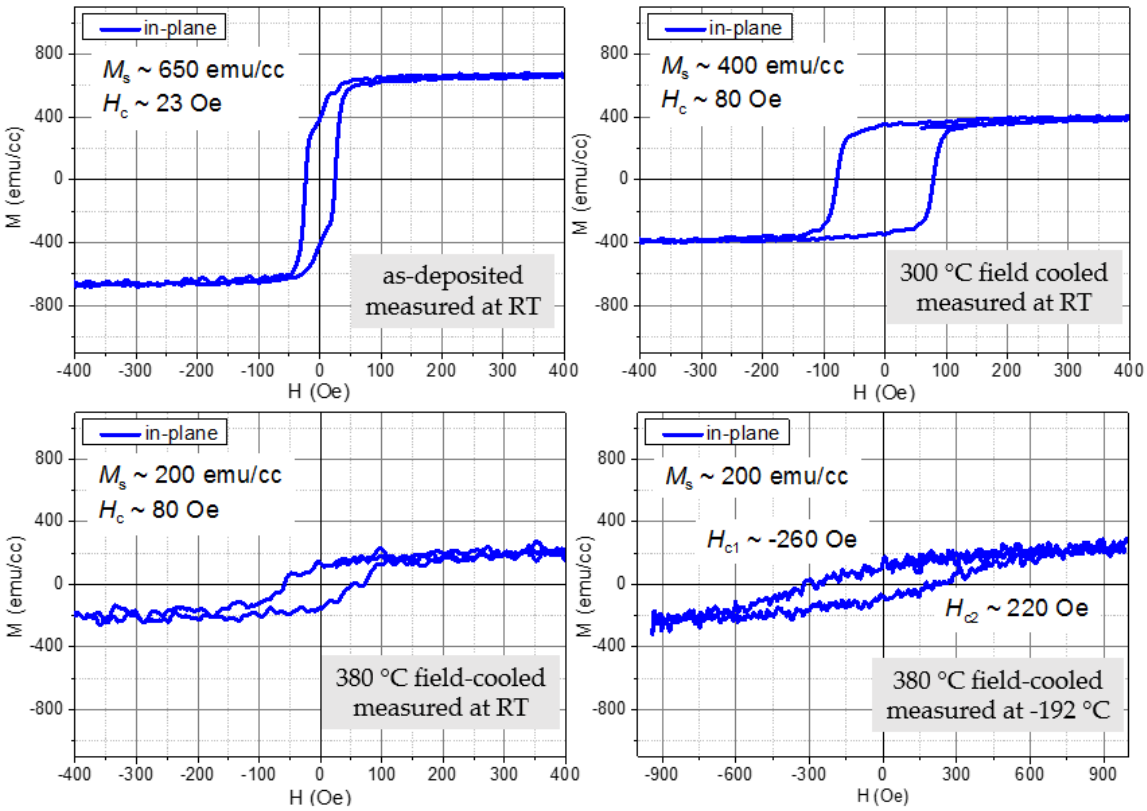

Figure 5-17 Magnetic hysteresis loops of $CFS_{6nm}/Pt_{0.5nm}/BFO_{30nm}$/MgO (001).

In all, exchange bias effect can be obtained at -192 °C measurement after 380 °C field cooling treatment. However, together with exchange bias, CFS oxidization also becomes quite severe, indicated by the M_s value reduction. If field-cooled temperature decreases

from 380 °C to 300 °C, exchange bias effect is only expressed as coercivity enlargement without loop shift.

5.4.4 $Co_2FeSi_{6nm}/Pt_{0.7nm}/BiFeO_{3\ 30nm}$ films

To further explore the Pt effect, we increase Pt thickness gradually to 0.7 nm. The XRD profiles and magnetic hysteresis loops are demonstrated in Figure 5-18 and Figure 5-19, respectively.

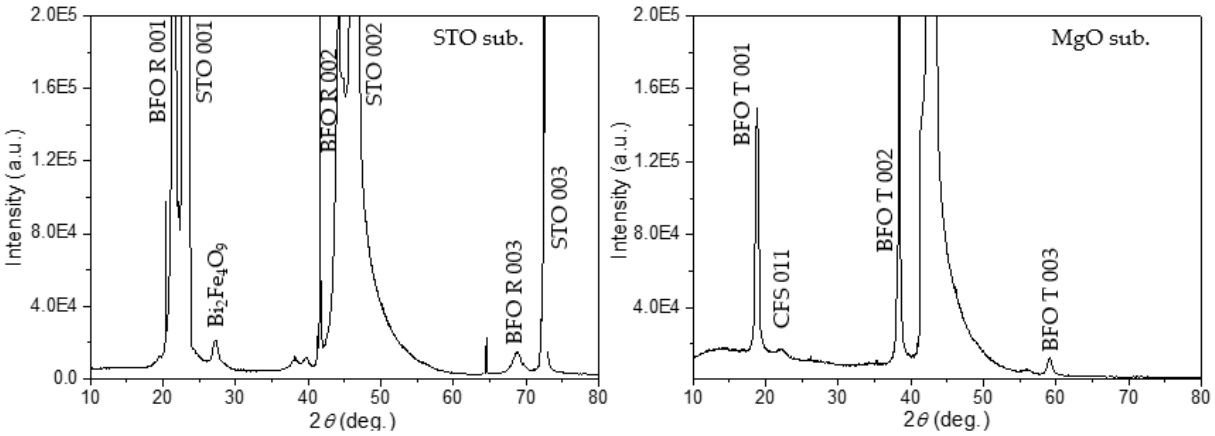

Figure 5-18 XRD profiles of $CFS_{6nm}/Pt_{0.7nm}/BFO_{30nm}$ samples prepared on STO (001) and MgO (001) substrates, respectively.

From XRD profiles, one can see that BFO presents only R phase on STO substrates and only T phase on MgO substrates. Both phases are (001)-orientation. This results are a bit different from that of $CFS_{6nm}/Pt_{0.5nm}/BFO_{30nm}$ and CFS_{6nm}/BFO_{30nm} samples, where both phases appear at the same time. At present, it is hard to tell whether such differences are related with Pt thickness. Nevertheless, there is peak attributed to CFS (011) diffraction on MgO substrates. Since this peak position is overlapped by substrate information on STO substrates and we believe this peak also exists on STO substrates. The existence of CFS crystal phase may originated from the relatively Pt thickness. We expect this thick Pt layer can smooth the interface to some extent (from section 3.4.3 we know the more crystallinity the rougher BFO surface is) and promote CFS crystallization process.

Although different BFO phases present on various substrates, it seems does not make any big differences to magnetic properties, as shown in Figure 5-19. For the as-deposited samples, the M_s is around 800 emu/cc and H_c ~ 20 Oe. The hysteresis shape is more squared (M_r/M_s is larger) upon 300 °C field cooling. And M_s decreases to ~ 600 emu/cc while H_c increases to 70 Oe. As explained before, H_c enlargement is a manifestation of exchange bias effect.

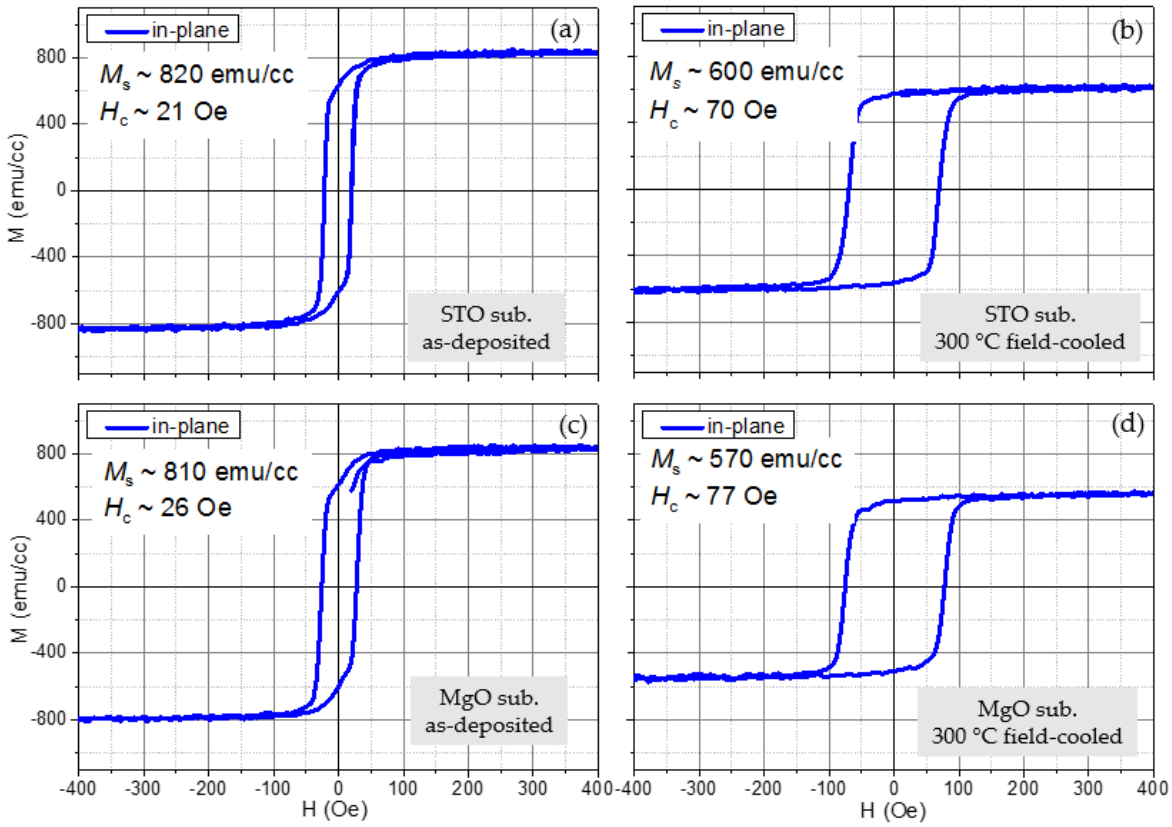

Figure 5-19 Magnetic hysteresis characterization of as-deposited (a) and 300 °C field cooled (b) $CFS_{6nm}/Pt_{0.7nm}/BFO_{30nm}$/STO substrate and as-deposited (a) and 300 °C field cooled (d) $CFS_{6nm}/Pt_{0.7nm}/BFO_{30nm}$/MgO substrate. All measurements are conducted in RT.

5.4.5 $Co_2FeSi_{6nm}/Pt_{2nm}/BiFeO_{3\ 30nm}$ films

Pt thickness is further increased to 2 nm. XRD profiles and magnetic characterization are summarized in Figure 5-20 and 5-21, respectively. The same with that of $CFS_{6nm}/Pt_{0.7nm}/BFO_{30nm}$ samples, BFO exhibits R phase on STO substrates and T phase on

MgO substrates (shown Figure 5-20). And CFS (011) peak can be observed, indicating the crystal phase of CFS.

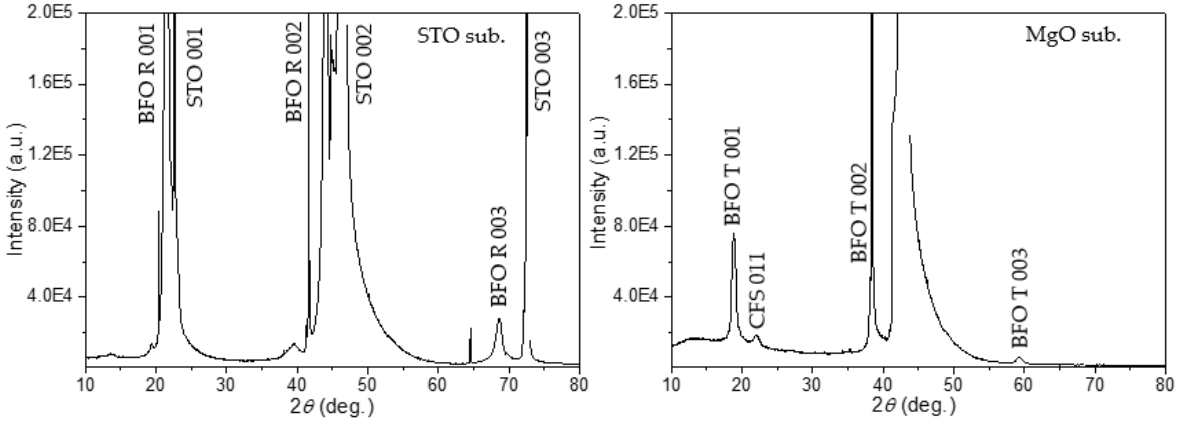

Figure 5-20 XRD profiles of $CFS_{6nm}/Pt_{2nm}/BFO_{30nm}$ samples prepared on STO (001) and MgO (001) substrates, respectively.

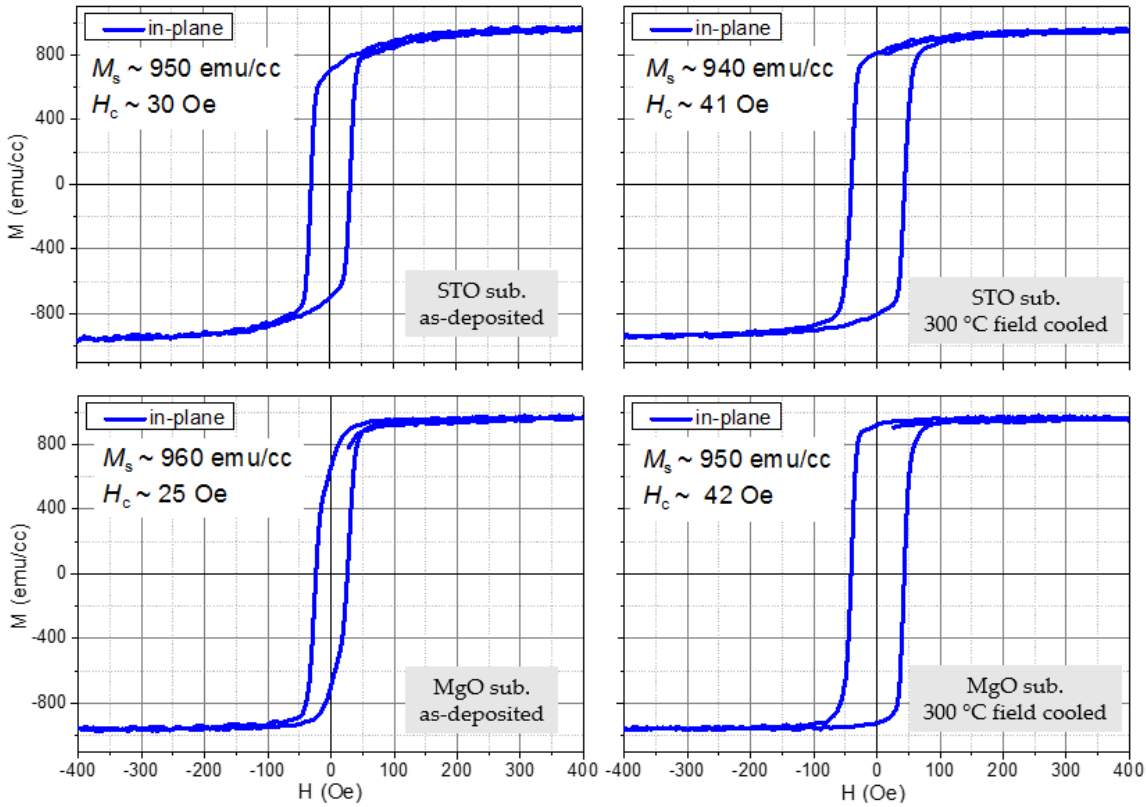

Figure 5-21 Magnetic hysteresis characterization of as-deposited (a) and 300 °C field cooled (b) $CFS_{6nm}/Pt_{2nm}/BFO_{30nm}$/STO (001) substrates films. As-deposited (a) and 300 °C field cooled (d) $CFS_{6nm}/Pt_{2nm}/BFO_{30nm}$/MgO (001) substrates films. All measurements are conducted in RT.

The magnetic measurements are shown in Figure 5-21. Samples prepared on STO and MgO substrates do not have big differences. The 2 nm Pt layer can greatly prevent CFS oxidization in both the as-deposited conditions and 300 °C field cooling process, since the M_s value remains at 950 emu/cc. The bad effect of thick Pt layer is also clear, that the Hc enlargement magnitude is smaller compared to before. This is reasonable, since thick Pt layer block the interaction to some extent.

5.4.6 Pt effect summary

This section mainly summarizes the Pt effect demonstrated in section 5.4.2 to 5.4.5. As shown in Figure 5-22, M_s values of as-deposited (black and square dots) and 300 °C field-cooled (blue and round dots) samples prepared on MgO substrates with various Pt thickness are listed. Quite clear, with increasing Pt thickness, M_s becomes high. Both are the same tendency for as-deposited and field-cooled results.

Similarly, H_c values dependence of Pt interlayer thickness is summarized in Figure 5-23. There exists a peak H_c value at Pt ~ 0.5 nm. When there is no Pt layer, oxidization is severe and the oxidized layer separate the interaction. The existence of Pt can prevent such oxidization and interface effect can still survive though this ultra-thin layer. However, if Pt is too thick (> 2 nm), itself will block the interaction as well.

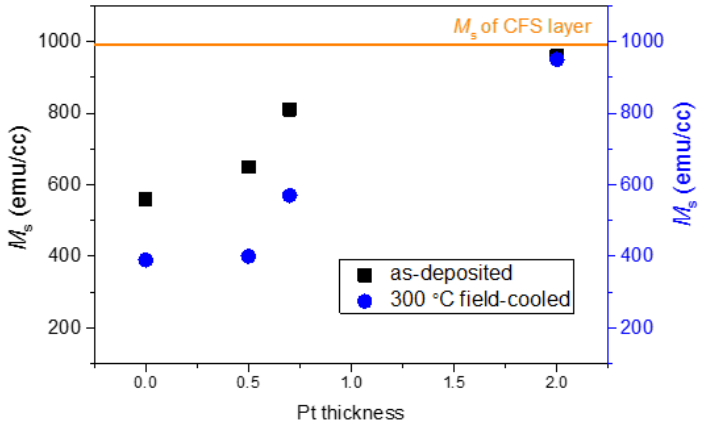

Figure 5-22 Layered structure M_s dependence of Pt interlayer thickness.

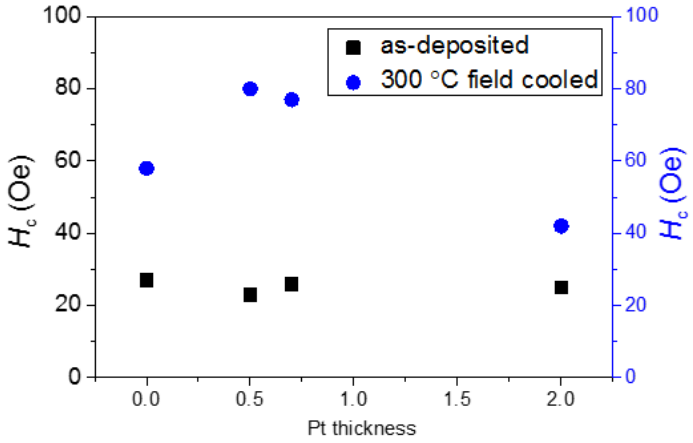

Figure 5-23 Layered structure H_c dependence of Pt interlayer thickness.

To further confirm the Pt effect, Auger electron spectroscopy (AES) depth profiles of CFS/BFO layered with and without Pt layers (0.7 nm) are conducted, as compared in Figure 5-24. The existence of Pt layer is clearly observed. Since this method is only semi-quantitative, we only use the concentration value as a comparison ruler and do not take it for real. Without Pt layer, oxygen concentration goes directly upward from CFS to BFO layers. While with 0.7 nm Pt, a clear oxygen concentration drop is detected around interface. One thing needs to point out that O source not only comes from BFO layers, but also from the atmosphere. Besides, existence of Pt can also prevent Co atom inter-diffuse into BFO layers indicated the Co diffusion length comparison, which is the same situation for BFO/CoPt in last chapter.

Such CFS oxidization is further indicated by cross-section TEM image of as-deposited CFS/BFO sample, shown in Figure 5-25. Similar to XRD pattern in Figure 5-14, BFO layer displays a clear (001)-texture growth. Although no CFS peaks can be detected in XRD, CFS phase still crystalize indicated TEM images. Besides, oxidized layer is observed between BFO and CFS layers, and its thickness is estimated around 2-3 nm. Since no cap layer is deposited on the top, a oxidized layer also exists at the film surface, which agree with AES depth profile.

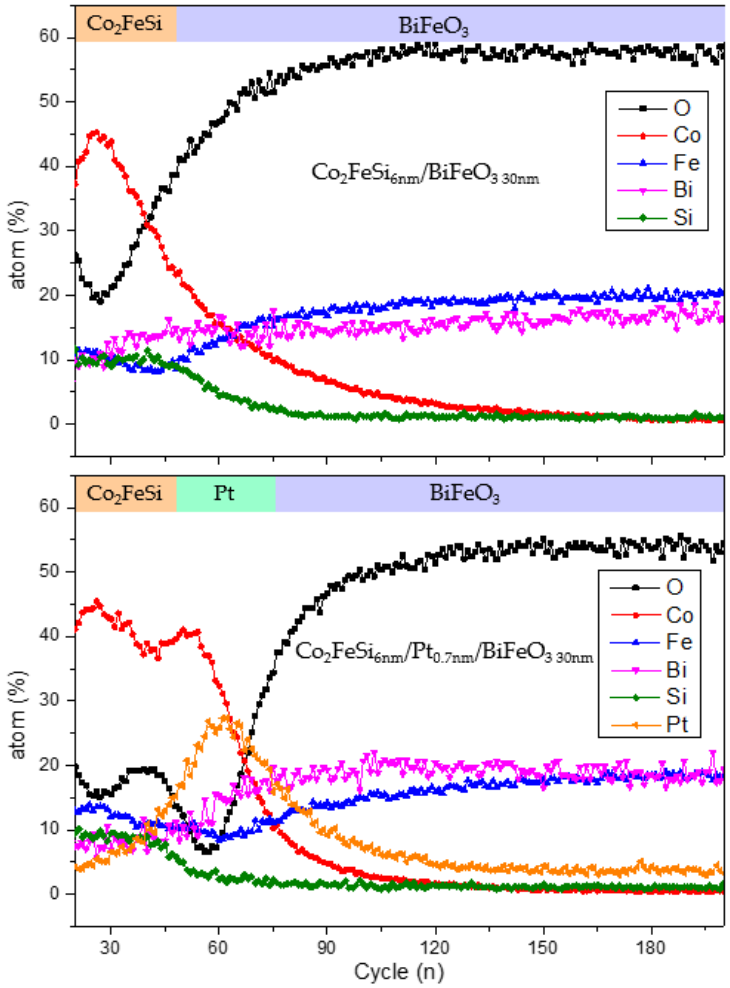

Figure 5-24 Auger electron spectroscopy (AES) depth profiles of CFS_{6nm}/BFO_{30nm} and $CFS_{6nm}/P_{0.7nm}/BFO_{30nm}$ films, respectively.

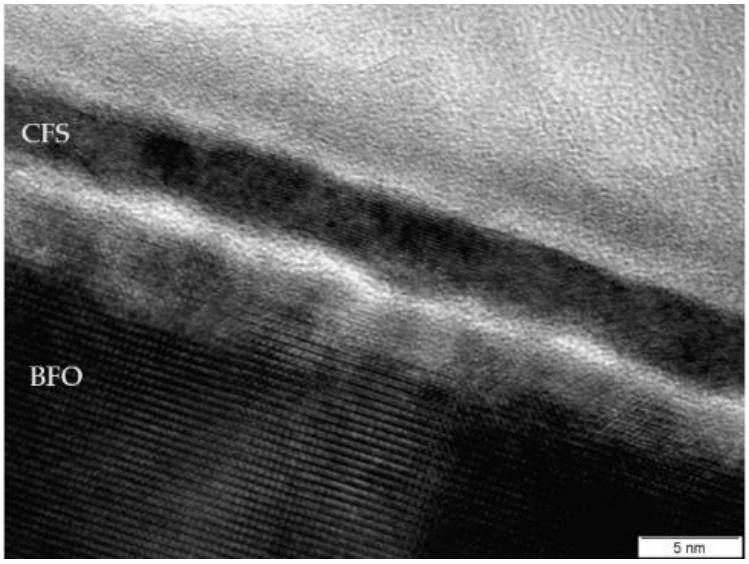

Figure 5-25 Cross-section TEM image of as-deposited CFS_{6nm}/BFO_{30nm} sample. Clear oxidized layer is observed at the interface between CFS and BFO.

5.5 Preparation and characterization of patterned $Co_2FeSi/BiFeO_3$ bilayers

As we know from last section, CFS layer deposited directly on BFO films is easily oxidized. In this section, we concentrate on this oxidized layer effect on BFO leakage current measurement.

Figure 5-26 draws XRD profiles of patterned CFS/BFO/Nd-STO with different CFS deposition temperature. Only BFO R phase can be detected in the XRD profiles and there are no sign of CFS peaks. Thus no big differences can be seen from the XRD.

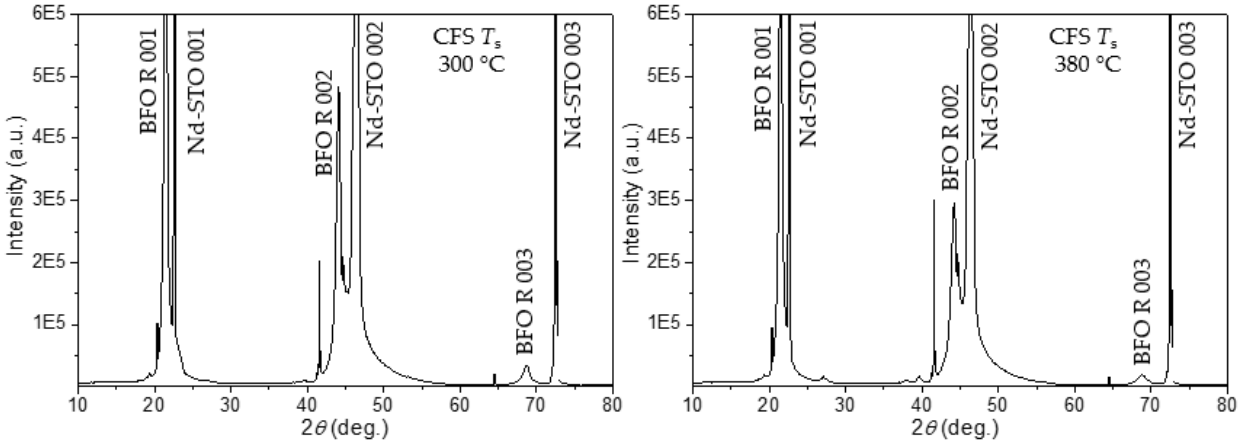

Figure 5-26 XRD profiles of patterned CFS_{20nm}/BFO_{30nm}/Nd-STO samples with different CFS deposition temperature (300 and 380 °C).

Figure 5-27 compares the hysteresis loops of sample prepared with different CFS deposition temperature (300 and 380 ° C). Probably because of the small amount of CFS films, the measured loops do not exhibit much differences in terms of M_s values. Besides, 380 °C deposited film even seems to display a bit higher M_s value than that of 300 ° deposited films. In common sense, the higher deposition temperature is, the more severe oxidization exists, leading to smaller M_s value. However, such expected tendency has not been detected probably due to the measurement resolution.

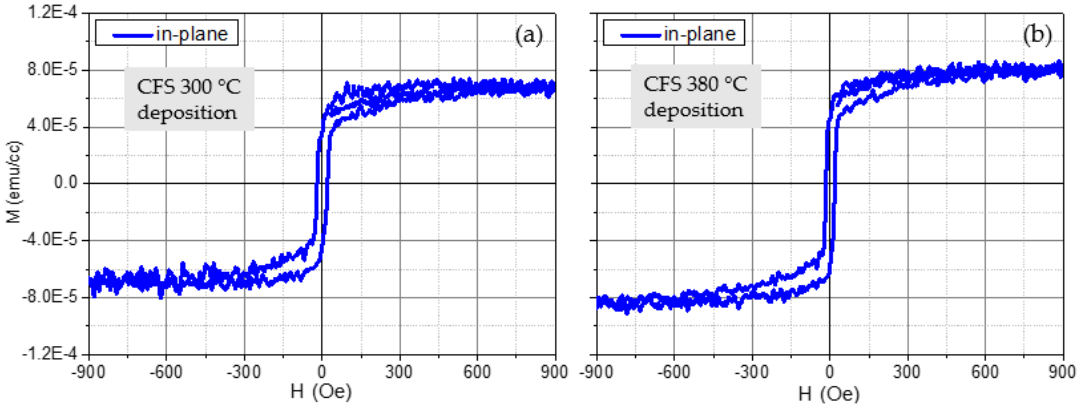

Figure 5-27 Magnetic hysteresis loops of patterned CFS_{20nm}/BFO_{30nm}/Nd-STO samples with different CFS deposition temperature (300 and 380 °C).

VI curves of the two films are compared in Figure 5-28. In the current leakage measurement, CFS dot (prepared by masks) serves as top electrode and Nd-STO substrate is bottom electrode. At small current range, 300 ° prepared sample shows high voltage value, and this might because the severe surface scratch (clearly observed under microscopy). At ~ 40 μA, two curves have a cross-section. In the high current range, 380 °C deposited CFS sample shows higher voltage. We believe the high current range tendency is the intrinsic properties of two samples. The slightly higher voltage value at the same current condition means this sample is less conductive compared to that of 300 °C sample. This high resistivity may originate from oxidization of CFS layers. This oxidized CFS layers can prevent the current leakage problem of BFO films some extent.

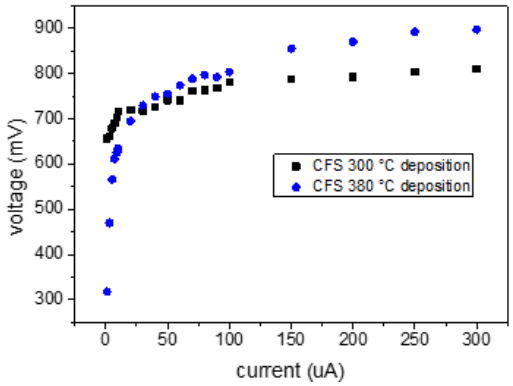

Figure 5-27 VI measurements of patterned CFS_{20nm}/BFO_{30nm}/Nd-STO samples with different CFS deposition temperature (300 and 380 °C).

5.6 Summary

Co_2FeSi single layers and $Co_2FeSi/Pt/BiFeO_3$ layered structures are prepared in this chapter. For single layers, crystalized CFS phase (at least B2 order) can only exist if thickness is larger than 60 nm. However, only several nanometer thickness is preferred in spintronic devices. Then post annealing treatment is conducted to increase thin film (20 nm) crystallinity. CFS single layer starts to crystalize when post-annealed at 600 °C for 1 hours. Despite of the success, this method does not work well for CFS/Pt/BFO layered structures, because inter-diffusion occurs. Although no CFS peaks can be detected, CFS phase still crystalizes in the layered structure, indicated by TEM image.

Followed by the preparation, we characterize the magnetic hysteresis loops of layered structures. Suggested by M_s values, existence of Pt layer can prevent CFS oxidization effectively, in both as-deposited and field-cooled situations. However, if Pt is too thick (~ 2 nm), interaction between CFS and BFO will be blocked, reflected by the reduction of coercivity enlargement (an expression of exchange bias effect). Thus there exists a trade-off between CFS oxidization and exchange bias effect and the best Pt thickess is ~ 0.5 nm. In all, longitudinal exchange bias effect has been observed in CFS/Pt/BFO layered structures.

Reference

[1] F. Heusler, W. Starck and E. Haupt, *Verh DPG* **5**, 220 (1903)

[2] T. Graf, C. Felser and S. S. P. Parkin, *Prog. Solid State Chem.* **39**, 1 (2011)

[3] C. Felser, G. H. Fecher and B. Balke, *Angew Chem. Int. Ed.* **46**, 668 (2007)

[4] J. Winterlik, G. H. Fecher and C. Felser, *Solid State Commun.* **145**, 475 (2008)

[5] K. R. Kumar, V. Chunchu and A. Thamizhavel, *J. Appl. Phys.* **113**, 17E155 (2013)

[6] X. Y. Dong, J. W. Dong, J. Q. Xie, T. C. Shih, S. McKernan, C. Leighton and C. J. Palmstrom, *J. Cryst. Growth* **254**, 384 (2003)

[7] H. C. Kandpal, C. Felser, R. Seshadri, *J. Phys. D Appl. Phys.* **39**, 776 (2006)

[8] C. J. Palmstrom, *Prog. Cryst. Growth Charact. Mater.* **62**, 371 (2016)

[9] P. Villars, L. D. Calvert, *Pearson's handbook of crystallographic data for intermetallic phases*. American Society of Metals, 1991

[10] J. Nuss and M. Jansen, *Z Anorg Allg Chem.* **628**, 1152 (2002)

[11] B. Balke, S. Wurmehl, G. H. Fecher, C. Felser and J. Kubler, *Sci. Technol. Adv. Mater*. **9**, 014102 (2008)

[12] S. Wurmehl, G. H. Fecher, H. C. Kandpal, V. K.senofontov and C. Felser, *Appl. Phys. Lett.* **88**, 032503 (2006)

[13] S. Wurmehl, G. H. Fecher, V. Ksenofontov. F. Casper, U. Stumm and C. Felser, *J. Appl. Phys.* **99**, 08J103 (2006)

[14] Z. Gercsi, A. Rajanikanth, Y. K. Takahashi and K. Hono, *Appl. Phys. Lett.* **89**, 082512 (2006)

[15] N. Tezuka, N. Ikeda, S. Sugimoto and K. Inomata, *Appl. Phys. Lett.* **89**, 252508 (2006)

[16] N. Tezuka, N. Ikeda, F. Mitsuhashi and S. Sugimoto, *Appl. Phys. Lett.* **94**, 162504 (2009)

[17] S. Wurmehl, G. H. Fecher, H. C. Kandpal, V. Ksenofontov and C. Felser, *Phys. Rev. B* **72**, 184434 (2005)

[18] H. C. Kandpal, G. H. Fecher and C. Felser, *J. Phys. D: Appl. Phys.* **40**, 6 (2007)

[19] J. Kubler, G. H. Fecher and C. Felser, *Phys. Rev. B* **76**, 024414 (2007)

[20] P. Blaha, K. Schwarz, G. K. H. Madsen, D. Kvasnicka and J. Luitz, 2001 WIEN2K, An Augmented Plane Wave + Local Orbitals Program for Calculating Crystal Properties Karlheinz Schwarz, Techn. Universitaet Wien, Wien Austria

[21] A. B. Garg and V. Vijayakumar, *J. Appl. Phys.* **10**, 083523 (2011)

[22] B. Balke, S. Wurmehl, G. H. Fecher, C. Felser, M. C. M. Alves, F. Bernardi and J. Morais, *Appl. Phys. Lett.* **90**, 172501 (2007)

[23] P. K. Manna and S. M. Yusuf, *Phys. Rep.* **535**, 61 (2014)

[24] X. Y. Lang, W. T. Zheng and Q. Jiang, *Nanotechnology*, **18**, 155701 (2007)

[25] A. J. Devasahayam and M. H. Kryder, *J. Appl. Phys.* **85**, 5519 (1999)

[26] J. Sort, V. Baltz, F. Garcia, B. Rodmacq, B. Dieny, *Phys. Rev. B* **71**, 054411 (2005)

[27] M. Ali, C. H. Marrow, B. J. Hickey, *Phys. Rev. B* **77**, 134401 (2008)

[28] V. K. Valev, M. Gruyters, A. Kirilyuk, T. Rasing, Phys. Rev. Lett. 96, 067206 (2006)

[29] J. Geshev, S. Nicolodi, L. G. Pereira, L. C. C. M. Nagamine, J. E. Schmidt, C. Deranlot, F. Petroff, R. L. Rodriguez-Suarez, A. Azevedo, *Phys. Rev. B* **75**, 214402 (2007)

Chapter 6 Conclusions

Interface structure and magnetic properties of $BiFeO_3$ –based layered structures are explored in this thesis. $BiFeO_3$ (BFO) is the only room temperature single-phase multiferroic material discovered at present and receives hot attention in spintronic field. Chapter 2 and chapter 3 focus on the structure characterization of $BiFeO_3$ films prepared on various substrates (a-SiO_2, MgO and $SrTiO_3$ substrates) and under layer (TiN layer). Chapter 4 and 5 report interface induced magnetic performances of $BiFeO_3$/$L1_0$ ordered CoPt and Co_2FeSi/$BiFeO_3$ layered films, respectively.

Main conclusions of this thesis are summarized in the following:

1) Growth of crystal BFO films is quite sensitive to substrates. No pure crystalized BFO films can be obtained on a-SiO_2 substrates, while poly-crystal like (three growth orientation) and epitaxial BFO films are prepared on MgO substrates (mismatch ~ - 6.6 %) and STO substrates (mismatch ~ 1.4 %), respectively.
2) BFO epitaxial films can be grown on conductive TiN under layers at reduced substrate temperature (~ 500 °C). TiN is widely used as electrodes in current semiconductor techniques, and thus it will greatly broaden BFO application prospect if embedded on TiN layers. Our results indicate rhombohedral (R) and tetragonal (T) of BFO co-exist and both structures show epitaxial growth: T-BFO (001)[100]//TiN (001)[100] and R-BFO (001)[100]//TiN (001)[100].
3) Perpendicular exchange coupling effect is observed in $BiFeO_3$/$L1_0$ ordered-CoPt layered structures. Besides, this effect can be mediated by external static magnetic field (5000 Oe). That is the coupling effect (expressed as existence of plateau in the hysteresis loops) is induced by in-plane direction field and vanishes upon out-of-

plane field. Cross-section element mapping results suggest there exist two additional layers across the BFO/CoPt interlayer: Co-containing BFO layer (2 nm) and Co-deficient CoPt layer (1.5 nm). These different layers respond to external field differently and lead to two shapes of hysteresis loops.

4) Longitudinal exchange bias effect is observed in $Co_2FeSi/BiFeO_3$ layered structures. Various thickness (0, 0.5, 0.7, 2 nm) of Pt layer is sputtered in between. Both VSM and AES depth profiles suggest existence of Pt can prevent inter-diffusion of O and Co atoms. However, too thick Pt layer (2 nm) also blocks the interface interaction between CFS and BFO. To balance, 0.5 nm Pt layer is the optimal, where coercivity enlarges from 20 Oe to 80 Oe after field-cooling treatment. This coercivity enlargement is a manifestation of exchange bias effect, which describes the pinning effect of antiferromagnetic moments to ferromagnetic layers at the interface.

In all, preparation and magnetic characterization of BFO-based layered films are studies in this thesis work.

Publications

Papers included in the thesis

1. "Epitaxial growth of $BiFeO_3$ films on TiN under layers by sputtering deposition"
   Yue Wang, Tianjun Li, Jian Wang, Takashi Harumoto, Tingting Jia, Hideo Kimura, Katsuyuki Nakada, Shigeki Nakagawa, Yoshio Nakamura and Ji Shi, *AIP advances*, **7**, 055815 (2017)
2. *"Magnetic field-mediated exchange coupling effect in $BiFeO_3$/CoPt layered structure"*
   ***Yue Wang**, Takashi Harumoto, Jian Wang, Eiji Suzuki, Katsuyuki Nakada, Yoshio Nakamura, Shigeki Nakagawa and Ji Shi, to be submitted*
3. *"Exchange bias effect in $BiFeO_3$/Co_2FeSi Heusler layered films"*
   ***Yue Wang**, Takashi Harumoto, Jian Wang, Eiji Suzuki, Katsuyuki Nakada, Yoshio Nakamura, Shigeki Nakagawa, Ji Shi, in preparation*

Other papers

1. "SnAs with the NaCl-type structure: Type-I superconductivity and single valence state of Sn"
   Yue Wang, Hikaru Sato, Yoshitake Toda, Shigenori Ueda, Hidenori Hiramatsu and Hideo Hosono, *Chemistry of Materials*, **26**, 7209 (2014)
2. "Magnetoelastically induced perpendicular magnetic anisotropy and perpendicular exchange bias of CoO/CoPt multilayer films"
   Lei Guo, **Yue Wang**, Jian Wang, Shinji Muraishi, Takumi Sannomiya, Yoshio Nakamura and Ji Shi, *Journal of Magnetism and Magnetic Materials*, **394**, 349 (2015)

International conferences

1. "Co-existence of tetragonal and pseudo-cubic phases in $BiFeO_3$ film deposited on TiN under layer"
   Yue Wang, Jian Wang, Takashi Harumoto, Yoshio Nakamura, Katsuyuki Nakada, Shigeki Nakagawa and Ji Shi, 61st Annual Conference on Magnetism and Magnetic Material, 31st Oct.- 4th Nov. New Orleans, Louisiana, USA
2. "Enhancement of perpendicular anisotropy in $BiFeO_3$/CoPt bilayer structure"
   Yue Wang, Hongyu An, Takashi Harumoto, Yoshio Nakamura, Katuyuki Nakada, Shigeki Nakagawa and Ji Shi, 61st Annual Conference on Magnetism and Magnetic Material, 31st Oct.- 4th Nov. New Orleans, Louisiana, USA
3. "Perpendicular exchange bias phenomenon in BiFeO3/CoPt bilayer structure"

Yue Wang, Takashi Harumoto, Yoshio Nakamura, Shigeki Nakagawa and Ji Shi, *5th International Education Forum on Environment and Energy Science*, San Diego, 15th – 19th Dec. 2016 (oral)

4. "Substrate effect on structure formation of $BiFeO_3$ films"
   Yue Wang, Tianjun Li, Takashi Harumoto, Shigeki Nakagawa and Ji Shi, *4th International Education Forum on Environment and Energy Science*, Hawaii, 6th – 10th Dec. 2015 (oral)

Patents

1. 積層構造体、スピン変調素子及び磁気記録システム（積層層構造体）
   鈴木　英治、中田　勝之、米村　祥吾、中川　茂樹、史　蹟、王　月、 出願中、出願番号：特願 2017-191288
2. 積層構造体、スピン変調素子及び磁気記録システム（積層製造法および応用素子の電圧印加方法）
   鈴木　英治、中田　勝之、米村　祥吾、中川　茂樹、史　蹟、王　月、 出願中、出願番号：特願 2017-191289
3. 積層間磁気カップリングスイッチングに基づいた磁気デバイス
   鈴木　英治、中田　勝之、中川　茂樹、史　蹟、王　月、 出願中、出願番号：特願 2017-190457

Acknowledgements

Foremost, I'd like to express my sincere gratitude to my supervisor in doctor course, Prof. Ji Shi, for his guidance in academic research and helps in daily life. I could not have imagined having a better advisor and mentor for my doctor period. I'm also very grateful to my supervisor in master course Prof. Hideo Hosono. His acceptance of my enrolment in Tokyo Institute of Technology is the beginning of my research life. I learn a lot from Prof. Hosono, obsession to research, perseverance, self-discipline. His unique characters enlightened me and helped me go through the difficult period in Japan.

My sincere thanks also goes to Prof. Shigeki Nakagawa for his numerous advices and continuous support to my research. And great thanks to Mr. Eiji Suzuki, Mr. Katsuyuki Nakada from TDK Corporation for their technical advices and financial support.

I'm also thankful to Prof. Yoshio Nakamura. He is always very kind and quite supportive to my research. I'd particularly like to express my thanks to assistant Prof. Takashi Harumoto. I could not finish this work without his detail explanations, careful guidance and countless helps. Special thanks to associate Prof. Takumi Sannomiya for his explanations and demonstrations of TEM operations.

Many thanks to Dr. Jian Wang in National Institute for Materials Science (NIMS) for his careful experimental measurements of TEM and SQUID. To Prof. Hideo Kimura and Dr. Tingting Jia in NIMS for their ferroelectric measurement helps. To Dr. Hongyu An in Keio University for his magnetic measurement support. To Dr. Tenghua Gao, who is now in Keio University, for useful discussions and enlightening me the glance of research.

A special gratitude goes to Prof. Zaoli Zhang in Austrian Academy of Sciences for offering me an opportunity to study analysis and operations of TEM.

I'd like to single out my genuine thanks and love to my husband Dr. Chao Zhi. He is the first reason I came to Japan. He is always there for me to support me spiritually and financially in my doctor life. I could not survive happily without his concern and love.

I thank my fellow lab mates in Namamura-Shi lab of Titech: Lei Guo, Hiroto Sakimura, Tianjun Li (now in Tsinghua Univ.), Satoshi Inagaki, Toshiki Omi, Yuki Sugiura, Petrus Caesario, Hangxian Gao, Ying Gao, Haomin Xu (now in Tsinghua Univ.), Chunjiao Pan (now in Tsinghus Univ.), Fuxing Wan, Naoto Kikuchi, Atsuki Ienaka, Taiyo Asakawa, Katsuya Uchida, Hiroki Kato. Together they make the laboratory a friendly place.

In addition, I want to give my special thanks to Prof. Hidenori Hiramatsu, Dr. Hikaru Sato for their kind training and academic guidance in the first period of my research life.

I also appreciate the financial and activity support from "Academy for Co-creative Education of Environment and Energy Science" in Titech.

Thanks to Mr. Hori, Mr. Suzuki, Mr. Tada and other members of Ookayama Materials Analysis Division for their experimental support.

Last but not the least, I'd like to thank my parents for giving birth to me at the first place and emotional care throughout my overseas life.